UNIVERSITÀ DEGLI STUDI DI PALERMO

Ph.D. Course in Information and Communication Technologies
Department of Energy, Information Engineering and Mathematical Models (DEIM)
Scientific Disciplinary Sector: ING-INF/01

Instabilities Effects in Thin Film Solar Cells: Reversible Ageing, Performance Recovery and Improvement by Electrical Stresses

Ph.D. CANDIDATE
Andrea Scuto

COORDINATOR
Prof. Ilenia Tinnirello

TUTOR
Prof. Alessandro Busacca

CO TUTOR
Dr. Salvatore A. Lombardo

CYCLE XXX
YEAR 2018

IMM Institute for Microelectronics and Microsystems

“Knowledge is nothing without imagination”

Albert Einstein

UNIVERSITA' DEGLI STUDI DI PALERMO

Ph.D. Course in Information and Communication Technologies – XXX Cycle
Department of Energy, Information Engineering and Mathematical Models (DEIM)

Instabilities Effects in Thin Film Solar Cells: Reversible Ageing, Performance Recovery and Improvement by Electrical Stresses

by **Andrea Scuto**

Abstract

Aim of this Ph.D. work was the study of the instabilities effects in Thin Film Solar Cells. The research was principally intended to a substantial experimental activity of electrical and optical measurements, to the physical modeling of solar cells behaviors and to the development of suitable electrical and optical conditioning techniques oriented to gain stability, reliability and an overall performance improvement for second and third generation solar cells. This project report consists of seven chapters.

Chapter 1 represents an introduction to this research. A first part is dedicated to Renewable Energy Sources and their importance. It is here discussed about the challenges and objectives of Solar Energy by examining its properties, the different Photovoltaics Technologies and the various generations of solar cells available in the market, with a particular focus on Thin-Film solutions. The second part examines the hydrogenated amorphous Silicon (a-Si:H), pointing out on the main advantages and defects, listing its structural characteristics and focusing on the Staebler-Wronski Effect (SWE) occurring during light soaking of this type of cells. Here, in addition to the single junction analysis, it is discussed about how amorphous silicon is used in multi-junction cells, focusing attention on a-Si:H / microcrystalline Si tandem solar cells. Finally, the third part summarizes the reasons that led to the present thesis study and what are its goals.

Chapter 2 focuses on the ageing effects of hydrogenated amorphous Si (a-Si:H) under illumination. In this chapter, after a theoretical background on the typical defect density distrubution and the main strategies to reduce such unsolicited effects, is experimentally analyzed the role of the H_2/SiH_4 ratio during the PECVD deposition of the a-Si:H layers at 255 °C on the time zero performance of the solar cells, given the important role played by the H_2 dilution. Furthermore, showing the evident role of light intensity on degradation characteristics, this section underlines the effect of the different layers thickness on initial solar cell performance.

Chapter 3 investigates on the effects of prolonged exposure to reverse bias DC electric fields and illumination as a function of temperature in hydrogenated amorphous Si (a-Si:H) photovoltaic single *p–i–n* junctions. In this chapter we show that the application of a reverse bias stress in presence of illumination not only slows down the solar cell ageing kinetics but even produces an improvement of the cells parameters as a function of stress time. Such improvements have been investigated discussing the impact of temperature, electric field intensity, illumination level and reversibility properties (the applied external bias has a strong influence on the solar cell reversibility property, resulting strongly dependent from it). In addition, it is shown that different types of bottom contact over which the a-Si:H is grown by PECVD have a strong influence on the recovery-improvement kinetics: SnO:F (FTO) transparent conductive oxide (TCO) and molybdenum bottom contacts to the p-type a-Si:H layer are here compared. In order to confirm this, we demonstrate that an analogous improvement (reduction) of sheet resistance is observed in single thin films of doped a-Si:H deposited on SiO_2 under the application of high intensity electric fields. Moreover, discussing also about the radical differences between the forward and reverse bias stress on the spectroscopic signature of the defects responsible for the instability / improvement effect, we determine the range of wavelengths where the photons are effective to improve the lifetime and cell efficiency. Finally, examples of reverse bias practical use in solar cell application are shown.

Chapter 4 further investigates the aforementioned amorphous solar cells improvement kinetic, analyzing such effects also in the case of a-Si:H / microcrystalline Si tandem solar cells.
It has found that also in this case of tandem cells there is a clear improvement under reverse bias stress with illumination. But it is extremely important to notice that much lower stress voltages are here required, though the presence of illumination during the stress is crucial as in the case of single junction a-Si:H cells. It is here shown how after stress in MPP condition, it is possible to completely recover the cell efficiency η, and that the kinetics of the following LID under MPP conditions appear slower. Finally, even in this case it has shown the profound difference of behavior between forward and reverse bias stress, and it has found clear evidence of the range of wavelengths of the photons needed to assist the recovery / improvement effect under DC voltage stress. In this chapter a first part is dedicated to analyze the electric field contribution on single cells in indoor conditions, i.e. assisted

by the solar simulator illumination while a second part is intended to examine the stress effects repoorted by the cells under real condition of illumination (outdoor analysis) and for commercial tandem amorphous/microcrystalline Silicon PV minimodules.

Chapter 5 is dedicated to Dye-Sensitized Solar Cells (DSSCs) as promising Thin-Film third generation photovoltaic devices given their potential low cost and high efficiency. Despite great attention is reserved, some factors still affect DSSCs performance, such structure of electrodes, electrolyte compositions, nature of the sensitizers, power conversion efficiency, long-term stability, etc. In this section it is discussed the effect of electrical stresses, which allow to improve DSSC performance. We have investigated the outcomes of forward and reverse DC bias stress as a function of time, voltage, and illumination level in the DSSCs sensitized with the N719, Ruthenium complex based dye. We demonstrate that all the major solar cell parameters, i.e., open circuit voltage (V_{OC}), short circuit current (I_{SC}), series resistance (R_{OC}), fill factor (FF), and power conversion efficiency are, even in this type of solar cells, strongly influenced by the stress conditions and a clear reversibility of the parameters on the stress type is shown. In this context are examined also the possible effects that emerge from the electrolyte composition. We investigate the effects of temperature and electrolyte composition by means of current–voltage measurements and electro-chemical impedance spectroscopy, both under dark and illumination conditions.

Chapter 6, as final part of this report, summarizes the key finding of this project due to the overall set of experimental results, providing novel information to understand the cause of the many discussed improvements and containing recommendations and developments for future studies based on this P.h.D. work.

This work was principally carried out in collaboration with the researchers of the “Electrical and Optical Measurements group of CNR IMM Headquarter and has been partially funded by the National Project MIUR PON R&C 2007-2013, project “Tecnologie per l’ENERGia e l’Efficienza energETICa (ENERGETIC)” (PON02_00355_3391233).

In addition, regarding the solar cell manufacturing/assembly, research has benefited from profitable collaborations with important industrial realities and excellent research centers such as: *STMicroelectronics* and *3SUN* (*Enel Green Power*), for the study of hydrogenated amorphous silicon solar cells and the *Department of Physics and Chemistry of University of Palermo* and the *Institute for Physical Chemistry* (*IPCF-CNR*) of Messina with regard to the DSSC preparation and cells characterizations.

Acknowledgements

I would like to express my heartfelt thanks to all the people who contributed in some way to the work described in this thesis, who has been close to me and has supported me over these years.

First, I would like to express my deepest gratitude to my tutor, Prof. Alessandro Busacca, who provided me the right determination and passion for the research work. Precious was his support to make my Ph.D. experience productive and stimulating.

Immense gratitude is specially directed to my co-tutor Dr. Salvatore Lombardo, professional and personal mentor during my intense activity at CNR-IMM labs of Catania. With his immense knowledge he guided me along these years helping me in all the time of research and I really appreciate all his contributions of time, ideas, and funding. The joy and enthusiasm he has for the research was contagious and motivational for me.

In addition to my tutors, I would like to express my thankfulness also to the coordinator of the Ph.D. course, Prof. Ilenia Tinnirello, for her availability and courtesy.

I would like to thank also all Laboratory of Optics and OptoelectroniX (LOOX) research team of the University of Palermo and all people of CNR IMM headquarter who helped and supported me over these years.

Every result described in this thesis was main accomplished with the help and support of all my labmates and collaborators. The electrical and optical measurements group of CNR-IMM, in particular, has been in the last years a source of friendships as well as good advice and collaboration. A special thanks is so directed to Dr. Stefania Privitera, Dr. Silvio Pierro, Dr. Luca Valenti, Dr. Gabriella Milazzo, Dr. Ting Ting Han and Dr. Fabio Ricco Galluzzo for the precious cooperation.

Deep gratitude is also directed to Dr. Marina Foti of STMicroelectronics, to Dr. Cosimo Gerardi and Dr. Francesco Aleo of Enel, to Dr. Anna Battaglia, Dr. Andrea Canino and Dr. Giuseppe Condorelli of 3SUN; of great value and very appreciated was their collaboration over these years; in addition to providing the a-Si:H samples and research materials on which to perform part of the present research, my gratitude goes to all of them for their scientific support and enjoyable technical discussions, but also for their friendship.

For the precious contribution made to the study of the DSSCs and for the really appreciate support and

collaboration over these years, I would moreover like to thank immensely Dr. Gaetano Di Marco, Dr. Giuseppe Calogero and Dr. Ilaria Citro of CNR-IPCF (who provided me DSSCs used in this work) and Dr. Fabio Principato and Dr. Clara Chiappara of the University of Palermo. I am grateful to them for their friendship and for their high level scientific support in this work.

At last, I would like to thank my great family for all their support and encouragement: a special thank is so directed to my parents, who raised me with love and supported me in all my pursuits; to my special grand parents and sisters, that always supported my ideas and choices; to my supportive, encouraging, and patient wife Laura and to my precious and loving sons Eleonora and Edoardo. For all these reasons, I will never stop thanking and I dedicate this work to them.

Contents

Chapter 1

Introduction

1.1. Solar Electricity from Photovoltaics: Achievements and Challenges

Current approach in energy supply and use has become, nowadays, unsustainable both on the economic and environmental side. Without decisive and political actions, energy-related emissions of CO_2 will more than double in thirty years increasing oil demand rather than increasing the exploitation of clean energy. We can and must change our way of thinking and doing, but this needs a really energy revolution based on new ideas of energy and technologies [1,2]. Energy efficiency, renewable energy concept, nuclear power and new transport technologies will all require widespread deployment if we want to reach gas emission goals we imposed. Every major country and sector of the economy must be involved. The task is also urgent if we are to make sure that investment decisions taken now will not damage us in the long term.

Everyone of us think that should be really the right moment to turn political statements and analytical work into concrete action. To accelerate this reaction, at the request of the G8, the International Energy Agency (IEA) is developing a series of roadmaps for some of the most important technologies. These roadmaps provide solid analytical footing that enables the international community to move forward on specific technologies. Each roadmap develops a clear line for every particular technology from today to 2050, and identifies technology, financing, policy and public engagement milestones that need to be achieved to realise the technology's full potential. Roadmaps also include special focus on technology development and diffusion to emerging economies. International collaboration will be critical to achieve these goals [2-8].

While its use is small today, solar photovoltaic (PV) power has a great potential, representing a real alternative particularly promising for the future. Global PV capacity has been increasing at an average annual growth rate of more than 40% since 2000 and it has significant potential for long-term growth over the next decades. This roadmap envisions that by 2050, PV will provide 11% of global electricity production (4 500 TWh per year), corresponding to 3 000 gigawatts of cumulative installed PV capacity. In addition to contributing to a significant gas emission reduction, this level of PV will deliver substantial benefits in terms of the security of energy supply and socio-economic development.

To get this goal, a strong and balanced policy effort in the next decade will be required to allow for optimal technology progress, cost reduction and ramp-up of industrial manufacturing. This roadmap also identifies goals and milestones that must be undertaken by different stakeholders to enable the most cost-efficient expansion of the different PV technologies [9].

1.1.1. Solar Energy

The light emitted by the sun, travelling through space and time, can be identified as electromagnetic waves, a form of energy which is emitted and absorbed by charged particles. Quantum physics postulates that Electromagnetic waves are emitted as discrete bundles of energy, or *quanta*, called photons. The energy, E (known as irradiative energy), contained in a photon is defined by Eq. 1.1.

$$E = hf = \frac{hv}{\lambda} \qquad \text{Eq. 1.1}$$

where h is Planck's constant, f is the frequency, v is the wave velocity and λ represents the wavelength.

The photons are emitted by so-called thermal radiators. The idealized thermal radiator is known as a black body, which absorbs all incoming irradiation, and, in thermal equilibrium, re-emits it all isotropically. The thermal radiator, and therefore the black body, is characterized by an emission spectrum according to its temperature. Essentially, any physical body is a thermal radiator, but the most important one in our solar system, and the one which most closely assimilates the behavior of a black body, is the sun. With a surface temperature close to 6000 °K, the sun's radiation emission spectrum is described by two quantities, the spectral power density, $P(\lambda)$, and the photon flux density, $\phi(\lambda)$. As the emission and absorption of EM-waves occur in quanta or photons, the quantities describing an emission spectrum must link the emitting body to a certain photon distribution. Therefore, the photon flux describes the number of photons per unit time, unit area, and unit wavelength which are being emitted. Meanwhile, the spectral power density is a measure of incoming power per unit wavelength per unit area. Thereby, the two quantities are linked through the photon energy defined in Eq. 1.1. Next equation shows the relation between spectral power density and photon flux.

$$P(\lambda) = \phi(\lambda) * E = \phi(\lambda) * \frac{hv}{\lambda} \qquad \text{Eq. 1.2}$$

Starting from this equation, it is easy to obtain the power density, i.e. the quantity of energy per unit area, doing the integration of the spectral power density of the sun over its entire emissive spectral range. Losses of irradiative energy, or more precisely, the spectral power density, will occur when the electromagnetic waves of the sun are passing through the earth's atmosphere. The total energetic loss to the atmosphere will therefore depend on the path length within the boundaries of the atmosphere, and thus the geographical position where the measurement is taking place. In order to quantify this measure, the ratio of the distance travelled to the shortest path length of the electromagnetic waves is defined optical "air mass".

The air mass, or AM value, is defined according to the zenith angle of a geographical location, θ, as reported in Eq. 1.3.

$$air\ mass = AM = \frac{1}{\cos(\theta)}$$

Eq. 1.3

The air mass is an important parameter because it gives not only a measure of energy lost to the atmosphere, but it permits for a standardization of test conditions. In order to set an industry standard, the spectral response corresponding to the emissive spectrum at AM1.5, i.e. a zenith angle of 48.2 degrees, is always reported when referring to solar cells [9]. An illustrative schematic of optical air mass considerations is shown in Fig. 1.1 seen below.

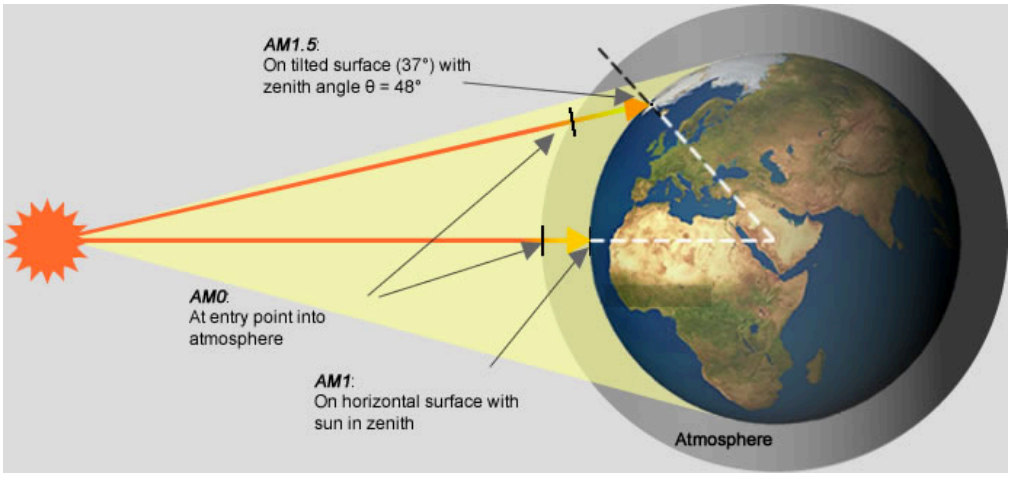

Fig. 1.1. Correspondence between air mass and path lengths of solar radiation incident to the earth. The figure is adapted from [9].

AM-value is so dependent from the geographical location. The AM-value influence also the sun spectral power density distribution. For reference, the spectral power density distribution is usually given for AM0, which is defined as the position outside the earth's atmosphere. A figure of the complete spectral power distribution is provided in Fig. 1.2.

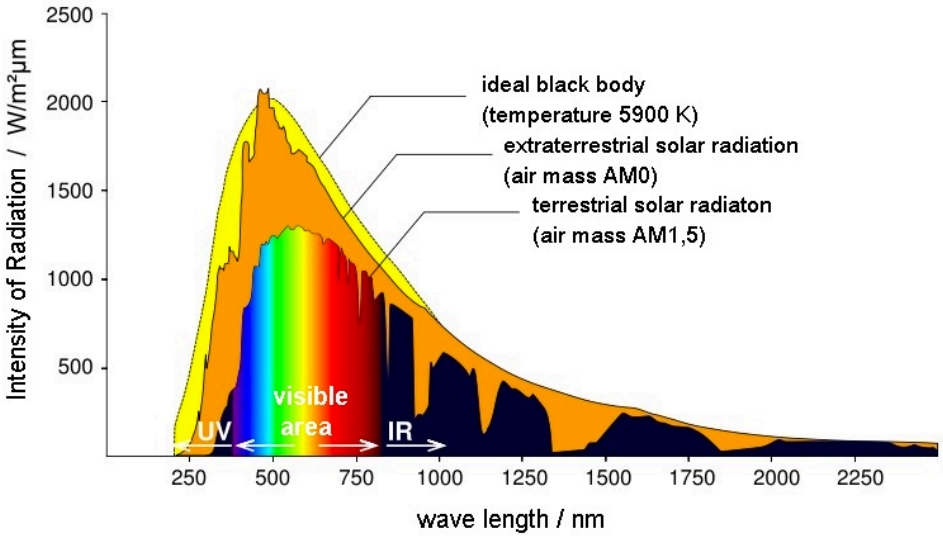

Fig. 1.2. Spectral power density distribution of the sun for different AM-values. © Wikimedia Creative Commons Licence.

It is common practice to distinguish between *direct sunlight* (reaches the earth's surface without interference from atmospheric particles), the *diffuse sunlight* (scattered by the atmospheric particles), and the *albedo* (reflected from the earth's surface). The global power density measured is the combination of these three. As such, the value of the integrated AM1.5 spectrum is defined as 1000 W/m^2 [10]. When referring to solar energy, it is so really important underlines the AM-value considered.

1.1.2. Photovoltaics and Energy Harvesting

Photovoltaic is the technology that generates direct current (DC) electrical power measured in watts (W) or kilowatts (kW) from semiconductors when they are illuminated by photons. As long as light is shining on the solar cell (the name for the individual PV element), it generates electrical power. When the light stops, the electricity stops. Solar cells never need recharging like a battery. Some have been in continuous outdoor operation on Earth or in space for over 30 years. The global solar resource is enormous, and the earth receives a tremendous amount of it. It is estimated that in one hour of

noontime summer sun, the United States mainland receives enough solar energy to meet its annual electricity demand. Moreover, the amount of solar radiation striking the earth in one day is enough energy to satisfy our population for 27 years [10].

PV solar cells are based on the *photovoltaic effect*, a process by which a voltage difference is generated in a material upon the absorption of photons. The material in question is a semiconductor, due to its well suited opto-electrical qualities. Due to the distribution of energy states in this type of material, one can define certain bands of states, namely the *valence band*, the forbidden band (usually referred to as the *band gap),* and the *conduction band*, in order of increasing energy. The valence band represents charge carriers with little freedom for movement. The conduction band, on the other hand, pertains to states where charge carriers have freedom to move, i.e. conduction may occur. Finally, the band-gap represents the distance between valence and conduction bands, a space energetically inhibited by semiconductor charges carriers.

As depicted in Fig. 1.3, when the solar cell is exposed to sunlight of sufficient energy, the incident solar photons are absorbed by the atoms, breaking the bonds of valence electrons and pumping them up to higher energy in the conduction band. There, a specially made selective contact collects conduction-band electrons and drives these freed electrons to the external circuit. The electrons lose their energy by doing work in the external circuit such as pumping water, spinning a fan, powering a sewing machine motor, a light bulb, or a computer. They are restored to the solar cell by the return loop of the circuit via a second selective contact, which returns them to the valence band with the same energy that they started with.

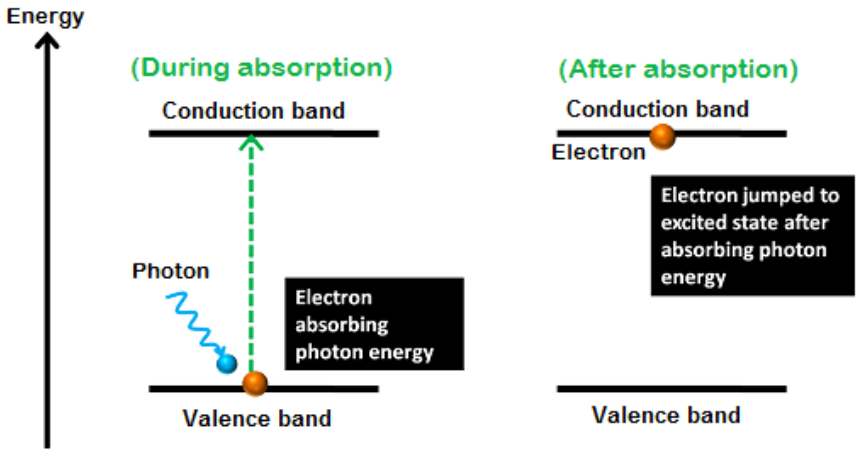

Fig. 1.3. Schematic of a solar cell. Electrons are pumped by photons from the valence band to the conduction band. © Wikimedia Creative Commons Licence.

The potential at which the electrons are delivered to the external world is less than the threshold energy that excited the electrons; that is, the bandgap. It is independent of the energy of the photon that created it (provided its energy is above the threshold). Thus, in a material with a 1eV bandgap, electrons excited by a 2eV (red) photon or by a 3eV (blue) photon will both still have a potential voltage of slightly less than 1V (i.e. both of the electrons are delivered with an energy of about 1 eV). The electrical power produced is the product of the current times the voltage; that is, power is the number of free electrons times their electric charge times their voltage. Brighter sunlight causes more electrons to be freed resulting in more power generated.

Sunlight is given by a full set of photons distributed over a spectrum of energy. Photons whose energy is greater than the bandgap energy (the threshold energy) can excite electrons from the valence to conduction band where they can exit the device and generate electrical power. Photons with energy less than the energy gap fail to excite free electrons and the relative energy travels through the solar cell and is absorbed at the rear as heat.

For practical applications, a certain number of solar cells are interconnected and encapsulated into units called PV modules, which is the product usually sold to the customer. They produce DC current that is typically transformed into the more useful AC current by an electronic device called an inverter.

1.1.3. PV Trends in Tecnology: an Overview

PV systems directly convert solar energy into electricity. The basic building block of a PV system is the PV cell, which is a semiconductor device that converts solar energy into direct-current (DC) electricity. PV cells are interconnected to form a PV module, typically up to 50-200 Watts (W). The PV modules combined with a set of additional application-dependent system components (e.g. inverters, batteries, electrical components, and mounting systems), form a PV system. PV systems are highly modular, i.e. modules can be linked together to provide power ranging from a few watts to tens of megawatts (MW). R&D and industrialisation have led to a portfolio of available PV technology options at different levels of maturity [11]. Even that commercial PV modules may be divided into two broad categories: wafer based c-Si and thin films, there are a range of emerging technologies, including concentrating photovoltaics (CPV) and organic solar cells, as well as novel concepts with significant potential for performance increase and cost reduction. Here an overview of the different technologies:

Crystalline silicon (c-Si) modules represent 85-90% of the global annual market today. c-Si modules are subdivided in two main categories: i) single crystalline (sc-Si) and ii) multi-crystalline (mc-Si).

Thin films currently account for 10% to 15% of global PV module sales. They are subdivided into three main families: i) amorphous (a-Si) and micromorph silicon (a-Si/µc-Si), ii) Cadmium-Telluride (CdTe), and iii) Copper-Indium-Diselenide (CIS) and Copper-Indium-Gallium-Diselenide (CIGS).

Emerging technologies encompass advanced thin films and organic cells. The latter are about to enter the market via niche applications.

Concentrator technologies (CPV) use an optical concentrator system which focuses solar radiation onto a small high-efficiency cell. CPV technology is currently being tested in pilot applications.

Novel PV concepts aim at achieving ultra-high efficiency solar cells via advanced materials and new conversion concepts and processes. They are currently the subject of basic research.

Current PV solar cell technologies may be also grouped into three main categories; although the solar cell industry is still relatively young, the pace of innovation, research, and development has resulted indeed in three *generations* of solar cells per today.

The ***first generation*** consists of crystalline silicon (c-Si) solar cells; the first solar cells to be commercially exploited and produced on a large scale. First generation cells consist of large-area, high quality and single junction devices. In addition this solar cells are high-cost and high-efficiency components, obtaining efficiencies between 20 and 25 percent. Such solar cells largely employ a structure of one junction between n-doped c-Si and p-doped c-Si. The reason for the elevated prices of first generation solar cells is the level of purity which is required for the crystalline material, and consequently, high production costs. Furthermore, these types of solar cells are subject to the *Shockley-Queisser* limit, a balance limit which refers to the maximum theoretical efficiency of a p-n junction solar cell [12]. This limit, which is based on a balance of losses inherent to the solar cell material and the junction, is considered to be 33.7% for first generation solar cells.

Second generation solar cells are low-cost yet lower efficiency devices, reaching conversion efficiencies between 10 and 15 percent. Such solar cells are thin-film devices, and, as the name implies, can be deposited as single, thin layers. This is because thin-film technology employs a different type of material, most commonly hydrogenated amorphous silicon (a-Si:H), copper indium gallium selenide (CIGS), and cadmium telluride (CdTe), which exhibit entirely different absorption levels than the c-Si material. The benefit of this type of solar cells is therefore the reduced production costs and increased production rate.

Finally, the optimal solar cell technology, which can obtain ideally high efficiencies at low cost, is commonly denoted as ***third generation*** technology. Third generation technologies aim to enhance poor electrical performance of second generation (thin-film technologies) while maintaining very low production costs.

As previously stated, for the time being, this is a research-based field without commercial application, so there exists no such device as of today and third generation solar cells are limited to laboratory research. Several research groups and industrial partners have theories for how to surpass the Shockley-Queisser limit. These theories are, for example, based on manipulations of incoming light or the absorbing material, such that electrical and optical losses in the device will reach a bare minimum.

1.1.4. PV Module and System: Costs and Forecasts

The large variety of PV applications allows for a range of different technologies to be present in the market, from low-cost, lower efficiency technologies to high-efficiency technologies at higher cost. Fig. 1.4 gives an overview of the efficiency and cost projections for first, second and third generation PV technologies.

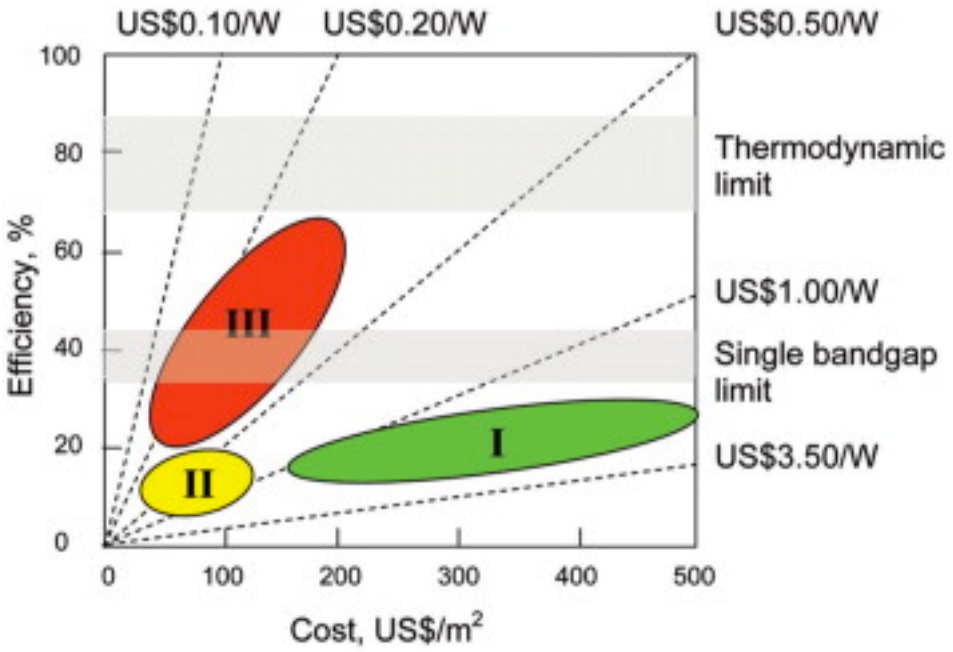

Fig. 1.4. Current efficiency and cost projections for first, second and third generation PV technology. Source: University of New South Wales.

Conversion efficiency, defined as the ratio between the produced electrical power and the amount of incident solar energy per second, is one of the main performance indicators of PV cells and modules. They can also be used in building-integrated systems (BIPV) or be ground-mounted, for example, in large-scale, gridconnected electricity production facilities.

The investment costs of PV systems are still relatively high, although they are decreasing rapidly as a result of technology improvements and economies of volume and scale. High investment costs, or total system costs, represent the most important barrier to PV deployment today.

Total system costs are composed of the sum of module costs plus the expenses for the "balance-of-system", including mounting structures, inverters, cabling and power management devices. While the costs of different technology module types vary on $ per watt basis, these differences are less significant at the system level, which also takes into account the efficiency and land-use needs of the technology. Total system costs are sensitive to economies of scale and can vary substantially depending on the type of application. For example, the lower cost (per watt) to manufacture some of the module technologies, namely thin films, is partially offset by the higher area-related system costs (costs for mounting and the required land) due to their lower conversion efficiency.

1.1.5. Motivation for Thin-film Solar Cells

In the previous paragraph we already stated that the benefits of thin-film solutions are represented by the reduced production costs and increased production rate respect to classic Si wafer-based modules. The Thin-Film Solar Cells (TFSC) are in fact based on materials that strongly absorb sunlight so that the cells can be very thin (1–3 micrometers). The electrons freed by the photons need to travel only this short distance inside the cell to the cell contacts (and from there to the external circuit to produce power). This reduces the demand for high purification and crystallinity of the material, one of the causes of the high cost of the Si cells. However, where the thin films have a real business advantage is that they are made directly into modules and not in cells. In other words, while Si cells are manufactured from wafers, then processed and assembled to form a module, in TFSC technology many cells are made and simultaneously formed as a module.

The TFSC manufacturing process is designed such that they are deposited sequentially on moving substrates as in a continuous 'in-line' process or on many substrates at a time in a stationary batch process. This minimizes handling and facilitates automation, including laser scribing, to isolate and interconnect individual cells on the module, called monolithic integration. They are deposited at relatively low temperature (200–500°C compared with ~800–1450°C for the different main processes of c-Si). TFSC are either polycrystalline with small ~1 μm sized grains such as Cu(InGa)Se2 or CdTe, amorphous like a-Si, or mixed amorphous/crystalline Si phases called nanocrystalline Si. The noncrystalline structure is a consequence of being deposited at temperatures too low and at rates too fast to allow perfect crystalline bond formation. TFSC typically consist of 5–10 different layers whose functions include reducing resistance, forming the *pn* junction, reducing reflection losses, and

providing a robust layer for contacting and interconnection between cells. Some of the layers are only ~20 atoms thick (10 nm), yet they may be a meter wide! This requires excellent process control.

However, in addition to all these advantages, there are weaknesses that hamper thin-film development on the market. The efficiency of TFSC modules is in fact 25–50% lower than for classical Si modules which makes it difficult to translate the low cost per m^2 of TFSC modules to cost per Wp. To obtain low manufacturing costs, TFSC plants must be operated at high volume throughput to offset the initial capital investment. In addition, the lower efficiencies of TFSC have a much less-developed knowledge and technology base compared with c-Si, and their properties are more difficult to control.

One of the the strengths and remaining challenges for the TFSC industry is the usage of Amorphous Si.

1.2. Amorphous Silicon-based Solar Cells

Amorphous silicon (a-Si) has been studied for many decades because of its many advantageous properties over traditional crystalline silicon (c-Si). In particular, amorphous silicon as material can absorb light more effectively than its crystalline brethren due to the larger number of allowed optical transitions as a result of the disordered structure. Unfortunately, this disorder also reduces charge transport, making photo-generated electron-hole pairs difficult to collect as current. Even that the main advantages of using amorphous silicon as a photovoltaic material is due to its ease of fabrication and to a low-cost solution to electricity generation from sunlight, overall amorphous silicon is at a disadvantage since its devices have a lower fill factor and current density. Using chemical vapor deposition, indeed, large area cells and modules can be made commercially in a roll-to-roll process or similar. Thus, amorphous silicon solar cells are found in low cost applications regardless of the limited efficiency. Amorphous silicon is also easy to deposit on a multitude of substrates because of its low fabrication temperature. Possible substrates include glass, plastics, and various metal sheets. Of these substrates, some are thin, cheap, and flexible. This opens the opportunity for a-Si cells to be made for flexible applications, like portable chargers for consumer electronics or shingles for building integration. Besides poor transport properties, the main disadvantage of amorphous silicon is the degradation of efficiency that occurs when exposed to sunlight. While this immediately seems to contradict the purpose of the device, the degradation eventually saturates at manageable efficiency levels.

1.2.1. Choice of a-Si:H for PV Thin-film Technologies

In the previous paragraph it was shown that thin-film photovoltaic has become a low-cost solution to electricity generation from sunlight. Of the available thin-film materials options, amorphous silicon (a-Si) has been studied for many decades. Amorphous Si is deposited from hydride gases such as SiH_4 using plasma to decompose the gas. This is called *Plasma-Enhanced Chemical Vapor Deposition* (PECVD) and allows for large areas to be coated rather uniformly and with excellent control, using the same technology as large-area flat panel displays. The a-Si film has 1-10% hydrogen bonded to the Si, and is often designated as *a-Si:H*. The H atoms passivate a large number of the defects resulting from the incomplete bonding of the Si atoms. The atomic structure lacks the long-range order of other crystalline or polycrystalline materials. In particular, amorphous silicon as a material can absorb light more effectively than its crystalline brethren due to the larger number of allowed optical transitions as a result of the disordered structure.

Films are typically deposited between 150 and 250°C, the lowest temperature of any of the TFSC materials, allowing the use of lower-cost, low-temperature substrates. a-Si solar cells are deposited on glass, stainless steel foil, or plastic. The last two substrates are flexible allowing for "roll-to-roll" manufacturing where all the layers are deposited as the roll moves through their process zone. Nearly all a-Si modules contain multiple junction devices where two or three junctions are grown on top of each other. This allows for more efficient utilization of the sunlight. The three major challenges for a-Si technology are the following:

- To improve the standard module efficiency to 10–12%;
- To minimize or eliminate the self-limited degradation which reduces efficiency by 2–3% (absolute);
- To increase the deposition rate of the layers and utilization of the gases, especially the nanocrystalline layer to allow faster, lower-cost manufacturing.

1.2.2. Structure and Doping of Amorphous Silicon

Talking about amorphous and crystalline silicon, the difference in material structure is revealed by the name of each substance. While c-Si offers a crystalline structure, with regular bond lengths and angles throughout the material structure, a-Si:H does not provide such long-range order. Therefore, the a-Si:H material structure is complex and unpredictable and really, a coherent and full understanding of the microstructure of a-Si:H is nowadays lacking. The random variations in bond lengths and angles in a-Si:H lead to certain very different combinations. Consequently to the non-crystalline structure, a

regular bond between the atoms will not form, thus leaving behind unpaired connections in the amorphous network, known as *Dangling Bonds* (DBs). Dangling bonds are denoted as *coordination defects,* which entails a mismatch between the coordination numbers of adjoining atoms in a material, i.e. number of atoms which an atom is energetically disposed to bond with. *Such* coordination defects block the movement of free charge carriers within the material structure, compromising the material conductivity. Moreover, recent studies of the amorphous material structure indicated the presence of other types of defects than solely DBs [14]. Initially, the large defect density in a-Si material, was so to render the material unsuitable for a PV approach [13].

During initial characterization studies, failure to dope the amorphous material was considered a normal consequence to the amorphous structure and its large density of coordination defects – as dopants would assume their natural coordination number and simply form bonds with DBs. This effect is, however, deterred by the presence of hydrogen (H) in the a-Si:H, as the H-atoms passivate (i.e. bond with) DBs in the a-Si:H, thereby reducing the defect density to 10^{15} – 10^{16} cm^{-3} [15]. Therefore an alloy between a-Si and hydrogen, or *hydrogenated amorphous silicon* (a-Si:H) is favorable for solar cell applications, and is the current standard in device grade applications. Therefore, when speaking of amorphous silicon solar cells, it is indeed a-Si:H that is referred to.

1.2.3. Optical and Band Properties of a-Si:H

As stated before, one of the most interesting aspects of amorphous silicon, which also clearly distinguishes it from its crystalline counterpart, pertains to the optical properties of the material.
Crystalline silicon is an indirect bandgap semiconductor, that, in practice, means that the momentum of induced charge carriers must be altered before they can occupy higher energy states (process which requires parts of the absorbed energy).

Amorphous silicon, instead, due to the disorder of the material, acts as a direct bandgap semiconductor. This means that the momentum of the electrons and holes is considered equal in the conduction band and in the valence band. The result of a direct band-gap is that the absorption coefficient of the material is much higher. As the charge carrier momentum mismatch is not an issue, more of the incident irradiation may actively participate in charge carrier transition across the band gap. In the visible part of the solar spectrum, a-Si:H absorbs up to two orders of magnitude more than c-Si. Due to this, a very thin layer of a-Si:H (1-μm) is sufficient to absorb almost all the light spectum [13].

Referring to the band structure, as previously reported, crystalline silicon material has well-defined energy bands and ranges. Hydrogenated amorphous silicon, instead, is energetically represented by a continuous distribution with no abrupt cessation of states between valence and conduction bands [13]. Due to the long-range disorder in the a-Si:H network, in fact, certain energetic states of the valence and conduction bands are located within the traditional band gap.

As depicted in Fig. 1.5, electronic properties of all amorphous semiconductors can be explained in terms of the energy distribution of their Density Of States (DOS) function, g(E). The DOS function has well-defined energies Ev and Ec that separate extended states from localized states.

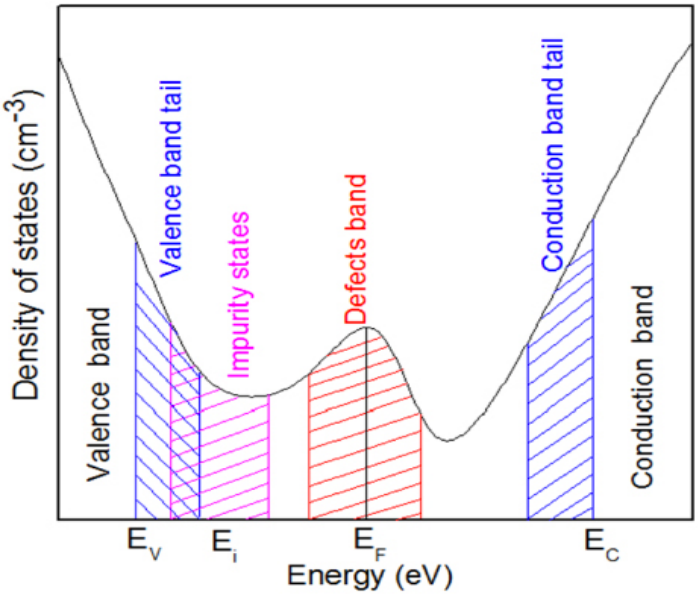

Fig. 1.5. Electronic Density of States (DOS) in a-Si:H. © Wikimedia Creative Commons Licence.

There is a distribution of localized states, called tail states below Ec and above Ev. The usual bandgap Ec-Ev is called the mobility gap. The reason is that there is a change in the character of charge transport, and hence in the carrier mobility, in going from extended states above Ec to localized states below Ec. Electron transport above Ec in the conduction band is dominated by scattering from random potential fluctuations arising from the disordered nature of the structure. The electrons are scattered so frequently that their effective mobility is much less than what it is in crystalline Si. Electron transport below Ec, on the other hand, requires an electron to jump, or hop, from one localized state to another, aided by thermal vibrations of the lattice. As know, indeed, the jump or diffusion of the impurity is a thermally activated process because it relies on the thermal vibrations of all the crystal atoms to occasionally give the impurity enough energy to make that jump. The electron's mobility associated

with this type of hopping motion among localized states is thermally activated, and its value is small. Thus, there is a change in the electron mobility across Ec, which is called the conduction band mobility edge. The localized states (frequently simply called traps) between Ev and Ec have a profound effect on the overall electronic properties. The tail localized states are a direct result of the structural disorder that is inherent in noncrystalline solids, variations in the bond angles and length. Various prominent peaks and features in the DOS within the mobility gap have been associated with possible structural defects, such as under – and overcoordinated atoms in the structure, dangling bonds, and dopants. Electrons that drift in the conduction band can fall into localized states and become immobilized (trapped) for a while. Thus, electron transport in a-Si:H occurs by multiple trapping in Shallow localized states.

1.2.4. The p-i-n Junctions in a-Si:H Solar Cells

Typically a-Si:H cells are made from a p-i-n structure instead of the p-n junction common for crystalline silicon cells. This is a consequence of poor carrier transport, requiring drift to assist with carrier collection. In fact, defect-compensated donors and acceptors in the doped layers cause increased recombination rates, thus lowering charge carrier *mobility* and *lifetime* in the material. For this reason, a relatively thick intrinsic a-Si:H layer is sandwiched between thin n-doped and p-doped a-Si:H layers. The doped layers ensure that an electric field is generated across the solar cell, while the intrinsic layer acts as the absorber layer of the solar cell device.

So, although similar to a p-n junction, the physics of a p-i-n junction is different based on transport aided by a built-in electric field provided by the separation of quasi-Fermi levels in the heavily doped regions. In addition, carrier transport in a-Si is controlled by mid gap defects which act as recombination centers. Next figure shows the physical structure and energy band diagram of a *pin-device*. Normally, the separation between quasi-Fermi levels in the p^+ and n^+ regions creates a built in electric field which generates a depletion region at the junction. In a p-i-n device the transition between p^+ and n^+ regions takes place uniformly throughout the intrinsic layer. Thus, the built-in electric field in thermodynamic equilibrium is roughly linear in the i-layer allowing any photo-generated carriers to be swept to their respective contacts for collection. Increasing bias decreases the strength of the field while negative bias augments it. This is simplified by stating that p-i-n solar cells depend on drift of carriers whereas p-n cells primarily operate based on diffusion.

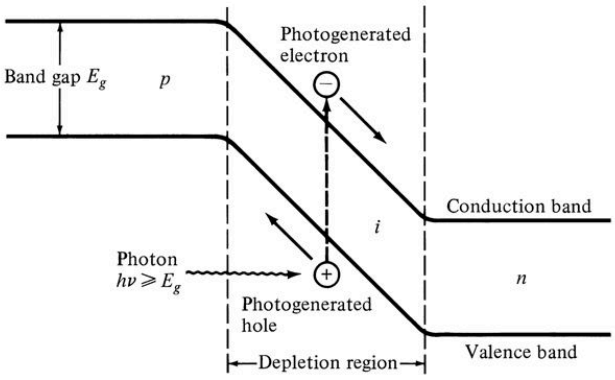

Fig. 1.6. Energy band diagram for a p-i-n junction. © Wikimedia Creative Commons Licence.

This device structure is beneficial for overall charge transport due to a combination of two a-Si:H material properties. Firstly, holes have a mobility-lifetime product in intrinsic a-Si:H material which is considered to be lower than that of electrons, meaning that they will recombine sooner as they propagate through the intrinsic layer. Secondly, the absorption spectrum of a-Si is such that light is not absorbed homogeneously throughout the intrinsic layer, where a higher proportion of incoming sunlight is absorbed in the first couple of nanometres (nm) of the material [13]. Thereby, employing the device structure as seen in Fig. 1.6 will infer the least possible amount of losses during charge carrier transport through the device. Meanwhile, it should also be noted that the nip-configuration is successfully employed in solar cell fabrication.

1.2.5. Efficiency Losses and Recombination

Collection losses are considerated as one of the biggest problems in the design of solar cells, especially in the case of amorphous silicon, since it is a defect-rich material. Normally, the problems due to failure of charge carrier collection, can originate from two different strategic zones: in the *bulk* material, i.e. where the carriers are generated and separated, or at the contact interfaces, i.e. where the carriers are physically collected. In both cases, the collection loss is due to the process of recombination. Such process, complimentary to the generation of charge carriers by photons, is the process by which two charge carriers of opposite polarity annihilate each other. Among the recombination processes we can distinguish 3 different types: *Band-to-Band* recombination, *Auger* recombination, and *Shockley-Read-Hall* (SRH) recombination.

We are in the case of band-to-band recombination when an electron from the conduction band recombines with a hole present in the valence band, emitting a photon as result of the process. The

wavelength of the emitted photon corresponds, in this case, to the energetic difference between the hole and electron involved.

Auger recombination shows up when an electron gives off its excess energy upon recombination to another electron in the conduction band. The recipient electron experiences an increased kinetic energy, and most likely thermalizes shortly after.

SRH recombination instead, is a defect where a hole and an electron recombine by means of an intermediate defect site in the band gap. The energetic requirement for this transition is less than in the two other cases, and is therefore more frequent in defect-rich material like a-Si:H material, where both Auger and band-to-band recombination are negligible compared to SRH recombination [13].

1.2.6. The Staebler-Wronski Effect (SWE)

In 1977, Staebler and Wronski discovered that films made from amorphous silicon degrade in quality when exposed to sunlight. After the first few hundreds of hours of illumination ("light soaking"), indeed, the a-Si:H photovoltaic cells have a noticeable reduction of power conversion efficiency, mostly due to the today well known "Staebler–Wronski" effect [16]. This reduction is mainly attributed to dangling bond defects whose density under light illumination increases compared to the initial value, reaching a saturation steady-state at about 10^{17} cm^{-3} [17,18]. The stabilization of defect concentration in the a-Si:H materials after extended light soaking is probably what renders the a-Si:H PV technology commercially viable.

Although a complete and coherent model for the degradation process is lacking, it is common consensus that the presence of hydrogen within the a-Si:H structure plays a large role in the creation mechanisms of metastable defects. Because hydrogen atoms within the amorphous silicon material pacify DBs in the structural framework, it is believed that such changes in bonding configurations lead to alterations in defect density and defect density distribution. From a basic physics point of view the main idea is that the illumination provides the energy to break the so-called "dilute" H phase and thus creating dangling bonds [19,20]. In fact, a short anneal at about 150 °C can largely restore the solar cell performance. Such effect is also largely responsible for the positive relative efficiency temperature coefficient of a-Si:H solar cells and its very good performance in hot climates [21]. Recent studies show that rather than by thermal annealing the light-induced degradation in the a-Si:H solar cells can be totally recovered by the application of a reverse bias while the cells are exposed to illumination. These works focus on the behaviour of the solar cell power conversion efficiency and fill factor. It was found that the rate of recovery of degradation depends strongly on the electric field, on the temperature and on the light intensity [22,23]. These findings might be due to field emission of either

electrons or holes from the metastable defects rendering these defects charged and therefore mobile or to hydrogen ion motion, possibly on the internal surfaces of micro voids.

1.2.7. Micromorph Solar Cells

Amorphous silicon solar cells can be fabricated in a stacked structure to form multijunction solar cells. This strategy is particularly successful for amorphous materials, both because there is no need for lattice matching, as is required for crystalline heterojunctions, and also because the bandgap is readily adjusted by alloying with Ge or by forming μc-Si. One fundamental concept underlying multijunction solar cells is "spectrum splitting." Consider two *pin* junctions, one deposited on top of the second. The top junction "filters" the sunlight to the bottom junction: photons absorbed in the top cell are removed from the light that reaches the bottom cell. Note that a multiple-bandgap tandem cell does not absorb more photons than the bottom cell would on its own; rather, the top cell absorbs its share photons and converts them to electrons with a higher energy. Thus, there is more incident power converted, not more incident photons absorbed. In this work will be experimentally analyzed the case of a-Si:H / microcrystalline Si tandem solar cells. Tandem solar cell consisting of a microcrystalline silicon bottom cell and an amorphous silicon cell stacked on top, usually known as "micromorph" solar cells, are considered as one of the most interesting new thin-film silicon solar-cell concepts. Micromorph tandem solar cell main advantage over a-Si:H cell and μc-Si:H single-junctions is due to the splitting of the solar spectrum: while the thin amorphous silicon top cell absorbs the blue light, the thicker microcrystalline silicon bottom cell absorbs the red and near-infrared light, allowing, in this way, to cover a wider range of the AM1.5 solar spectrum. One of the most important advantage of the micromorph approach is that through light trapping techniques and intermediate reflector adoption, it keeps the thickness of the amorphous top cell low contributing to a lowering of the production costs and, specially, to reduce the undesired light induced degradation characterized by a noticeable reduction of power conversion efficiency, mostly due to the "Staebler-Wronski" effect. Nonetheless, even that the bottom crystalline cell shows higher stability against light-induced degradation, the a-Si top cell still suffers the degradation phenomenon mainly attributed to dangling bond defects whose density under light illumination increases compared to the initial value.

1.3. Project Purpose

This doctoral project born from the need to actively contribute to the development and advance of Renewable Energy Sources. Studying the various technologies, it is clear that worldwide research in the photovoltaic field is principally oriented not to manufacture solar cells with higher efficiency but, rather, to make the cost per watt cheaper. In this context, one of the most suitable solutions, ready to represent a real alternative to the classic crystalline silicon is given by the so-called second generation solar cells, the thin-film technology and so, relying on the strengths and remaining challenges of the TFSC industry, the usage of Amorphous Si.

Amorphous silicon as a material can in fact absorb light more effectively than its crystalline brethren due to the larger number of allowed optical transitions as a result of the disordered structure. In addition, during the deposition of any of the TFSC materials, the very low process temperature allow the use of lower-cost and flexible substrates, allowing a "roll-to-roll" manufacturing where all the layers are deposited as the roll moves through their process zone. Unfortunately, despite the innumerable advantages, this technology has weaknesses that hamper its expansion in the global market. Among the main faults, one of the main disadvantages is represented by the strong degradation of efficiency mainly due to the SWE effect.

The main purpose of this P.h.D. thesis project was so to find a way to make this technology truly competitive, trying to find the right recipe to counteract the aging of these cells and, why not, try to improve their overall efficiency.

During this study, part of the attention was also addressed towards new thin-film technologies such as the solid–liquid junction Dye-Sensitized Solar Cells (DSSC) that operate on very different principles than an all-solid-state solar cell. Their main attraction is the potential for very low cost even that, also in this case, these fascinating new technologies present many challenges, as strong sensitivity to air and water vapor and poor efficiencies due to a strong instability. Also in this case, the study was conducted in order to counteract the degradation of these cells, trying to make such instability phenomena reversible.

Through the development of suitable electrical and optical conditioning techniques, aim of the research was therefore to gain stability, reliability and an overall performance improvement of second and third generation thin-film solar cells.

Chapter 2

Hydrogenated Amorphous Silicon Solar Cells: light induced degradation analysis

2.1. Theoretical Background

As mentioned in the previous chapter, hydrogenated amorphous silicon solar cells quality is closely linked to the deep defect density and to the light soaking mainly due to the Staebler and Wronski Effect (SWE). The energy states in the amorphous material are categorized as two separate types of states – extended states and localized states. The extended states, both present in the valence and conduction band, are energetically overlapping. This facilitates for free charge carriers to move in the material, i.e. the charge carriers have a certain concentration *and* non-zero mobility. Therefore, the extended states are traditionally considered not so harmful for the amorphous network [13]. The localized states are instead constituted by the tail states and the defect states of the amorphous semiconductor material, i.e. where charge carriers remain trapped giving place to the degradation.

While the definition regarding extended states of a-Si:H is widely accepted from the scientific community, for tail and defect states a clear definition appear more complicated.

The defect states in a-Si:H play a large role in the electronic performance of the material since it is largely accepted that the types of defects, as well as the energetic and spatial distribution of the defects, affect the material, and ultimately, solar cell performance. The most widely accepted theory is that the defect states are similar with dangling bonds in the amorphous network, which ultimately act as trap states and recombination centers [19]. The DBs are considered amphoteric in nature, and present two possible energy transitions for a charge carrier: from neutral state to negative state, and from positive state to a neutral state, where each of these energy transitions involves the capture of an electron. There are several models of SWE, some based on the role of hydrogen and DBs in defect creation and propagation [20,24] and others based on alternative defect nature as vacancies and voids [25]. Current research efforts reveal in fact the presence of other types of defects than mere DBs. Several transitional energies have been identified within the material, suggesting the existence of other

charged states than those incorporated by the amphoteric nature of the DBs [15].

Resuming, to determine the numerous defect states present in the amorphous material is of noteworthy importance to understanding the kinetics of charge carriers within a-Si:H, and, of course, the SWE. The standard model of DOS distribution in a-Si:H states that the defect states are distributed according to two Gaussians, each one centered at a characteristic energy which represents the average energy of transition for an electron to occupy the state.

Despite the undesired Staebler-Wronsky degradation effect has been extensively studied by many authors, definitely rules for the mechanism of light-induced degradation of a-Si:H is still not made. In order to study and limit the Staebler-Wronsky degradation effect, many techniques have been implemented to prevent the formation of defects during the a-Si preparation phase. In the next paragraphs two of the best-known techniques will be discussed.

2.1.1. Thermal Annealing

As known, in the hydrogenated amorphous silicon (a-Si:H), the light soaking produces an increasing of the a-Si dangling bonds in the intrinsic layer resulting in a module power degradation. This degradation process is rapid and reaches a maximum (stabilized power), which depends on the number of junctions (initial degradation).

As any thermodynamic process is defined by an activation energy, it is natural that a certain amount of energy is required in order to create defects, and a certain amount of energy is required to remove them. A light soak can furnish the right amount of energy to create a defect, while a provision of a thermal annealing, contrarily, reverse the process [26].

Shortly speaking, metastability requires an energy barrier between alternative states (e.g. A, B) and creation of defects by external excitation. The recovery process, achieved by the thermal excitation, is descripted in Figs. 2.1 and 2.2.

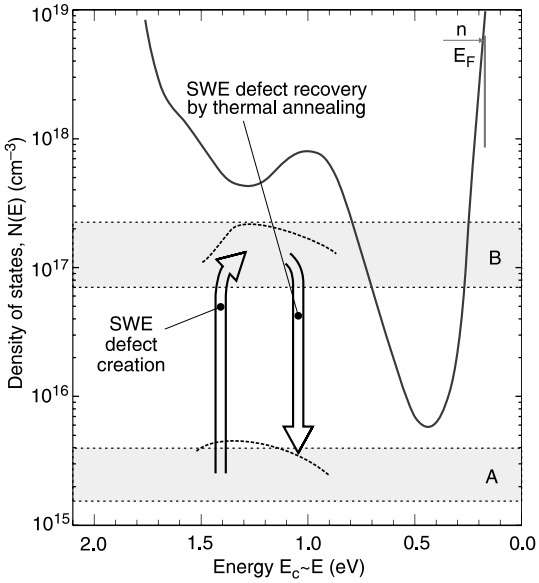

Fig. 2.1. a-Si:H defect density change due to light soaking defect creation and thermal annealing defect recovery. The figure is adapted from [26].

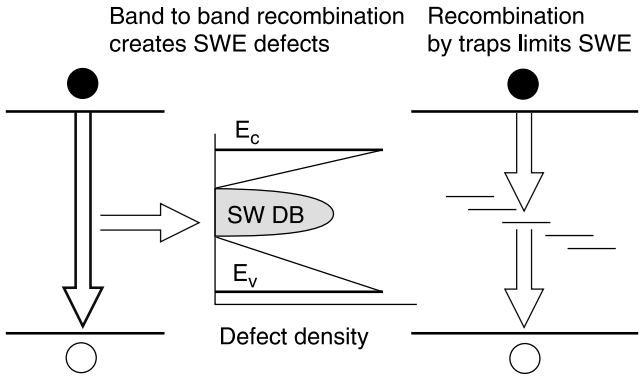

Fig. 2.2. Generation of metastable defects by band-to-band recombination and their recovery through annealing process. The figure is adapted from [26].

The manufacturing process conditions (deposition rate, PECVD plasma frequency, hydrogen on Silane gas dilution amount) are, as known, provide a range of possible activation energies of thermal annealing. Moreover, as the quality of the device degrades, the activation energy of thermal annealing needs to be higher. To conclude, it is possible state that the light induced degradation and thermal annealing are two continuously ongoing processes, resulting in an equilibrium of creation and annihilation of defects.

2.1.2. Hydrogen Dilution

As already introduced in the previous paragraphs, a significant reduction in photodegradation of solar cells and so of the SWE is due to the use of hydrogen (H_2) dilution of silane-processing gas (SiH_4) during film growth [27,30]. Pratically, hydrogen is implemented as an additional feed-in gas to the deposition chamber, which consequently reduces the relative amount of pure silane gas. It is possible in this way to define the hydrogen-to-silane deposition gas quantity, or simply, H-dilution ratio, *R*. Such parameter, as reported in Eq. 2.1, is represented by the ratio of the gas flow rate of hydrogen gas to silane gas that enter the deposition chamber.

$$R = \frac{[H_2]}{[SiH_4]}$$

Eq. 2.1

Imposing a certain hydrogen dilution is believed to increase the structural order of the amorphous material by limiting the silicon bonds in the network, and permitting growth radicals to reach energetic positions which are more favorable [31]. The insertion of hydrogen H_2 as an excess gas during the deposition of a-Si:H based films, increases essentially the etch rate of the growing surface and helps to find energetically more favorable sites leading to a more ordered structure.

The insertion of hydrogen during the deposition of a-S:H strengthens the bonds between the atoms of the a-Si:H structure due to the incorporation of the hydrogen atoms resulting in the increase of the Si-H bonds that have energies higher than Si-Si bonds. Moreover, the increased hydrogen coverage of the growing surface due to higher values of *R* allows for precursors of silicon to diffuse for a longer time before settling in the amorphous structure.

It is important to show here a dependence of SWE on technology and moreover on the level of structural ordering of the amorphous films. If, for istance, it is used a high dilution threshold value, the silicon films become microcrystalline. Just before this threshold is reached, however, it is observed evidence of greater structural order or substantial regions of intermediate range order in the amorphous film.

Despite the great importance of hydrogen during deposition processes, it is useful to know that the amorphous-micro-crystalline phase boundary depends not only on the dilution ratio $R = [H_2]/[SiH_4]$, but also on the film thickness *d* as shown in Figs. 2.2 and 2.3 because the ordered regions grow with the growing film [30,32]. In addition, other important parameters affecting the evolutionary phase

boundary are the following: substrate material, deposition rate and temperature, and the frequency (13.6 or 80 MHz, or microwave) of the plasma-deposition process.

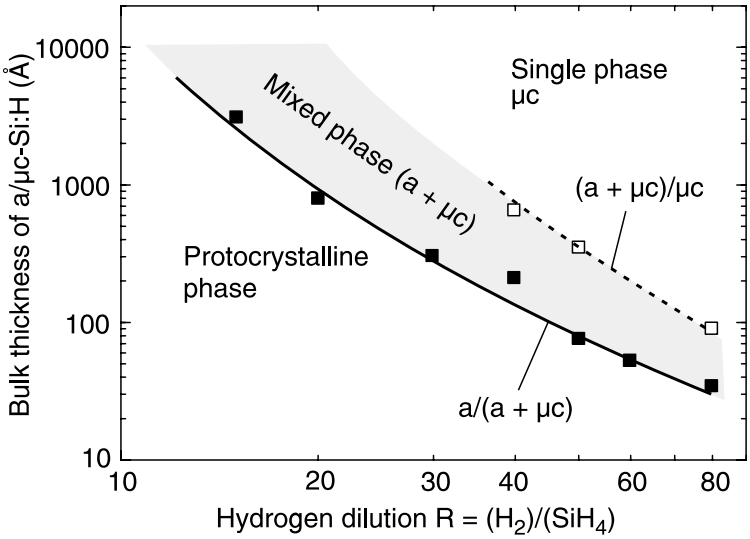

Fig. 2.2. Film thickness, *db*, at which the different phase transitions occur during Si:H film growth in RF PECVD normal process, plotted as a function of the hydrogen dilution ratio R = $[H_2]/[SiH_4]$ using glass substrate. The figure is adapted from [26].

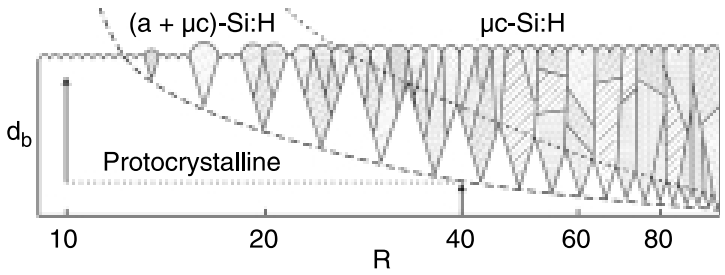

Fig. 2.3. Schematic of the structure of Si:H films prepared as a function of R = [H2]/[SiH4]. The dashed and dotted lines identify the a→(a+μc), and (a+c)→μc transitions, respectively. The arrows denote Si:H i-layer process found to optimize the performance of p-i-n solar cells. The figure is adapted from [26].

2.2. Experimental Analysis

2.2.1. As-Deposited Characteristics of a-Si:H Solar Cells: Effect of Thickness and Hydrogen Dilution on Initial Performance

To define the sample preparation conditions it was studied the role of the H_2/SiH_4 ratio during the PECVD deposition of the a-Si:H layers at 255 °C on the time zero performance of the solar cells, given the important role played by the H_2 dilution [33–34]. Two different typologies of samples using various different dilution ratios R, defined as the H_2/SiH_4 ratio, were prepared and various number of a-Si:H solar cell types were used in this analysis. One group was single-junction p–i–n cells with p and n-type a-Si: H layers of both 20 nm thickness and with the intrinsic (i) layer of either 45 nm or 250 nm thickness. The second group was a tandem a-Si:H/a-Si:H cell where the two i layers were 45 nm and 250 nm, respectively.

The analysed samples had the AGC ASAHI GLASS VU-type as substrate and a ≈700 nm thick SnO_2:F was used as TCO. The p–i–n a-Si:H cells were deposited by Plasma Enhanced Chemical Vapour Deposition (PECVD) at 255 °C. The top contact at the n-type a-Si:H layer was a TCO layer of ZnO:Al (Aluminium doped Zinc Oxide, AZO) of 900 nm thickness deposited by sputtering. In summary, the entire solar cell layer sequences (illustrated in Fig. 2.4) was SnO_2:F/p–i–n a-Si:H/AZO. The final geometries (circular with diameters varying from 0.01 to 0.64 cm) were defined by photolithography and selective etching of the AZO/p–i–n films. The initial power conversion efficiencies of the single junction cells at 1 sun with AM1.5G spectrum illumination were typically about 5.5% with open-circuit voltage of 0.8 V, short-circuit current densities of 12 mA/cm^2 and fill factor of 60%.

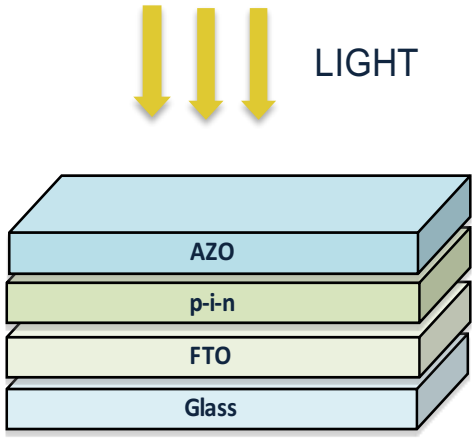

Fig. 2.4. Schematic structures showing the layers sequence.

The solar cells were analyzed by measuring the I–V curves under illumination conditions in a Cascade probe station with micro chamber, with the voltage varying in the -1 to 1 V range by using a HP 4156B semiconductor parameter analyzer. All the I-V measurements were performed in substrate configuration, i.e., with the illumination light entering from the top AZO contact. Illumination with an AM1.5G spectrum of the photovoltaic cells was achieved by using a 92191-1000 Newport solar simulator assisted, in some cases, by a mirror system and Fresnel lens to illuminate the samples either at very low, or, on the contrary, under high sun concentration with high intensity light (up to 30 suns). For the sample temperature control, all the measurements were performed by using a thermostatic chuck with a Temptronic thermal controller working under N_2 flux.

Fig. 2.5 shows the I-V characteristics of these samples measured under AM1.5G spectrum with illumination intensity of 1.5 suns. From the figure it is evident that in each case the samples with R=5 dilution show better short circuit current. The effect is attributed to a better photo-carrier lifetime. In all cases, however, the a-Si:H films are amorphous, not micro-crystalline, and without any clear sign of Si nanocrystals, as shown by Raman and TEM analysis (not reported). Due to the observed effects, in all the experiments on single junction reported in the following part of the thesis, were used a-Si:H solar cells with 250 nm i layer and prepared with a dilution R equal to 5.

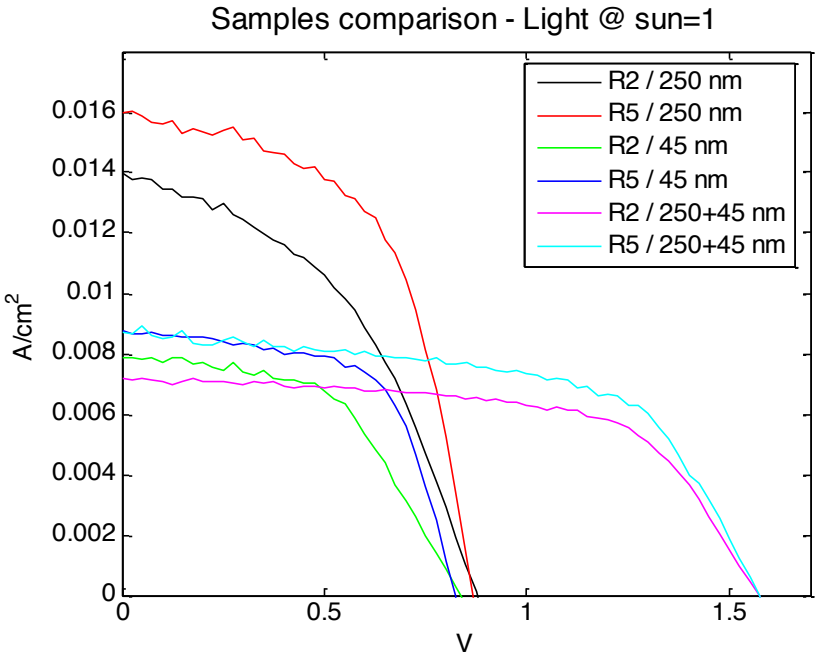

Fig. 2.5. Solar cells comparison showing the differences between the two hydrogen–silane ratios (R=2 and R=5) combined with the three different intrinsic thickness layers (i=45, i=250 and i=45+250).

2.2.2. Role of Light Intensity on Degradation Characteristics

As second step, to define a reference baseline for the further analyzes, it was studied the degradation of the solar cells under light soaking in short circuit conditions, observing the well-known Staebler-Wronski a-Si:H ageing effects [35-41].

To speed up the solar cell wear out, it was increased the intensity of the incident light through illumination under concentration to a large number of equivalent suns. Fig. 2.6 shows the comparison of the solar cell parameters under prolonged light soaking in short circuit condition of the samples with i = 250 nm and R =2 and 5.

Even in this case, independently on the light intensity, a larger H_2/SiH_4 ratio leads to a better solar cell power conversion efficiency, both at time zero and under light soaking conditions.

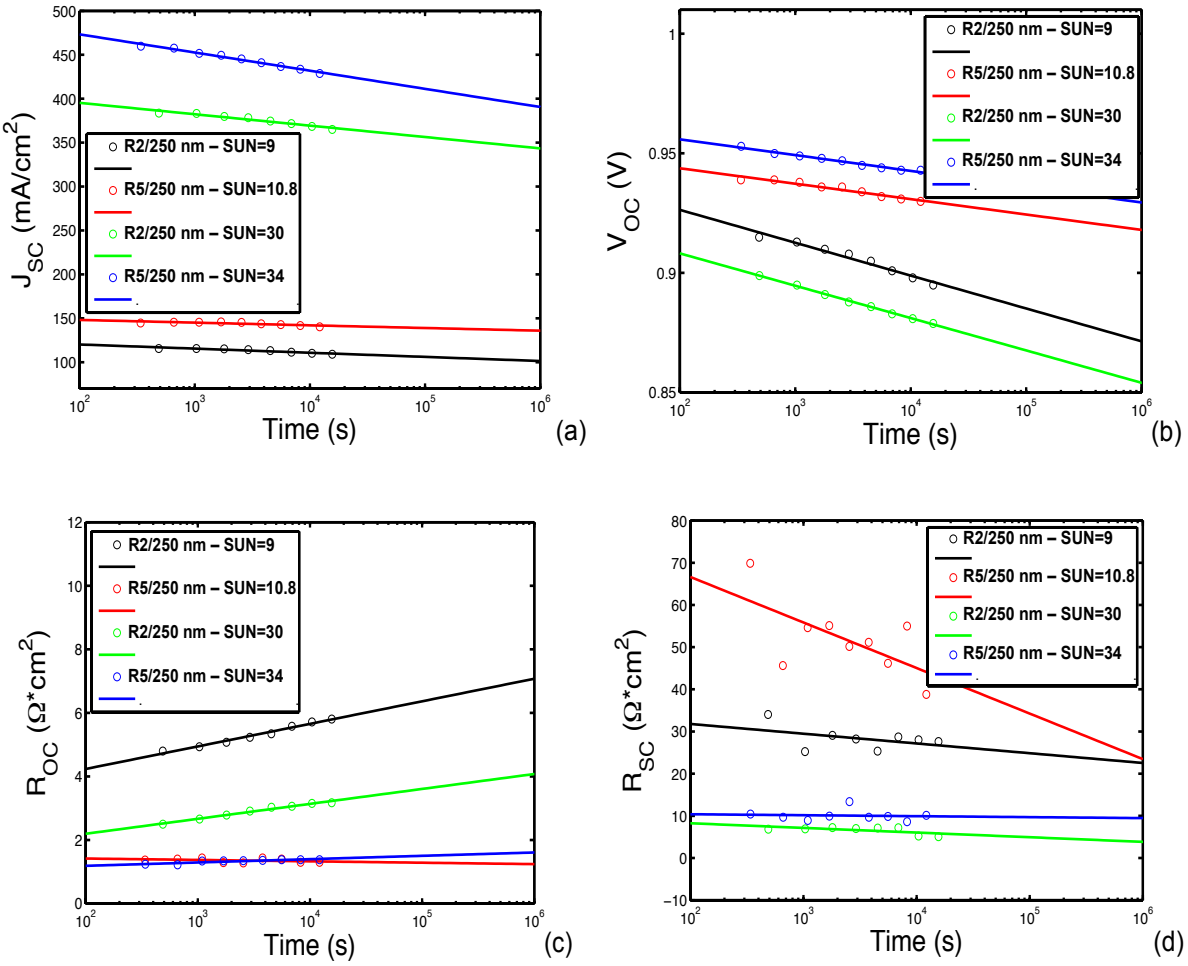

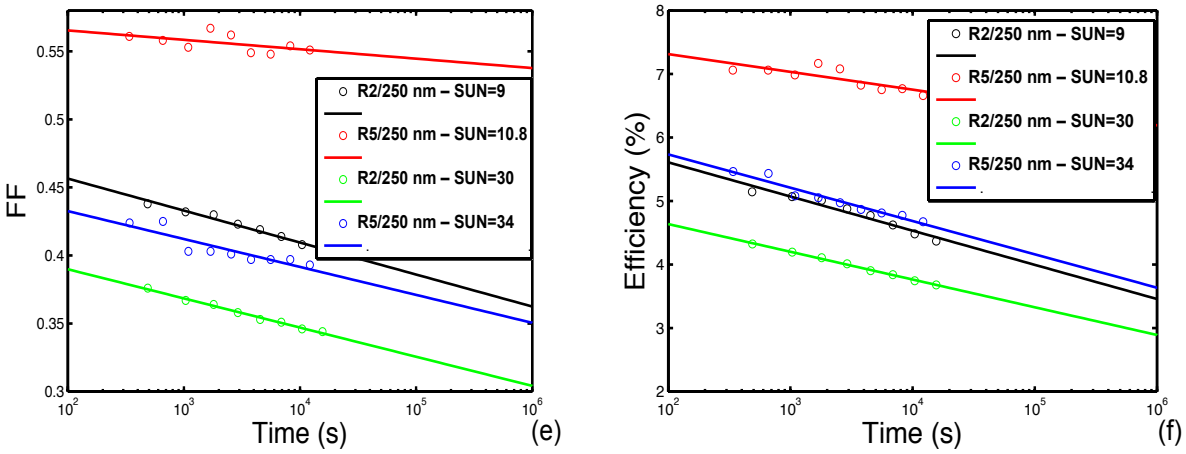

Fig. 2.6. Data trend analysis for (a) J_{SC}, (b) V_{OC}, (c) R_{OC}, (d) R_{SC}, (e) FF and (f) Efficiency as function of stress time for two H_2/SiH_4 ratio (R=2, 5) and for two different light intensity levels (~10-30 suns).

The light soaking effects are attributed to either to H-related defects or to D-centers [19], [33-36]. In the examined case the best samples with better efficiencies and lower ageing effects are those with larger amount of hydrogen (R=5), so we speculate that rather than H-related defects, here the dominating defect is the D-center that is better passivated by larger H content.

Moreover, to study in details the degradation of our solar cells, it was analyzed the effect of light soaking stress under short circuit conditions on all the major solar cell parameters/figures of merit for four different light illumination levels. As expected, under this condition it is observed an increasing solar cell degradation as a function of stress time, and the degradation rate is an increasing function of the incident light intensity (Fig. 2.7). In particular, the decrease of efficiency under light soaking becomes larger as the light intensity rises.

The solar cell efficiency, the J_{SC}, and V_{OC} parameters get worse with the stress time, with an approximately linear trend when plotted in a semi logarithmic scale, i.e. as a function of the logarithm of stress time. Series resistance has a more complex behaviour, dependant upon the illumination levels. At high illumination, as the other parameters, it also worsens with stress time.

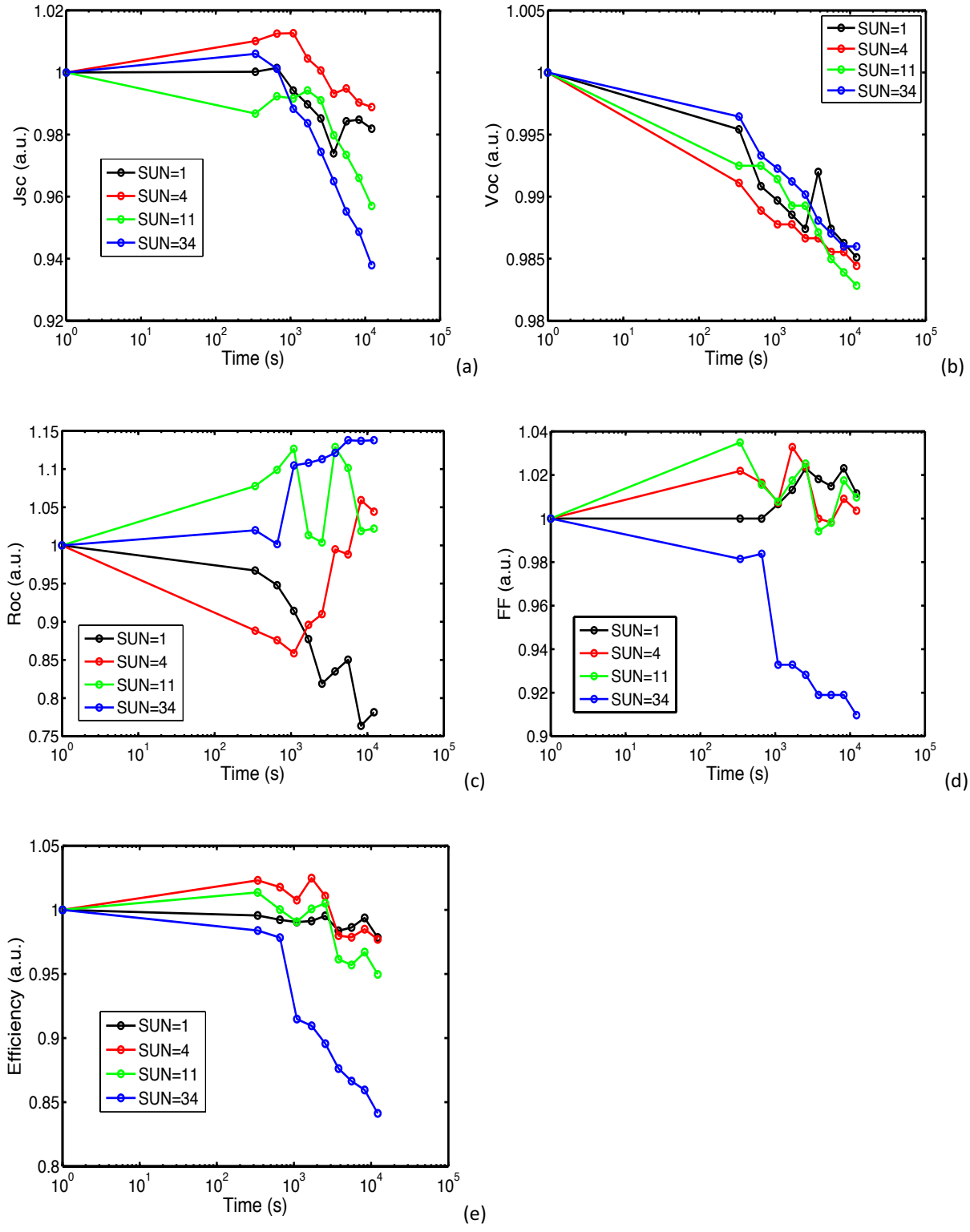

Fig. 2.7. Normalized data trend analysis (short circuit conditions) for (a) J_{SC}, (b) V_{OC}, (c) R_{OC}, (d) FF and (e) Efficiency as a function of light soaking time for increasing sun intensity.

Fig. 2.8 reports the normalized J_{SC} vs. time renormalized for the number of suns: J_{SC} and the stress time are, respectively, divided and multiplied by the number of suns for the various experiments, going from 1 to 34 suns.

Such coordinates are justified by the fact that J_{SC} is proportional to the illumination intensity while one expects that the wear out rate is proportional to the light intensity. It is evident that all curves collapse in a single one, and this justifies the above hypothesis. So we conclude that the light-soaking rate is actually proportional to the illumination intensity.

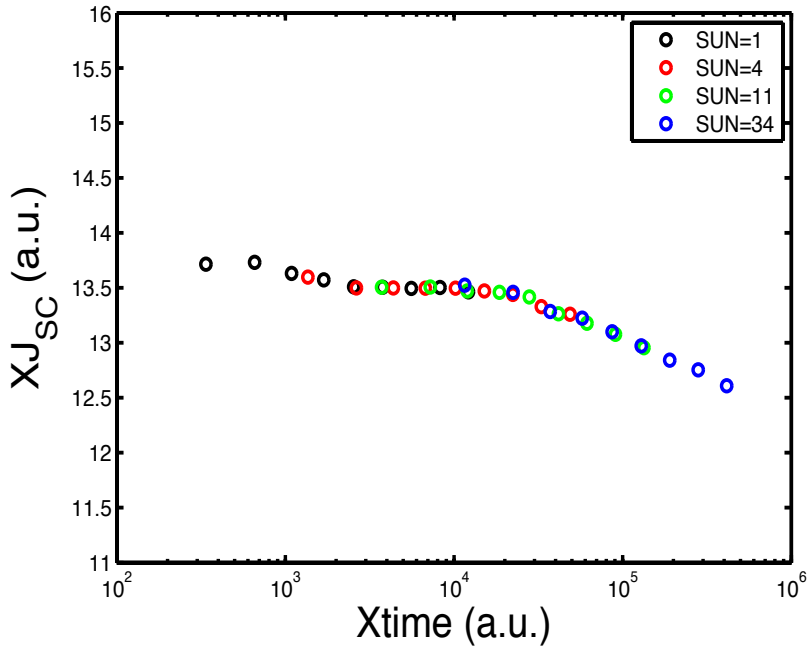

Fig. 2.8. Data trend analysis for normalized J_{SC} as a function of stress time renormalized for the number of suns.

Chapter 3

a-Si:H solar cell performance improvement

3.1. Reversing Light Induced Degradation

In the previous chapter it was shown how the decrease of efficiency under light soaking becomes larger as the light intensity rises. In this section, will be studied appropriate techniques useful to recover the initial efficiency of the cells and, why not, try to improve their overall performances.

3.1.1. Bias Effect

Starting from the previous chapter analysis as baseline in short circuit conditions, it was analysed how the application of a reverse bias to the cells during the light soaking changes the wear out kinetics. Fig. 3.1 shows an example of a sequence of I-V measurements on a solar cell stressed for various times, up to 11,000 s, at -12 V reverse bias and at 1.5 suns illumination intensity. Fig. 3.1 reports the initial I-V curve of the fresh solar cell and after stress for various times, monitored by temporarily stopping the stress and recording the I-V characteristics. It is evident that the I-V curves are shifting toward higher power conversion efficiencies as the stress time increases, that is, the solar cell characteristics are improving under the reverse bias stress.

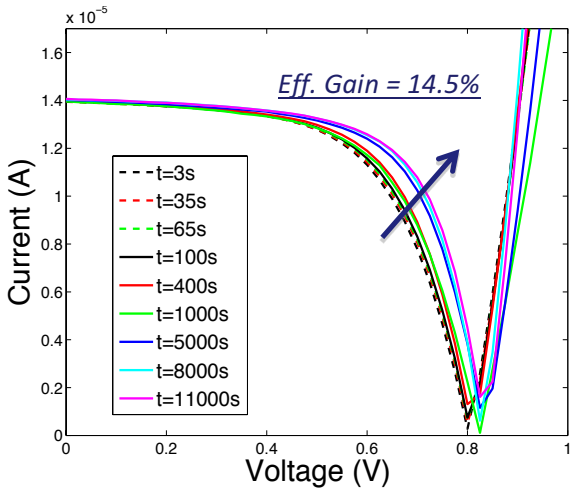

Fig. 3.1. Improvement rate observed applying a reverse bias of - 12 V under a light exposure of 1.5 equivalent suns.

Table 3.1 reports data of the major solar cell parameters / figures of merit as function of the stress time observed during such stress. In fact, the level of reverse bias during stress has a strong effect on the kinetics of the solar cell I-V characteristics evolution.

Stress time (s)	J_{SC} (mA/cm^2)	R_{OC} (Ω cm^2)	R_{SC} (kΩ cm^2)	FF (%)	V_{OC} (V)	Eff. (%)
t = 3 s	11.13	11.61	1.69	60.58	0.802	5.39
t = 35 s	11.14	11.44	1.59	61.00	0.805	5.45
t = 65 s	11.16	11.41	1.56	61.53	0.805	5.50
t = 100 s	11.15	11.33	1.92	61.78	0.806	5.52
t = 400 s	11.15	10.48	1.66	63.02	0.810	5.67
t = 1000 s	11.18	10.84	1.62	61.47	0.822	5.62
t = 5000 s	11.21	10.27	1.82	64.52	0.835	6.03
t = 8000 s	11.24	8.24	2.28	66.48	0.827	6.16
t = 11000 s	11.28	8.26	1.92	66.00	0.835	6.17

Table 3.1. Quantitative evaluation of the solar cell improvement under reverse bias stress. Major solar cell parameters/ figures of merit as a function of stress time at fixed reverse bias of -12 V under a light exposure of 1.5 suns.

To fully understand the effect of reverse bias stress on the cells, we have analysed all the major solar cell parameters/figures of merit. For each stress sequence an initially fresh solar cell was used, and its evolution was monitored in the same way as shown in the example of Fig. 3.1.

The major cell parameters as a function of the stress time for different levels of reverse bias at room temperature and at 1.5 suns illumination level are reported in Fig. 3.2. From the data of Fig. 3.2 it is evident that under reverse bias stress the solar cell characteristics improve, and that the rate of such improvement increases with the applied reverse bias.

These results suggest that the electric field plays a major role, so this instability may be linked to the motion of some charged atomic/molecular species, as better put in evidence by further experimental data reported in the last part of the work.

Fig. 3.2 shows that the cells parameters that mostly improve are the series resistance (and as a consequence the fill factor) and the open circuit voltage. Overall, a noticeable improvement of the power conversion efficiency is found at the highest reverse bias.

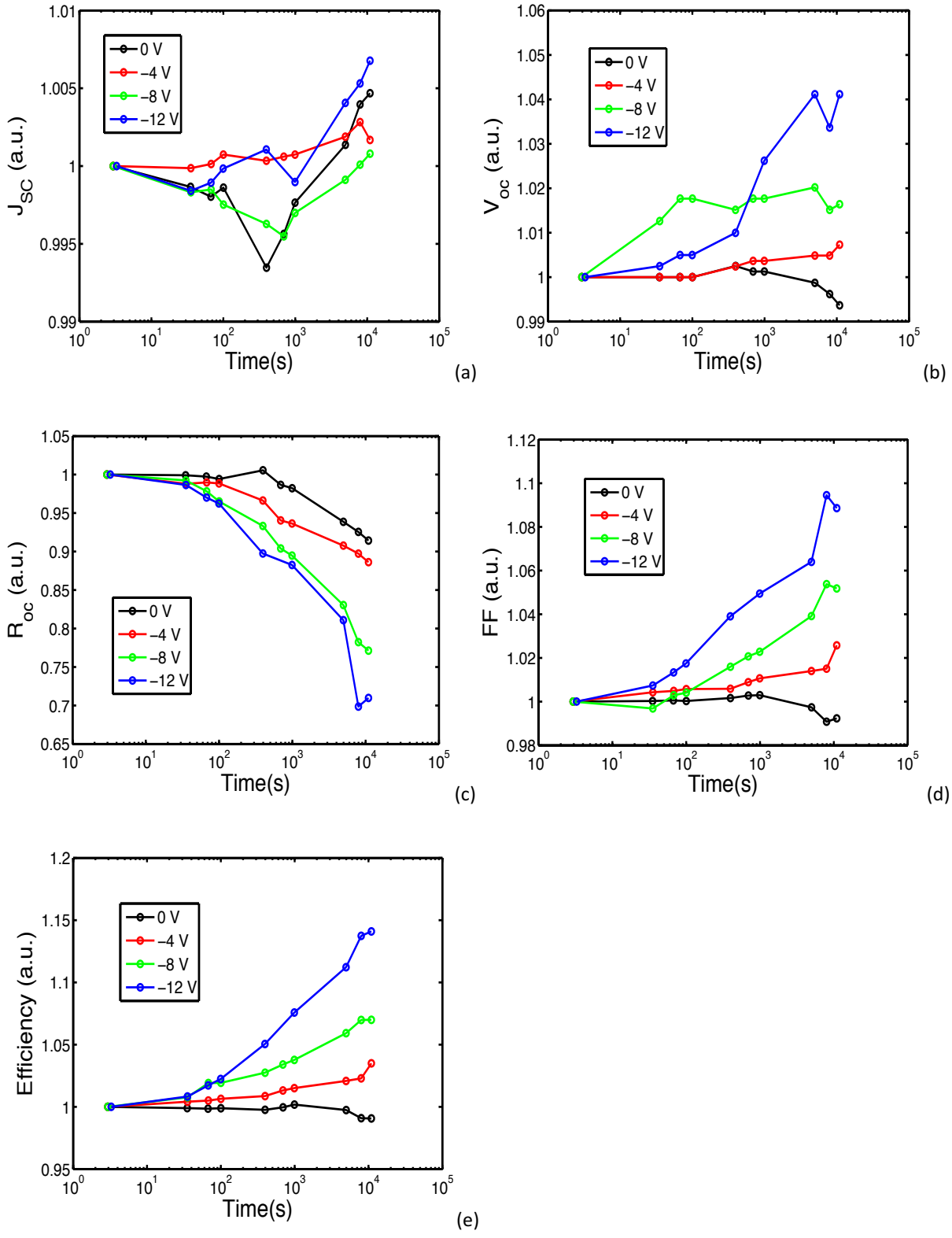

Fig. 3.2. Normalized data trend analysis for (a) J_{SC}, (b) V_{OC}, (c) R_{OC}, (d) FF and (e) Efficiency as a function of stress time for increasing reverse bias voltages under a light exposure of 1.5 equivalent suns.

About the series resistance improvement, it is important to understand which, among the various layers present, is the one dominating. For this purpose, the sheet resistances of the various possible layers have been measured and these correspond to resistivities of the order of 1E-3, 1E+2, and 1E+4 Ω cm for the TCO (AZO and FTO), the n-type a-Si:H, and the p-type a-Si:H layers, respectively. So, if the TCO/doped a-Si:H contact resistances could be considered negligible, for the vertical charge transport the layer dominating the series resistance is the p-type a-Si:H film. If, on the contrary, the contact resistances are those dominating the overall series resistance, then in the current experiments (solar cell in forward bias) the AZO/n-type a-Si:H junction is forward biased while the FTO/p-type a-Si:H junction is reversed biased. So the latter is most likely the dominating contact resistance. In any case the physical layer responsible for the series resistance change is therefore the p-type a-Si:H film.

3.1.2. Combined Bias-Light Effect

The role played by the illumination intensity during the reverse bias stress was also investigated; in suitable conditions it was found that actually the ageing effect is strongly reduced, and, on the contrary, in suitable conditions the light exposure under voltage bias results in an improvement of the I-V characteristics of the solar cell. Fig. 3.3 reports the results on the behavior vs. stress time of the solar cell parameters under reverse bias stresses at -4 V, at room temperature subjected to various illumination conditions. It is evident that by increasing the light intensity the cell parameters improvement rates increase very significantly. These results are in agreement with the previous findings [22], which show that the rate of recovery of light-induced degradation depends not only on the reverse bias level but also on the light level conditions.

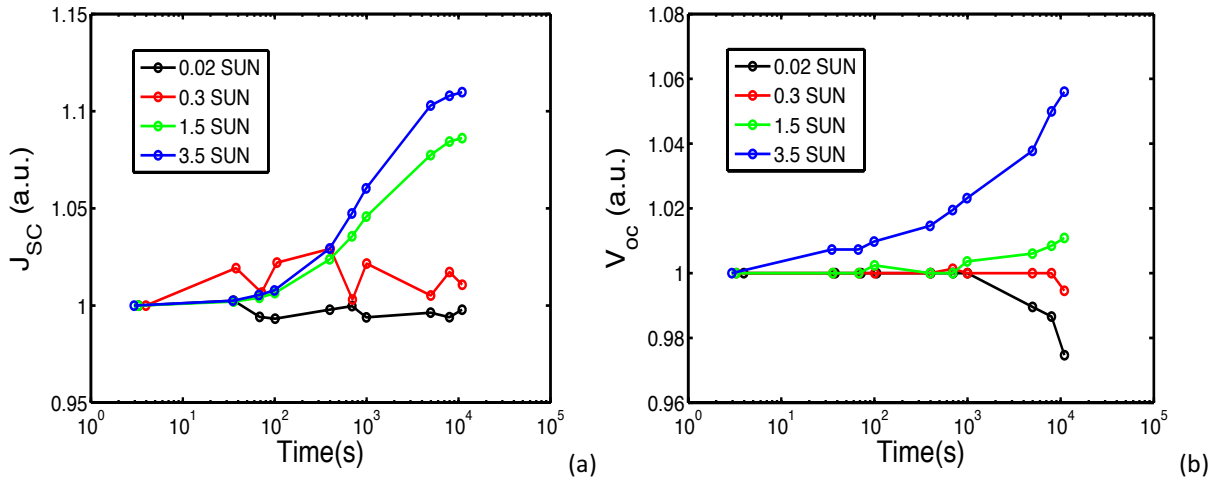

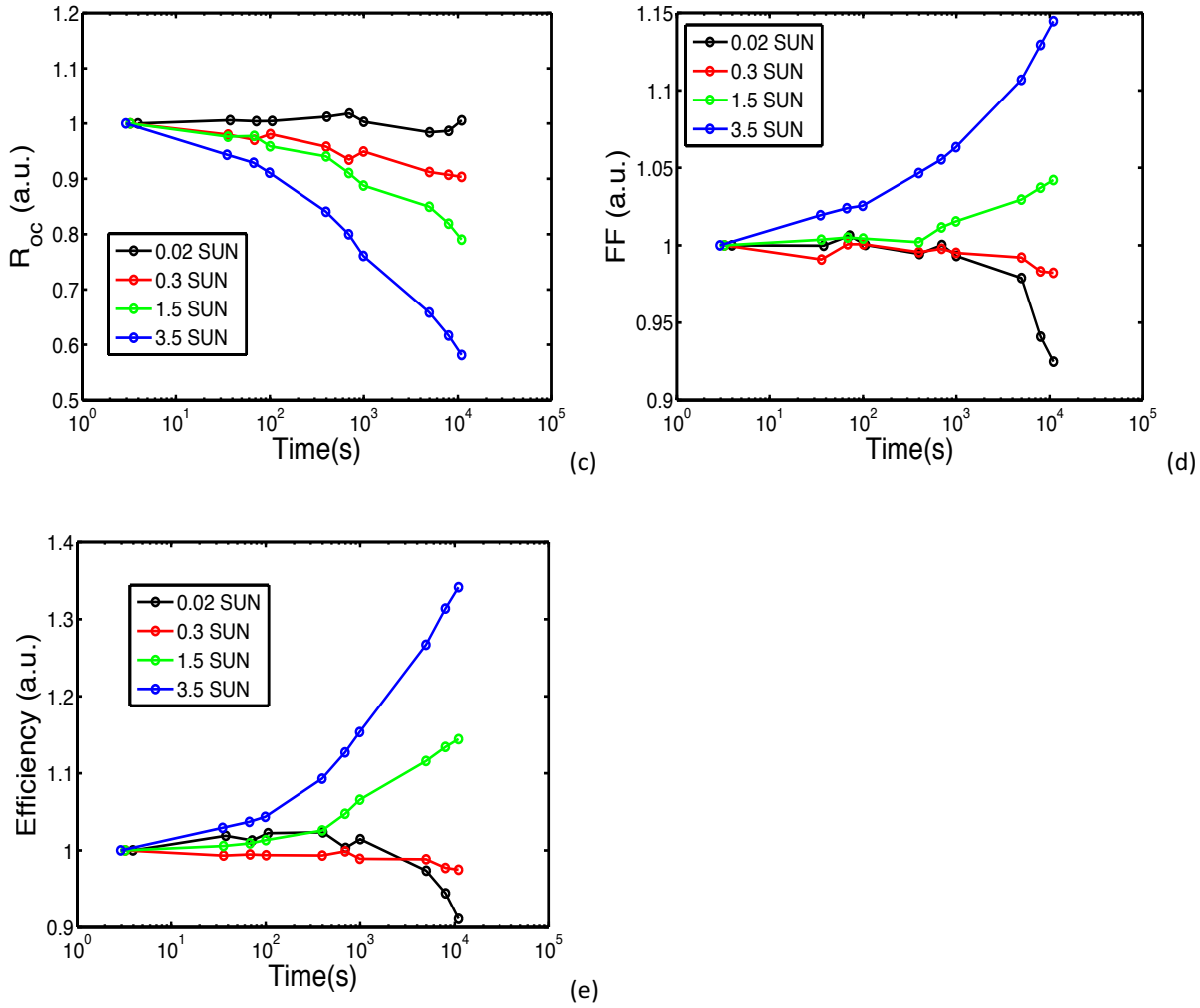

Fig. 3.3. Normalized data trend analysis for (a) J_{SC}, (b) V_{OC}, (c) R_{OC}, (d) FF and (e) Efficiency as a function of stress time for increasing sun intensity at a fixed reverse bias voltage of - 4V.

Here we find that the solar cell performances are not simply recovered but actually noticeably improved. As already shown, the major effect induced by the reverse bias stress under illumination is an improvement of the cell series resistance and therefore of the fill factor.

3.2. Analysis of the Effect of Temperature during Reverse Bias Stress

As reported in the previous paragraph, it was observed that the application of a strong reverse bias stress to the a-Si:H solar cells rather than simply slowing down the wear out rate under light soaking, indeed improves the solar cell characteristics. We have therefore analyzed the role of the solar cell temperature on the improvement kinetics in reverse bias stresses at -12 V under a light exposure of 1.5

suns. Figs. 3.4 show the effect of the solar cell temperature during the stress. It is evident that the largest solar cell improvement effect is around 40–50 °C, which represents in this case the ideal heating treatment. Lower or higher temperatures produce less improvement.

This indicates that the temperature represents a further important factor to be considered in the solar cell recovery/ improvement mechanism. This circumstance may be due to the fact that either the solar cell improvement is related to a short range atomic species diffusion phenomenon or other mechanisms become important at larger temperatures.

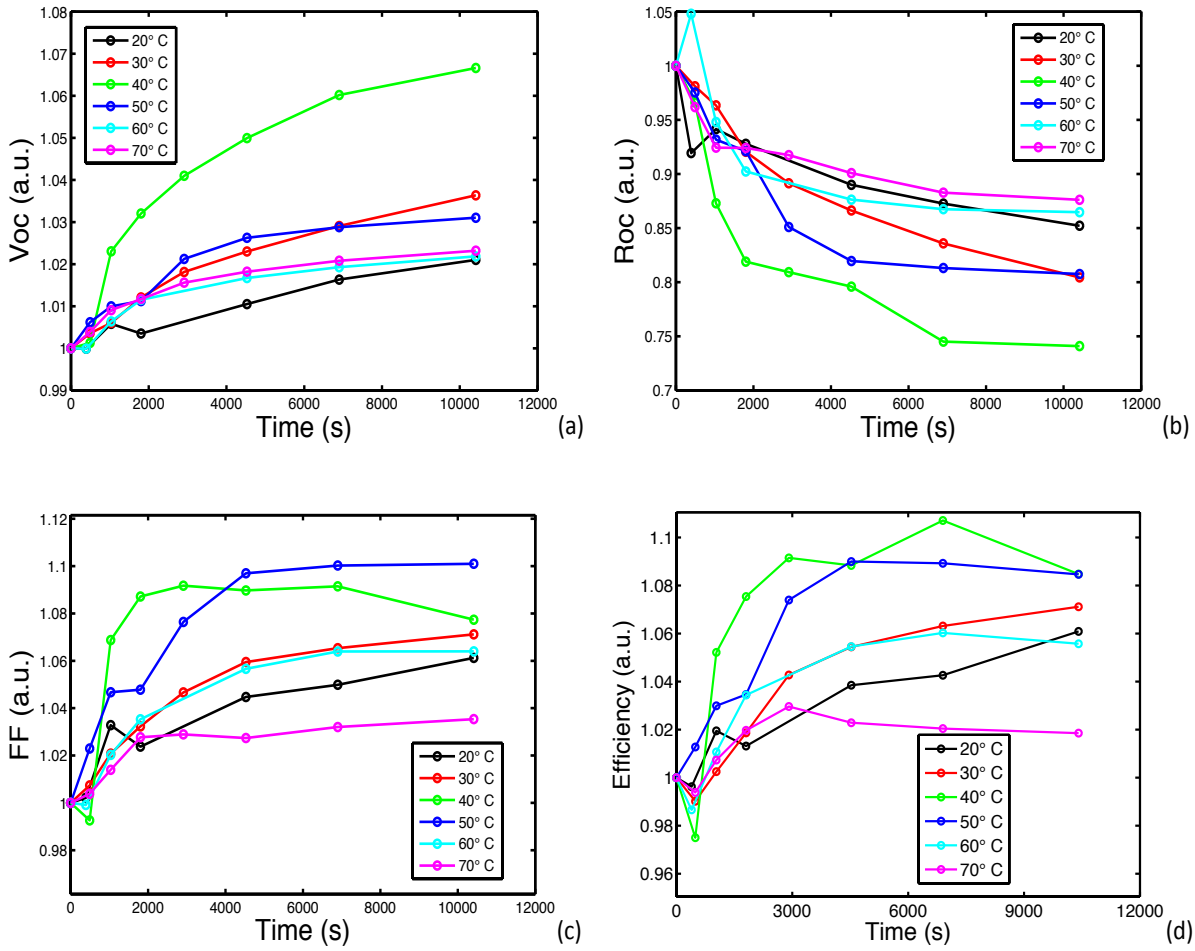

Fig. 3.4. Normalized data trend analysis for (a) V_{OC}, (b) R_{OC}, (c) FF and (e) Efficiency as a function of stress time for increasing temperature intensity observed @ -12 V, 1.5 suns.

3.3. Analysis on Single Layers

To further investigate the kinetics of solar cell parameters improvements, it was studied whether such kind of resistivity changes are directly detected on individual doped a-Si:H thin films too. For this purpose n-type and p-type doped 100 nm thick a-Si:H films were prepared and deposited under the same conditions as those used for the preparation of the p–i–n solar cell stack. These films were deposited on p-type Si substrates covered with a 100 nm thick thermal SiO_2 layer. On such samples we have performed sheet resistance (R_S) measurements by using the four points probe technique. R_S was evaluated in the fresh samples and on these after consecutive substrate bias pulses of 10 s duration applied by using the sequence of pulses described in Fig. 3.5. All measurements and stresses were performed under dark conditions and at 100 °C.

Here the Si substrate acts as a gate in a metal-oxide-semiconductor (MOS) structure since the doped a-Si:H films are separated from the substrate by a 100 nm SiO_2 layer. So a positive substrate bias for the p-type a-Si:H film is a depletion–inversion condition, while a negative substrate bias means an accumulation condition.

Fig. 3.5 reports how, by applying reverse and forward bias voltage pulses in sequence to the single a-Si:H layers in the p-type films the resistance goes up and down following the sign of the applied voltage pulse while in the n-type no monotonic trend change is visible.

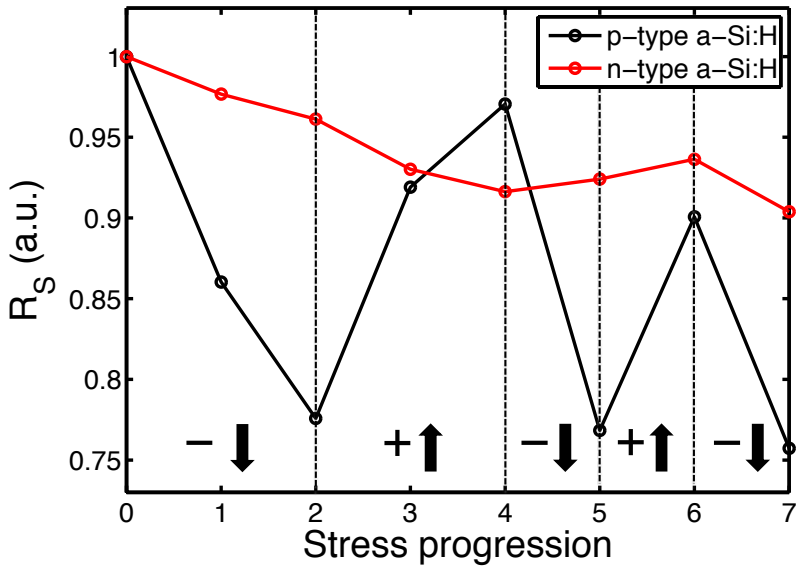

Fig. 3.5. Normalized data trend analysis (conducted in dark conditions and at 100 °C) showing the sheet resistance evolutions of single substrates p and n type a-Si:H. The diagram reveals the different sheet resistance kinetics in response to the contrary voltage bias (-10 V and +10 V).

This suggests that the sheet resistance is modulated by some charged atomic/molecular species which goes up and down, moving from the SiO_2 to the a-Si:H film, and vice versa, at modest temperature (100 °C) by simply following the sign of the electric field. Such large room temperature mobility suggests that we are in the presence of a small atomic species such as H or Li ions, most likely H, given the large concentration of H in the a-Si:H film.

The effect on R_S is much larger for the p-type film compared to the n-type, and this is in agreement with the observation of the improvement of R_S and fill factor of the p–i–n solar cells, heavily influenced by the sheet resistance of the p-type layer rather than the n-type.

3.4. Electrode Material Role

The result of Fig. 3.5 suggests that the change of sheet resistance is due to the motion in and out of ions from the a-Si:H to the SiO_2 film and vice versa, indicating that the improvements in solar cells parameters under reverse bias stress (Figs. 3.1-3.3) are related to the exchange of charged atomic species with the TCO layers. To test such concept we have performed reverse bias stress experiments in samples in which the TCO layer in contact with the p-type a-Si: H film has been replaced by a Mo film, in cells realized starting by a n-type Si wafer covered with SiO_2 for isolation on which a ≈ 700 nm thick Mo film was deposited by sputtering.

The p–i–n a-Si:H cells were deposited, as the previous type of cells, by plasma enhanced chemical vapour deposition (PECVD) under the same conditions at 255 °C. The top contact at the n-type a-Si:H layer was also in this case a TCO layer of ZnO:Al (Aluminium doped Zinc Oxide, AZO) of 900 nm thickness deposited by sputtering.

In summary, the reverse bias stress experiments were performed comparing the solar cell having FTO as bottom contact (illustrated in Fig. 2.4, with solar cell layer sequences SnO_2:F/p–i–n a-Si:H/AZO) with the solar cell having Mo as bottom contact (entire solar cell layer sequences equal to Mo/p–i–n a-Si:H/AZO). The schematic structures comparison showing the layers sequence are shown in Fig. 3.6.:

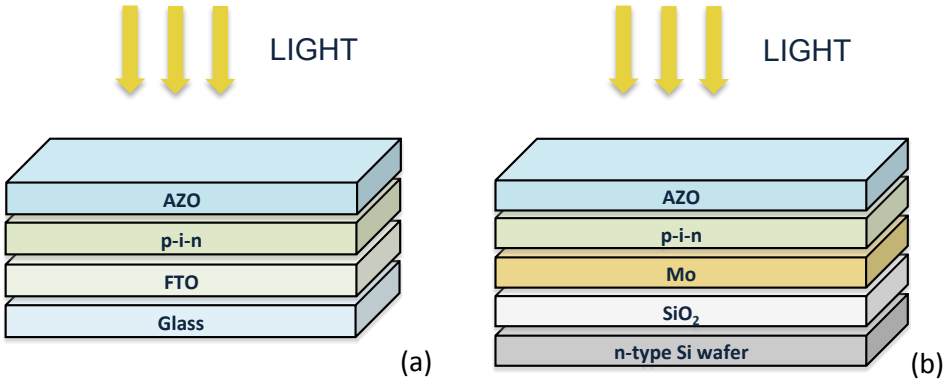

Fig. 3.6. Schematic structures showing the layers sequence of (a) the solar cell having FTO as bottom contact and (b) the solar cell having Mo as bottom contact.

In the case of the cells with Mo bottom contact the efficiencies were typically about 5% with open-circuit voltage of 0.85 V, short-circuit current densities of 12 mA/cm^2 and fill factor of 47%. The differences between these two types of cells are discussed in detail in references [42–44] and they are attributed to differences in substrate texture and photocarrier lifetime.

The use of Mo can give some advantage for the p-type a-Si:H/metal contact resistance and for the solar cell carrier lifetime (compared to FTO) [42,43], and it may be advantageous to fabricate a-Si:H solar cells on flexible substrates [44], and to realise plasmonic light trapping [45].

Fig. 3.7 reports the comparison of reverse bias stress experiments performed on solar cells with FTO as bottom contact layer respect to solar cells having Mo as bottom contact. These experiments were performed at a temperature of 40 °C and under an optical power level (white light source) producing a short circuit current equal to that of an illumination at about 3 suns.

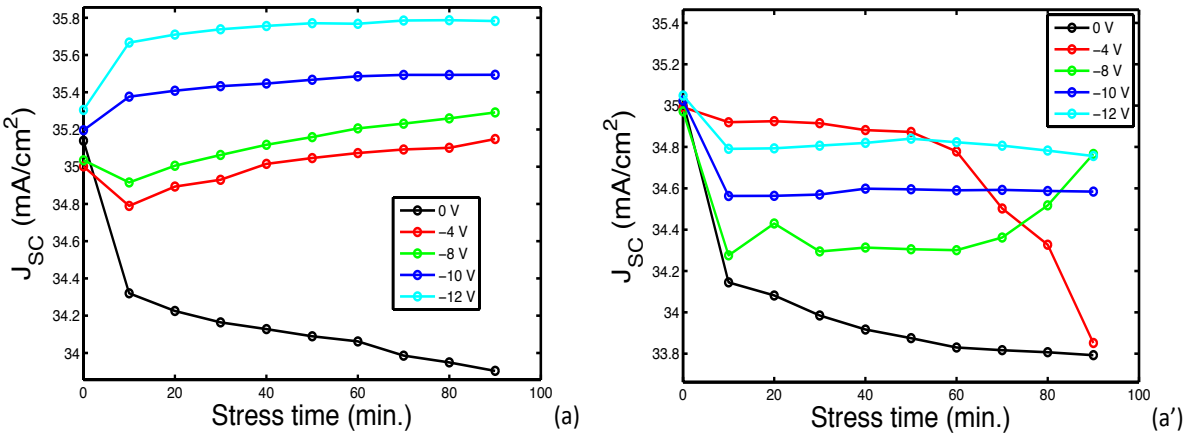

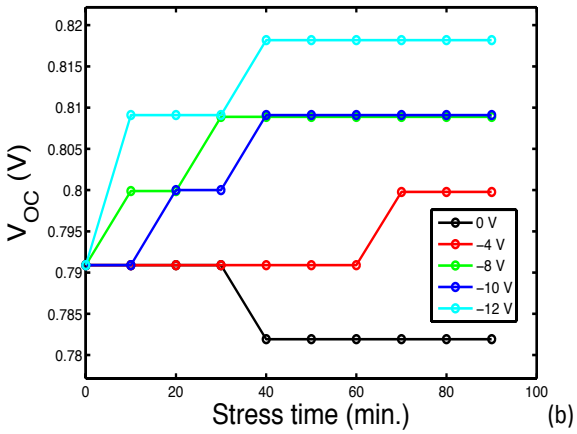
V_OC (V)
Stress time (min.)
0 V
−4 V
−8 V
−10 V
−12 V

(b)

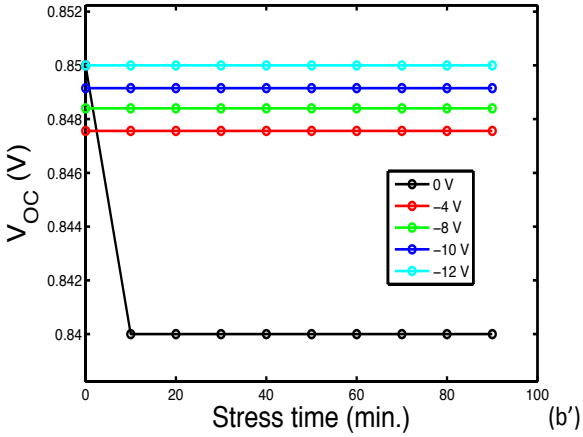
V_OC (V)
Stress time (min.)
0 V
−4 V
−8 V
−10 V
−12 V

(b')

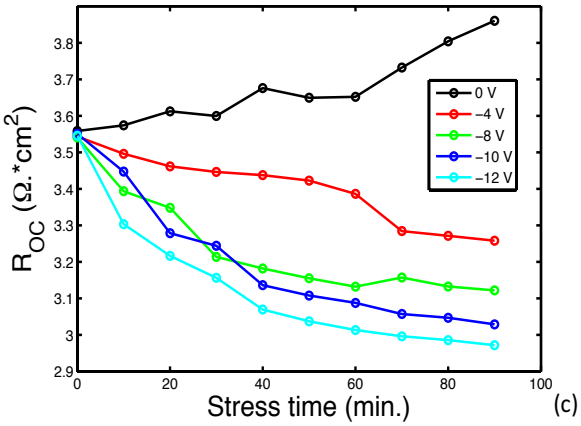
R_OC (Ω.*cm^2)
Stress time (min.)
0 V
−4 V
−8 V
−10 V
−12 V

(c)

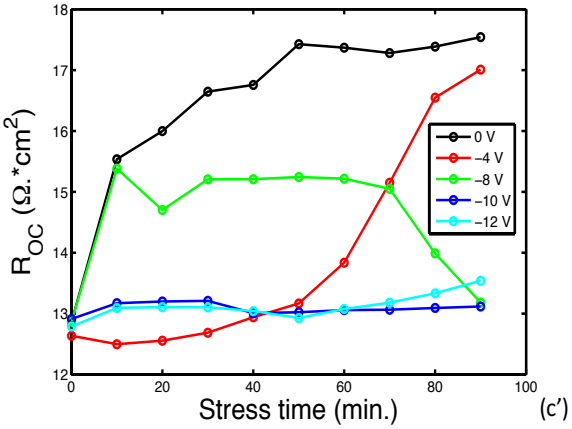
R_OC (Ω.*cm^2)
Stress time (min.)
0 V
−4 V
−8 V
−10 V
−12 V

(c')

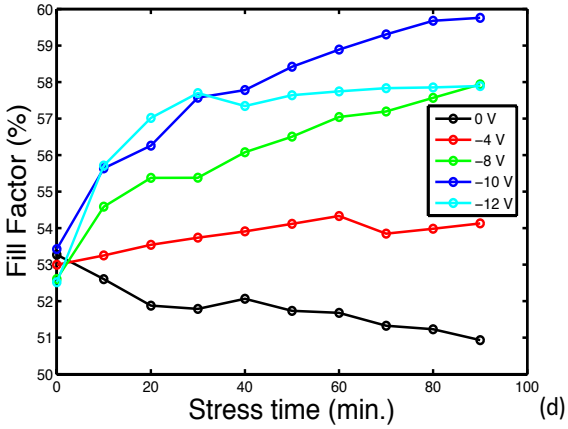
Fill Factor (%)
Stress time (min.)
0 V
−4 V
−8 V
−10 V
−12 V

(d)

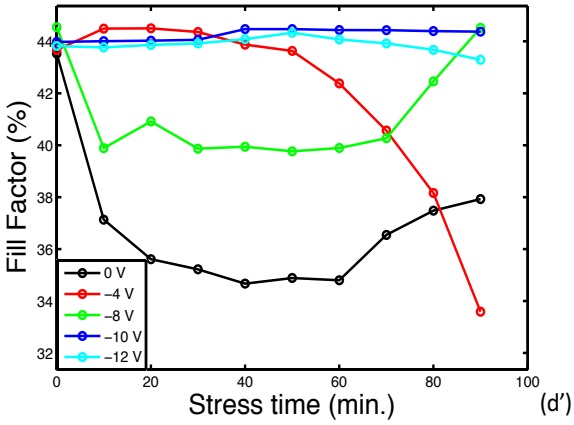
Fill Factor (%)
Stress time (min.)
0 V
−4 V
−8 V
−10 V
−12 V

(d')

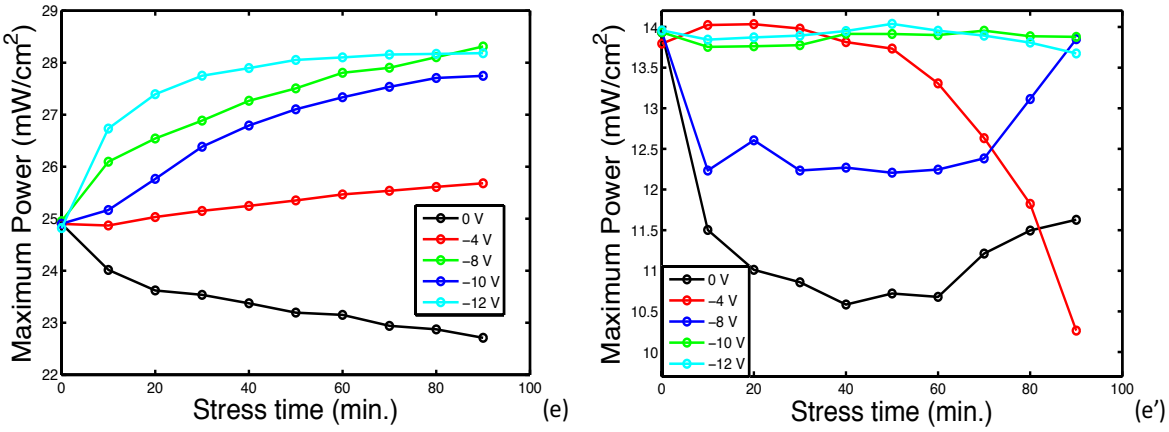

Fig. 3.7. Data trend analysis for (x) solar cells with FTO as bottom contact layer and (x') solar cells having Mo as same contact layer as a function of stress time for increasing reverse bias voltages under a light exposure of 3 equivalent suns and a temperature of 40 °C.

From the comparison of Figs. 3.7 it is evident that the samples with molybdenum have no advantage from the reverse bias stress, contrarily to the samples with FTO. As above, series resistance and fill factor improve under reverse bias stress in the samples with FTO, while the opposite (a worsening) is seen in the case of samples with the Mo contact. Overall, in the case of FTO the power conversion efficiency improves under reverse bias stress, while it gets worse in the samples with Mo.

The result of Figs. 3.7 can be well explained by the above-described hypothesis, i.e., that the observed effect is due to the motion of ions in and out from the FTO to the p-type a-Si:H layer (or from the SiO_2 to the p-type a-Si: H layer in the case of Fig. 3.5) and vice-versa [46]. Such motion is not possible in the case of the Mo substrate, since Mo is a very dense metal with a large melting point, in which atomic diffusion is inhibited. In fact, Mo is frequently used as diffusion barrier. So, most likely the motion of light ions in and out from the p-type a-Si:H layer is not possible with the Mo contact, and this explains why the reverse bias stress does not produce any positive result in the Mo case.

We mainly find an improvement of V_{OC} and R_{OC}. The R_{OC} improvement, is most likely due to a reduction of electrical resistance of the p-type a-Si:H film, being the other layers responsible for the R_{OC} value, i.e., the TCOs layers and the n-type a-Si:H film, with a much higher electrical conductance compared to the p-type a-Si:H layer which then likely dominates the series resistance.

The improvement of p-type a-Si:H layer conductance hypothesized by the R_{OC} improvement is actually confirmed by completely independent experimental observations on the behaviour of the sheet resistance of single layers of p-type and n-type a-Si:H films grown on SiO_2 substrates subjected to electrical stresses.

In fact, the reverse bias stress pulses have a profound effect (decrease) on the sheet resistance in the p-type films, where, moreover, clear reversibility is found since forward bias stresses recover the initial values. This suggests that the effect on the p-type layer resistivity is related to the motion of charged defects, and we demonstrate that such resistivity change/defect motion is reversible. On the contrary, in the case of n-type layers almost no change is found after the electrical stress pulses. The results on single doped a-Si:H layers on SiO_2 are consistent with the results on the R_{OC} improvement seen in the solar cells. We cannot draw any definite conclusion about the nature of such charged defect species, but we speculate it may be related to alkaline metal or hydrogen ions, which are well known to be able to rapidly diffuse and migrate under electric field application in SiO_2, and most likely also in FTO and in glass.

3.5. Reversibility of the Solar Cell Parameters

As observed in the case of p single substrates, where the sheet resistance goes up and down following the sign of the applied voltage pulse, also in the case of the complete a-Si:H solar cells it is observed reversible changes in the solar cell power conversion efficiency finding monotonic trends in response to forward and reverse bias stress. The effect of reversibility is indeed further analyzed in the data of Figs. 3.8, where the complete solar cell reversibility property is illustrated. In this analysis the reversible monotonic trends of the main solar cell parameters in response to a reverse and forward applied bias stress (-12 V and + 0.6 V respectively) are shown. Efficiency under forward bias in the Maximum Power Point (MPP) condition, improved through sequences of reverse bias stresses, is monitored as a function of time. It is here evident a strong overall improvement of efficiency. Further advantage is obtained by optimizing the stress sequence. These experiments were conducted at room temperature, under a light exposure of 3 suns and with a single stress duration of 4000 s.

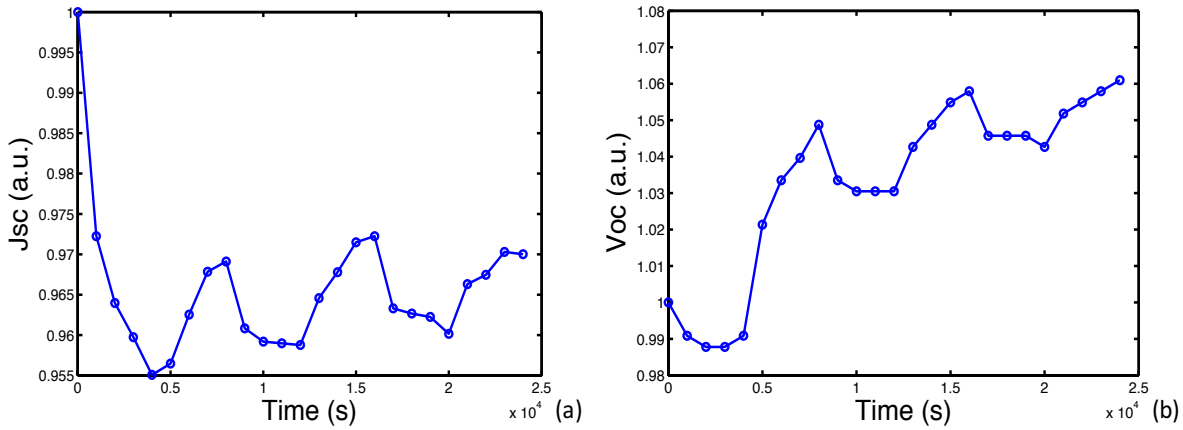

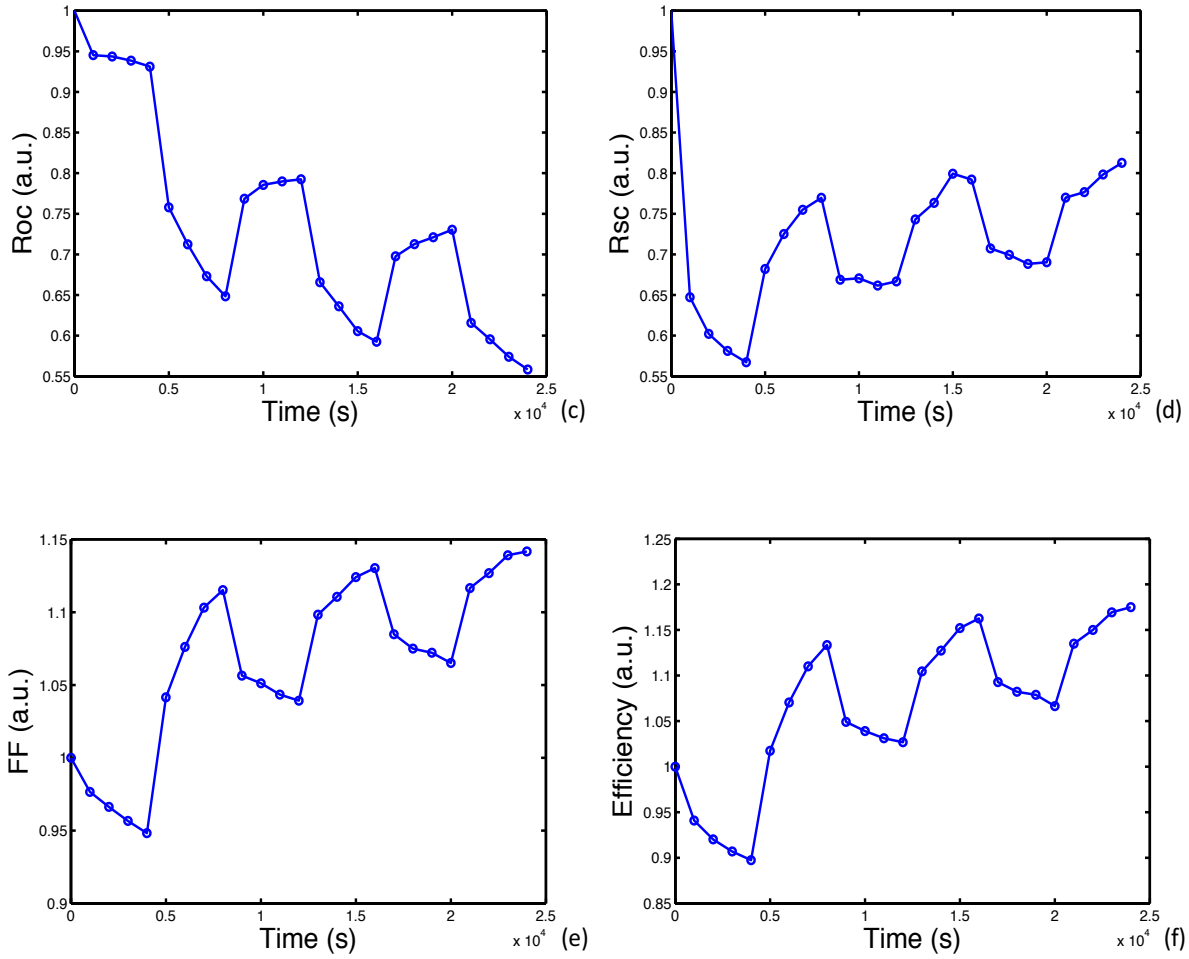

Fig. 3.8. Normalized (a) J_{SC}, (b) V_{OC}, (c) R_{OC}, and (d) R_{SC} data trend analysis as a function of stress time in response to alternating voltage bias (-12 V and +0.6 V) applied for 4000 s each under a light exposure of 1 equivalent sun.

About the practical use of reverse bias in solar cells application, the efficiency improvement given by the electric field needs to be compared with the external energy necessary to be applied to get efficiency improvement. Although the behavior in a complete PV system may be quite different compared to the solar cells here descripted and, of course, a careful analysis of the overall energy balance needs to be initially performed in any case, the following figure shows an example of how these solar cells performances have been experimentally enhanced.

Fig. 3.9 reports an experiment where two identical solar cells exposed to the same light source at 1 equivalent sun were used. The first cell has been connected to a load forcing its working point operate around its maximum power point (+0.6 V) for a time of 400 minutes. The second cell (having identical initial conditions) was instead initially stressed (control phase in the graph) with -12 V (for a time of 100 min.) and then forced, just after the previous stress, with +0.6 V (post-stress ageing phase in the graph). After that, to verify the capacity of the second cell to maintain the gained efficiency during the

stress phase, it was left in open circuit / dark conditions for 1 day. As clearly visible in the graph below (1 day after ageing), the degradation trend restart exactly from the previous day efficient value so, despite both pre-stress and post-stress ageing curves show an identical fall trend, the applied reverse bias stress has allowed a significant efficiency gain between them.

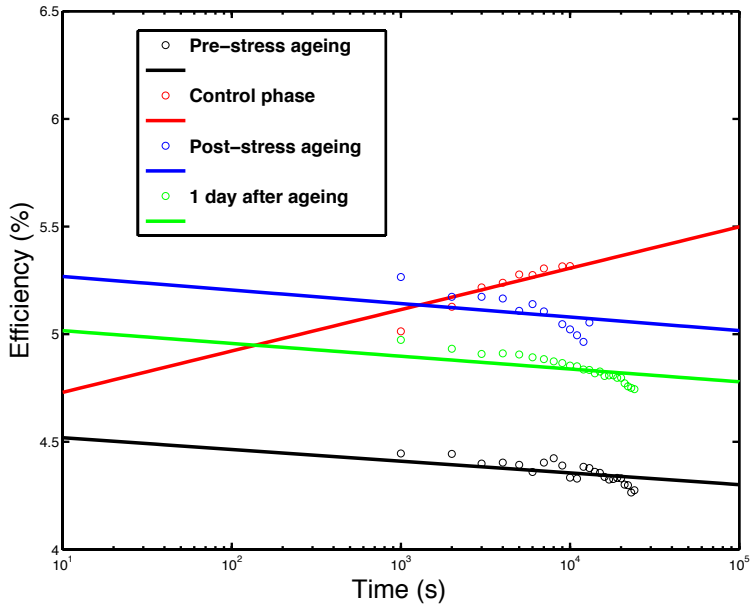

Fig. 3.9. Data trend analysis as a function of stress time showing a practical use of reverse bias in solar cells application.

As already pointed out, the behaviour in large area devices such as complete PV modules may be quite different compared to small area solar cells, as studied in this work. So, we believe that understanding the practical viability of such approach requires studies with complete PV modules in solar fields, and a careful analysis of the overall energy balance.

3.6. Dark Analysis

In addition to the R_{OC} improvement, in Figs. 3.8 we also observe a V_{OC} gain. Such improvement indicates an improvement (decrease) of the forward bias current in dark, attributed to an improvement in carrier lifetime. To further investigate on this, it was decided to analyze the solar cell characteristics in dark conditions, by comparing the case of forward and reverse bias stress. Figs. 3.10 and 3.11 show the results of the application of DC constant voltage stresses at room temperature to the PV cells either in reverse bias (−4 V, see Figs. 3.10) or in forward bias (+4 V, Fig. 3.11). Light intensity during the DC stress was in all cases equal to about 0.25 suns. In particular, Figs. 3.10 (a) and (b) show that the

application of the reverse bias stress is accompanied by an improvement (decrease) of the ideality factor (n) and of the pre-exponential J_0 of the forward bias I-V characteristics, fitted by the well known expression $J = J_0*\exp(qV/nkT)$. The decrease of n and J_0 indicates an improvement of the carrier lifetime, which explains the η improvement.

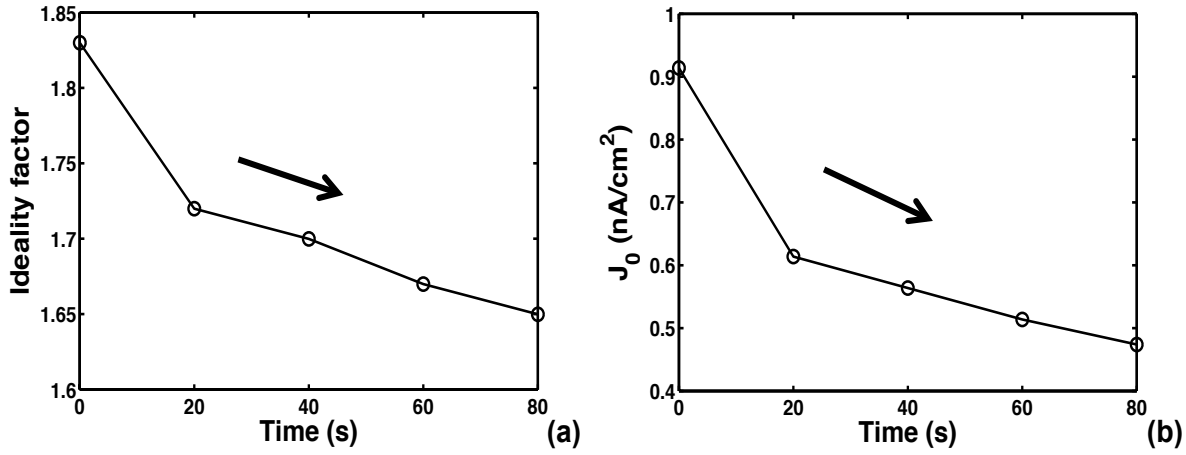

Fig. 3.10. Improvement of a-Si:H single junction solar cell I-V characteristics under reverse bias stresses at - 4 V with a light exposure at 0.25 equivalent suns: (a) ideality factor (n) vs. stress time; (b) J_0 parameter vs. stress time (n and J_0 measured in dark).

On the contrary, under forward bias stress with illumination, i.e., in a condition similar to the solar cell operation in the maximum power point (MPP), J_0 and n increase (Figs. 3.11 (a) and (b)). This indicates a worsening of carrier lifetime, due to increased density of defects promoting recombination.

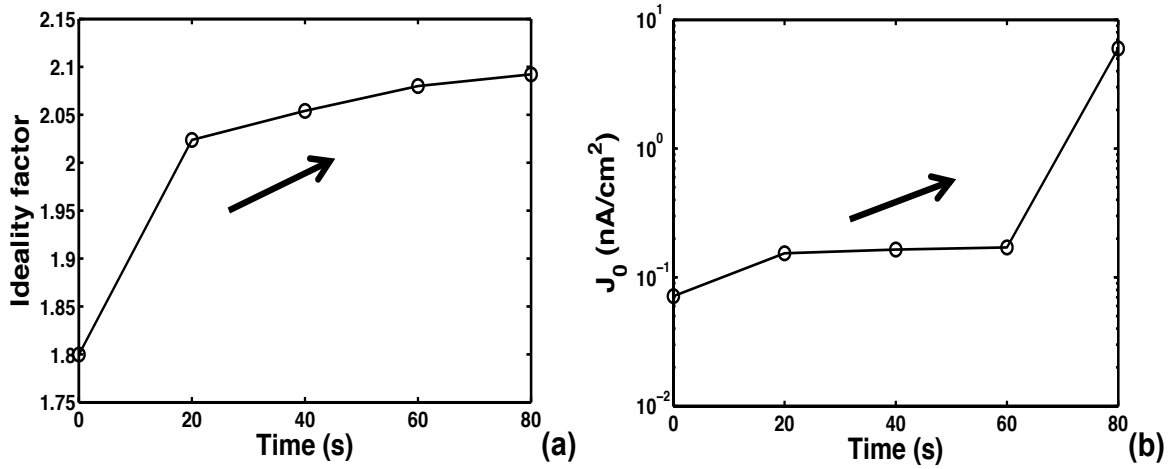

Fig. 3.11. Worsening of a-Si:H single junction solar cell I-V characteristics under forward bias stresses at + 4 V with a light exposure at 0.25 equivalent suns: (a) ideality factor (n) vs. stress time; (b) J_0 parameter vs. stress time (n and J_0 measured in dark).

3.7. Effect of Field and Pump Light Wavelength during DC Stress

As shown by the data of Fig. 3.3, the a-Si:H single junction solar cell improvement under reverse bias stress is proportional to the light intensity. We have therefore determined for this type of solar cell the range of wavelengths where the photons are effective to improve the lifetime and cell efficiency. For this purpose we have pumped the solar cells under reverse bias stress with monochromatic light at different wavelengths, all with about 1 nm Full Width Half Maximum (FWHM), and we have monitored the resulting external quantum efficiency (EQE) evolution.

Fig. 3.12 reports the percentage gain of EQE after reverse bias stress (i.e., EQE after stress minus initial EQE divided by initial EQE). The various curves refer to different pump wavelengths during the stress, ranging from 400 nm to 900 nm. All curves are normalized to the same flux and dose of pump photons.

From the data analysis it is evident that the EQE improvement is present only when the pump wavelength is in the range from 700 to 800 nm. Outside this interval, no appreciable improvement or change of EQE is observed.

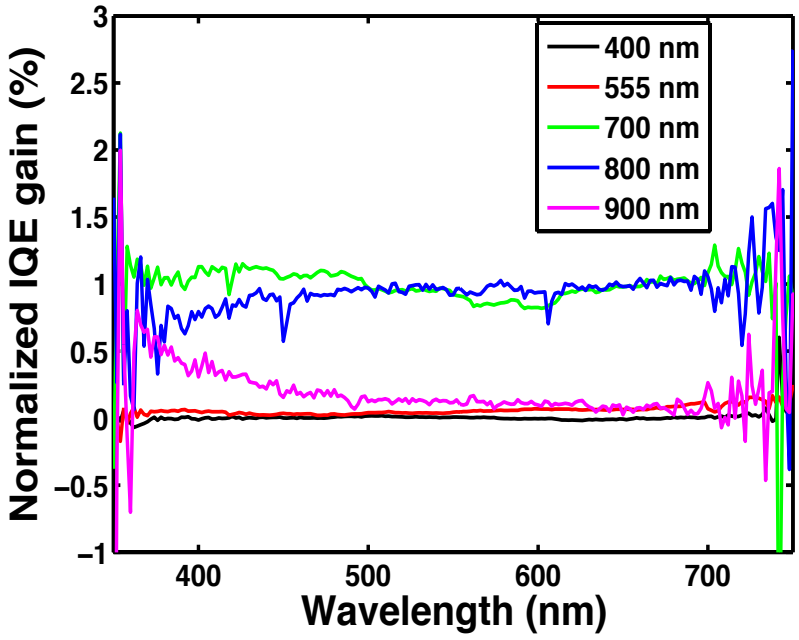

Fig. 3.12. Normalized IQE gain for five different radiation wavelengths: 400 nm, 555 nm, 700 nm, 800 nm and 900 nm.

Fig. 3.12 data therefore indicate that the mechanism of lifetime improvement is linked to a process promoted by photons in the 700-800 nm range, i.e., with energy of 1.6-1.7 eV, that is, close to the a-Si:H band gap.

About the dependence on wavelength of EQE in response to a reverse and a forward bias stresses (-10 V and +10 V respectively), with the same dose of pump photons at fixed wavelength (700 nm), Fig. 3.13 confirms that forward and reverse bias stresses have the opposite effect, i.e., they produce improvement for reverse bias and worsening in forward bias, and that the effect on EQE is "flat", that is, approximately constant in the whole wavelength range.

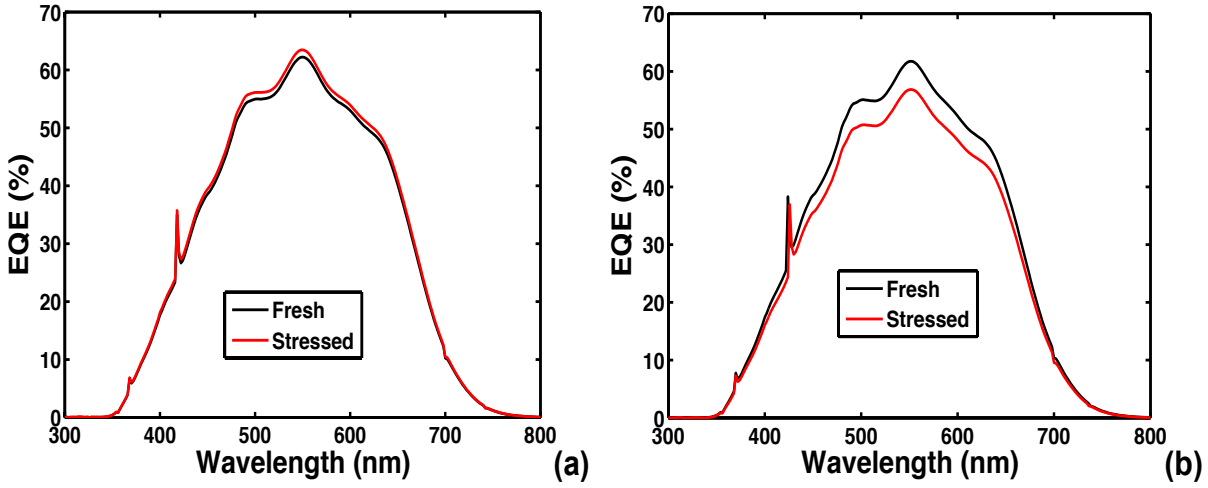

Fig. 3.13. Data trends analyses showing the EQE spectrums of both fresh and stressed solar cells. The stress, one minute long, was conducted under a radiation wavelength of 700 nm and under (a) a reverse bias of -10 V; (b) a forward bias of +10 V.

Chapter 4

a-Si:H Tandem Solar Cell Performance Improvement

In the previous section it was investigated the possible causes of improvement for single junction a-Si:H solar cells. As discussed, a possible cause of the described instability/improvement is the motion of ions in and out from the transparent conductive oxide (TCO) in contact to the p-type a-Si:H layer, as indicated by the comparison of the behavior of PV cells deposited on various types of substrate. In this chapter, the experimental part is addressed to further analyze this phenomenology: are here reported the results of studies on the application of DC reverse bias stresses in the case of tandem Si solar cells, and the results are compared to the case of single junction amorphous Si cells.

The tandem amorphous/microcrystalline analysis is, in this chapter, splitted in two different sections: a first part is oriented to verify the important contribution given by the electric field on single cells in indoor conditions, i.e. assisted by the solar simulator illumination; the second part of the study, insted, is intended to verify the important results observed on the single cells under real condition of illumination (outdoor analysis) and for commercial tandem amorphous/microcrystalline Silicon PV minimodules, produced and made available to us by *3SUN*.

4.1. Single Cells Analysis: Experimental Results

4.1.1. Experimental Details and Conditions

The cells used in this work were tandem amorphous/microcrystalline Si solar cells fabricated by 3SUN, deposited on SnO_2:F transparent conductive oxide of AGC glass substrates by plasma enhanced chemical vapor deposition.

As shown in Fig. 4.1, the tandem cell device structure is the following: glass/SnO_2:F/p a-Si:H/intrinsic a-Si:H/n_a-Si:H/p_microcrystalline-Si/intrinsic_microcrystalline-Si/n-microcrystalline-Si/ZnO/Ag.

The thicknesses of the intrinsic layers in the amorphous and in the microcrystalline Si layers were about 200 nm and about 1μm, respectively, while the doped n^+ and p^+ a-Si:H and microcrystalline Si films were a few tens on nanometers. The final geometries (circular with diameters varying from 0.01 to 0.64 cm) were defined by photolithography and selective etching. Front TCO is engineered to improve light transmittance and light scattering while the back TCO layer (ZnO) has the function to reduce series resistance, improve adhesion, and to enhance the reflectivity of the back reflector.

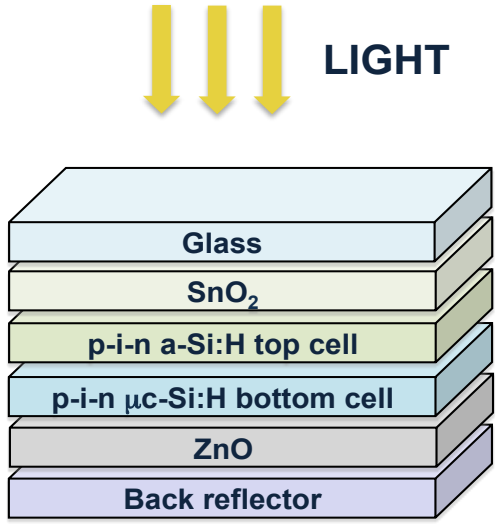

Fig. 4.1. Schematic structures showing the layers sequence.

All the I-V measurements to test the solar cells were performed with the voltage varying in the -0.1 to +1.5 V range by using a Keithley 2602A SMU connected via a General Purpose Interface Bus (GPIB) to a PC for computer control via an IEEE-488 GPIB connected to a personal computer for control. To understand how DC electric fields affect the recovery/improvement kinetics of the solar cells, the cells were stressed by using a reverse bias voltage varying in the 0 to -12 V range. Stress durations varied exponentially in the 10-10 000 s range. Stresses and the I-V measurements under illumination were performed in superstrate configuration.

Solar cell illumination was achieved with an AM1.5G spectrum by using a 92191-1000 Newport solar simulator assisted, in some cases, by a system with mirrors and Fresnel lenses to change the light intensity by focusing or defocusing the solar simulator light beam. The solar cells temperature was regulated by using a cooling system consisting of three fans properly oriented toward the cells to avoid cell overheating due to the exposure to the light of the solar simulator. The solar cell temperature was monitored through a negative temperature coefficient thermistor sensor placed in contact with the cell.

To understand the effect of reverse bias stress on the cells, we have analyzed all the major solar cell parameters/figures of merit, that are, series resistance (R_{OC}), short circuit current density (J_{SC}), open circuit voltage (V_{OC}), fill factor (FF), and power conversion efficiency (η) as a function of the stress time. For each stress sequence, an initially fresh solar cell was used, and its evolution was monitored by temporarily stopping the stress and recording the I-V characteristics.

4.1.2. Reversing LID: Bias Effect

Also for this type of cells, it was studied how the level of reverse bias during stress affects the solar cell performance. The solar cell parameters as a function of the stress time for different levels of reverse bias at room temperature and at 1 sun illumination level are reported in Fig. 4.2.

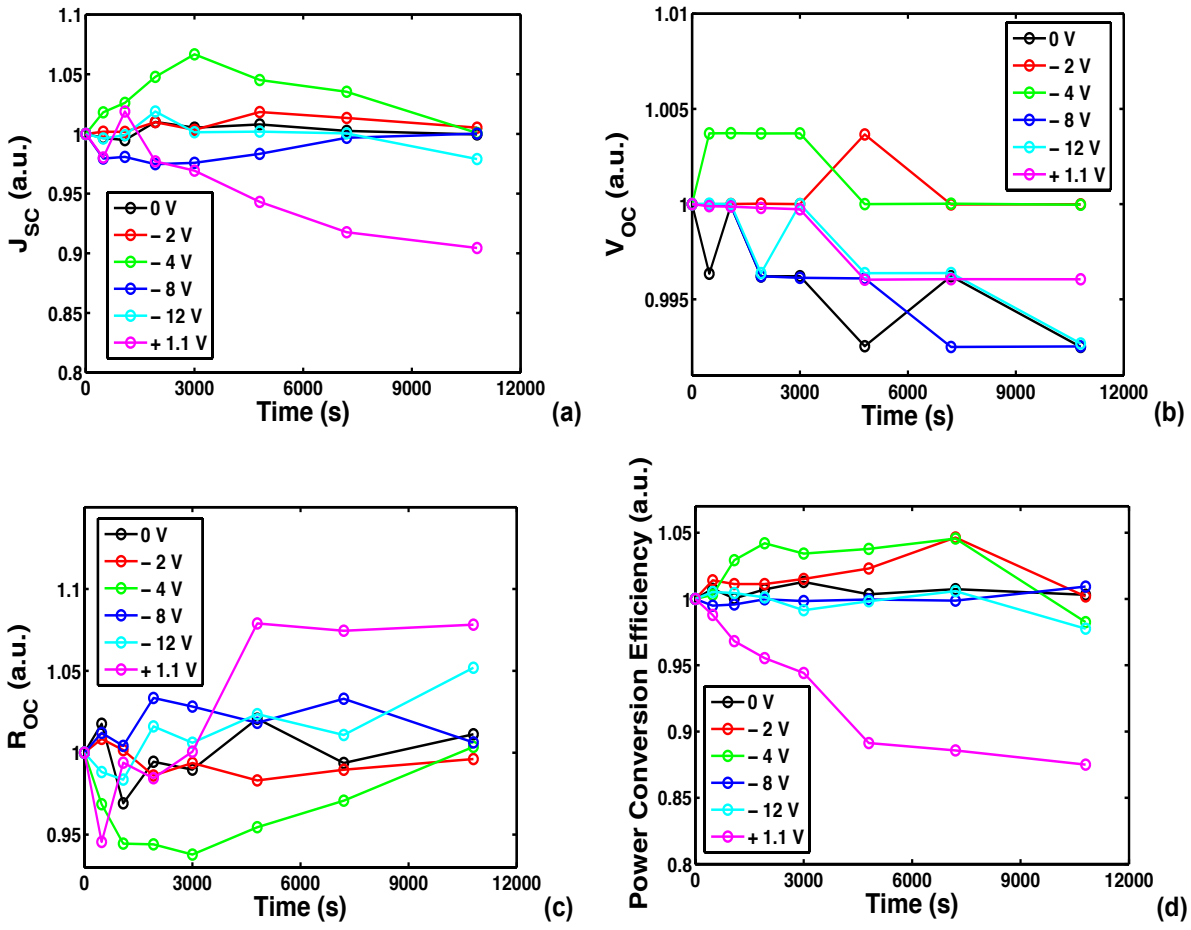

Fig. 4.2. Normalized data trend analysis for (a) J_{SC}, (b) V_{OC}, (c) R_{OC}, and (d) Efficiency as a function of stress time for increasing reverse bias voltages under a light exposure of 1 equivalent sun.

From Fig. 4.2, it is evident that by proper reverse bias stress voltage levels (the best behavior is observed at -4 V), the solar cell characteristics shift toward higher power conversion efficiencies. On the contrary, under MPP or in short circuit conditions the solar cell characteristics worsen under the Staebler–Wronski wearout mechanism. So, similarly to the case of single junction amorphous Si PV cells, also in the case of tandem amorphous/microcrystalline Si cells, it was observed that the reverse bias stress rather than simply slowing down the wearout rate under light soaking, for suitable applied voltage conditions improves the solar cell characteristics.

The results of Fig. 4.2, demonstrating that the electric field plays a strategic role, confirm the idea that this instability may be linked to the motion of some charged atomic / molecular species. In this case, as seen, the level of the applied reverse bias during stress has a strong effect on the kinetics of the solar cell I-V characteristics evolution.

It is extremely important to notice that this time much lower stress voltage is required, though the presence of illumination during the stress is crucial, as in the case of single junction a-Si:H cells. As clearly visible in Fig. 4.2, in the case of tandem amorphous/microcrystalline Si cell, the reverse bias voltage at which the best improvement results are found is -4 V, which corresponds to much lower electric field intensities. Fig. 4.3 reports, at room temperature and under a light exposure of 1 equivalent sun, the I-V sequence observed applying a reverse bias of -4 V (the best voltage level in terms of improvement). Here is clearly evident the improving trend, which shifts toward higher power conversion efficiencies as the stress time increases.

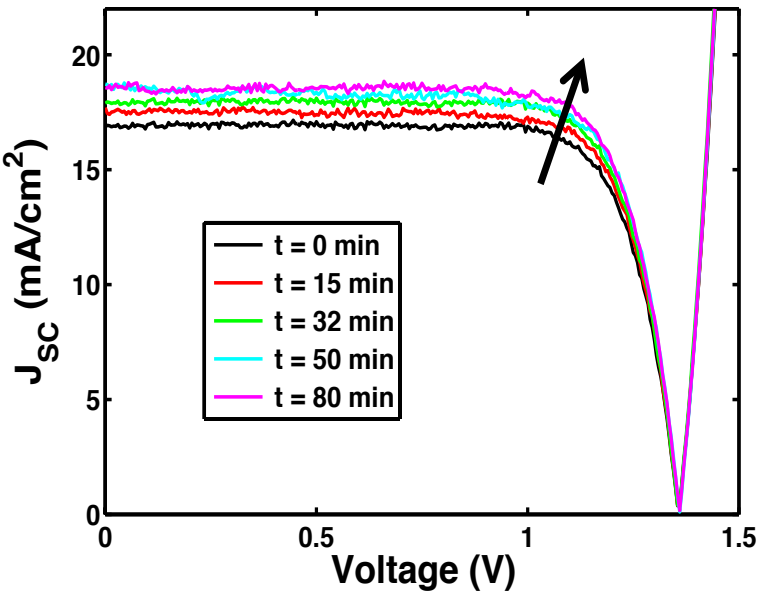

Fig. 4.3. Improvement of the I-V curve of a tandem amorphous/microcrystalline Si solar cell observed by applying a reverse bias stress of -4 V under a light exposure of 1 equivalent sun.

4.1.3. Reversing LID: Combined Bias - Light Effect

To further investigate the causes of such phenomenon, also in this case the role played by the illumination intensity during the reverse bias stress application was analyzed. Fig. 4.4 reports some data concerning the role played by the illumination intensity during the reverse bias stress. The figure reports the behavior of the solar cell main parameters under reverse bias stresses at -4 V versus stress time subjected to various illumination conditions, with the PV cell maintained at room temperature. It is evident that by increasing the light intensity, the cell parameters improvement rates increase very significantly.

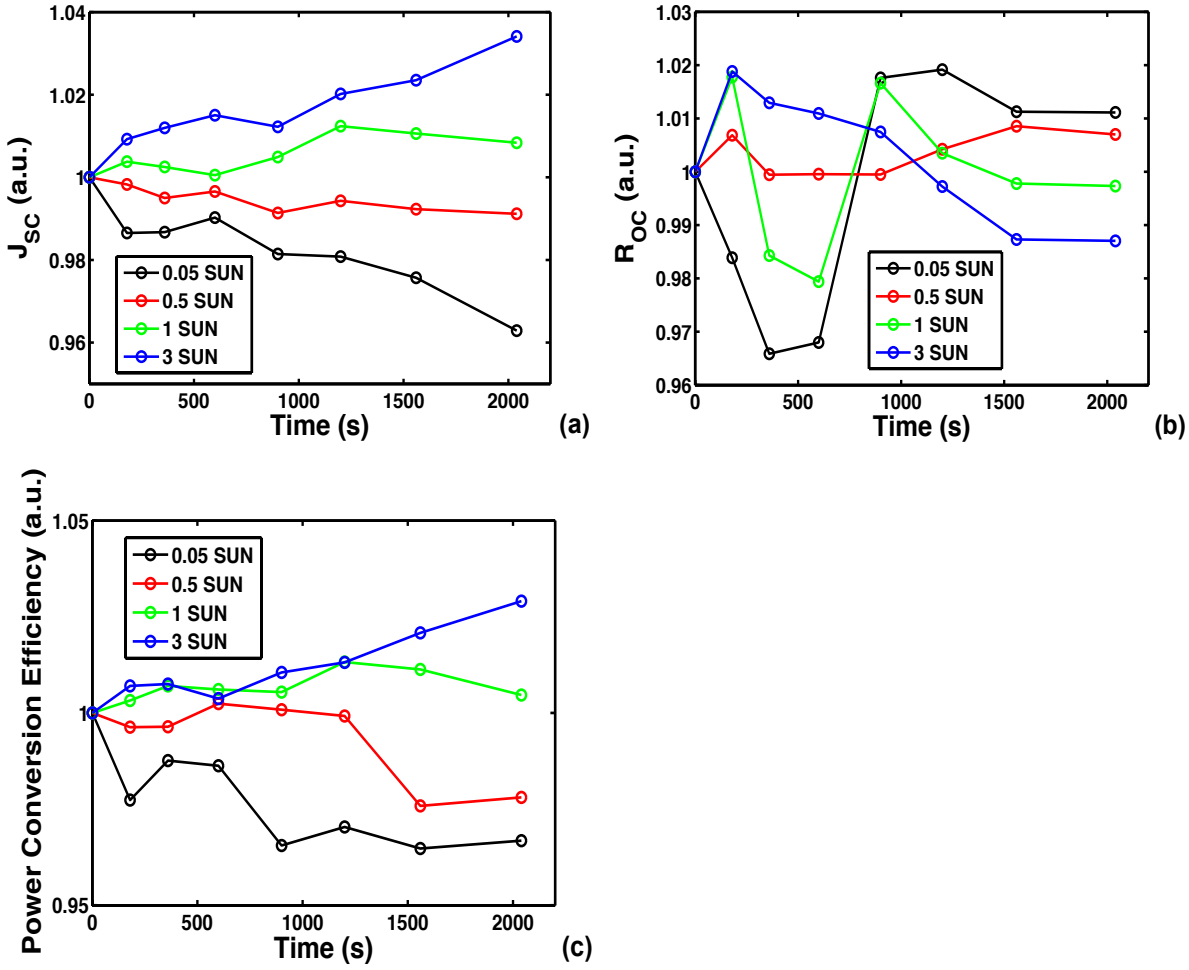

Fig. 4.4. Normalized (a) J_{SC}, (b) R_{OC}, and (c) efficiency as a function of stress time for various light intensities during stress at room temperature and fixed reverse bias of - 4 V.

These results are qualitatively similar with previous findings obtained on single junction a-Si:H cells which show that the rate of recovery of light-induced degradation depends not only on the reverse bias level but also on the light conditions. Also, in this case of tandem amorphous/ microcrystalline Si PV cells, the major effect induced by the reverse bias stress under illumination is an improvement of the short circuit current, of cell series resistance and therefore, of the power conversion efficiency.

Although, as already pointed out in the previous chapters, the behavior in a complete PV system may be quite different compared to our solar cells and the efficiency improvement given by the electric field needs to be compared in any case with the external energy necessary to be applied for the scope, the following figure shows an example of how we have experimentally enhanced our solar cells performances. Once examinated, indeed, the key factors responsable for the recovery-improvement kinetics, Fig. 4.5 reports an experiment where the cell efficiency η of a tandem micromorph solar cell was recovered after an initial stress in operative conditions.

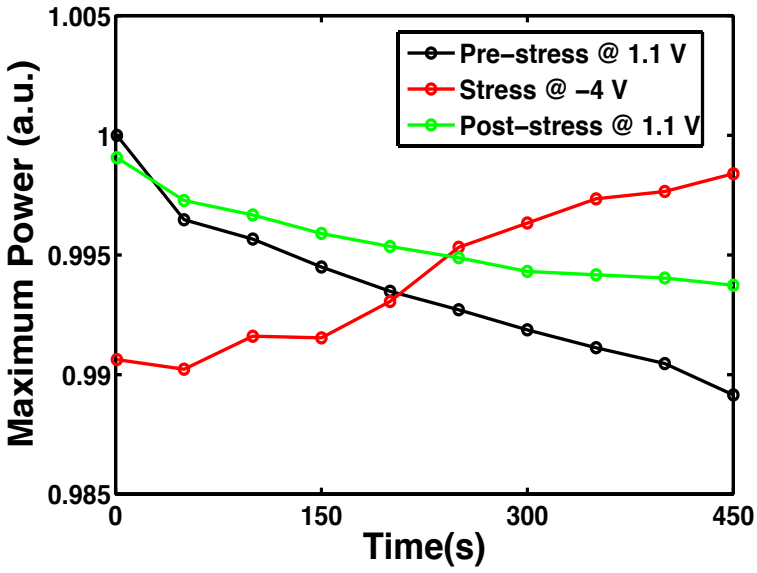

Fig. 4.5. Normalized data trend analysis as a function of stress time showing a practical use of reverse bias in tandem solar cells application.

In this experiment the cell has been initially connected to a load forcing its working point operate around its maximum power point MPP (+1.1 V) for a time of 450 s (pre-stress ageing phase in the graph) and under a light source of 1 equivalent sun. The cell was so stressed using a reverse bias of -4V (for a same time of 450 s) and then forced, just after the recovery stress, to operate in MPP condition. As visible from Fig. 4.5, we note that using the reverse bias stress not only it is possible to completely recover the cell efficiency η, but also the kinetics of the following LID under MPP conditions appears slower.

4.1.4. Dark Analysis

Further information is provided by analysis of the solar cell I-V characteristics in dark conditions. In particular, also in the case of tandem solar cell, we have analyzed the evolution of such characteristics under DC constant voltage stresses under illumination, by comparing the case of forward and reverse bias stress.

Figures 4.6 and 4.7 show the results of the application of DC constant voltage stresses at room temperature to the PV cells either in forward bias (+4V, see Fig. 4.6) or in reverse bias (-4V, Fig. 4.7). Light intensity during the DC stress was in all cases equal to about 0.25 suns.

Figures 4.6(a) and 4.7(a) report the evolution of the I-V characteristics under illumination as the DC stress progresses, while Figs. 4.6(b), 4.6(c), 4.7(b), and 4.7(c) show the evolution of the parameters describing the I-V characteristics in dark.

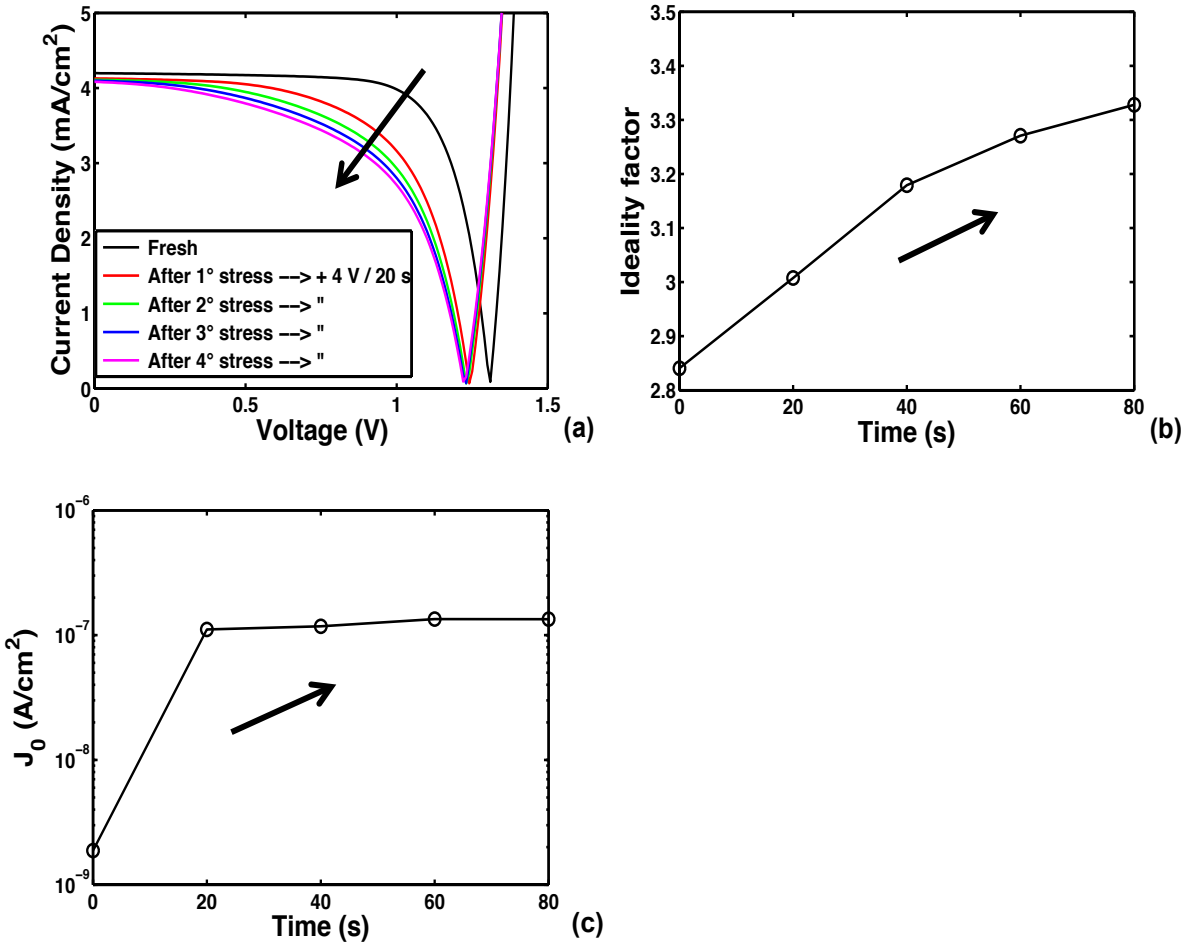

Fig. 4.6. Worsening of solar cell I-V characteristics under forward bias stresses at +4 V with a light exposure at 0.25 equivalent suns: (a) I-V curves; (b) ideality factor vs stress time; (c) J_0 parameter vs stress time (n and J_0 measured in dark).

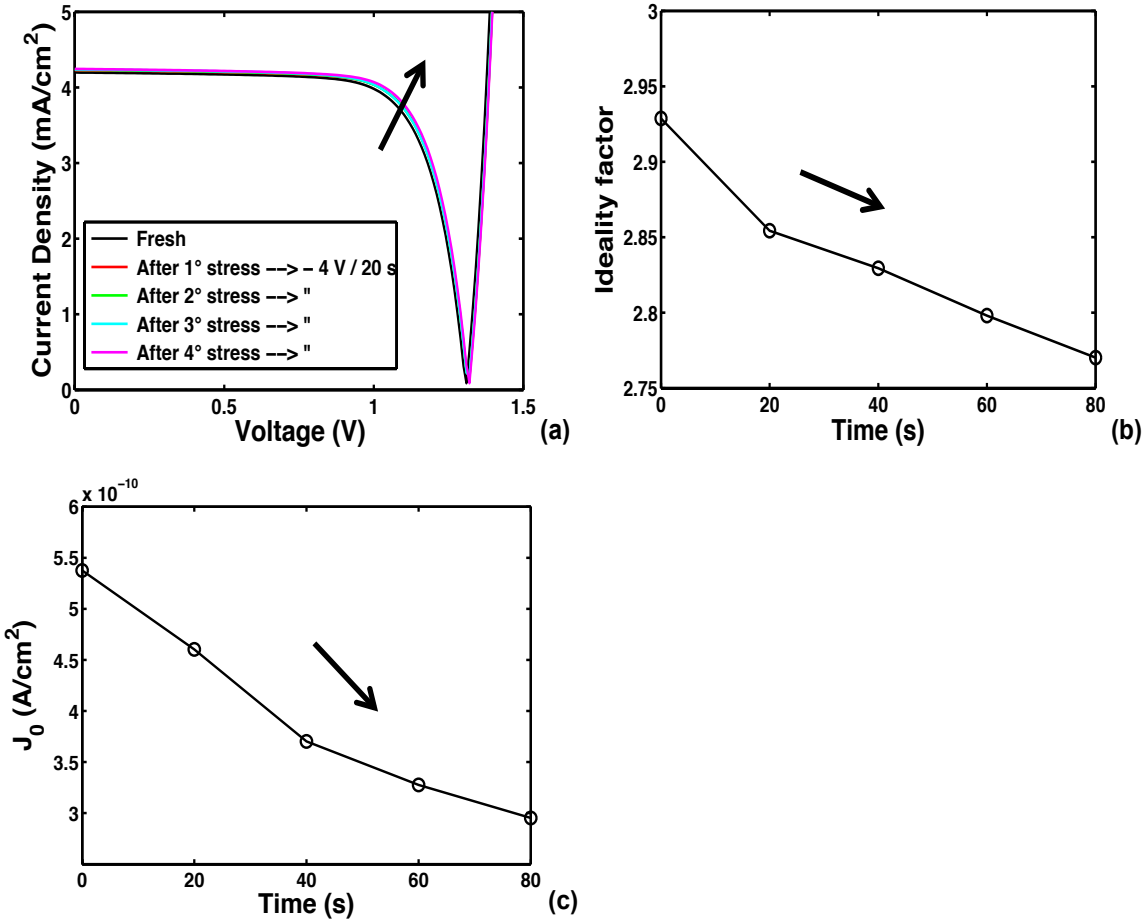

Fig. 4.7. Improvement of solar cell I–V characteristics under reverse bias stresses at -4 V with a light exposure at 0.25 equivalent suns: (a) I-V curves; (b) ideality factor vs stress time; (c) J_0 parameter vs stress time (n and J_0 measured in dark).

For the latter, we assume that the I-V curve is described by the equation $J = J_0 \times \exp(qV/nkT)$, where J_0 is a pre-exponential factor, n the ideality factor, k the Boltzmann constant, and T the absolute temperature. Figures. 4.6(b) and 4.7(b), and Figs. 4.6(c) and 4.7(c) report, respectively, the evolution of the ideality factor n, and of the pre-exponential term J_0. Note that n is larger than 2 since the forward bias I-V curve is the series of two p-i-n junctions, i.e., the amorphous and the microcrystalline Si cell. The value of the ideality factor n, approximately equal to 3, is indicative that either the amorphous, or the microcrystalline p-i-n junction, or both the junctions present relevant recombination effects, since for a single junction an ideality factor larger than 1 and up to 2 is indicative of strong recombination. In this case, are present two junctions in series with an ideality factor that is the sum of the two-ideality factors of the two junctions. This results in experimentally ≈ 3, in the presence of relevant recombination in one or both the junctions. An improvement (decrease) of n and J_0 indicates a reduction of the recombination rate, i.e., an increase in the carrier lifetime.

The data of Figs. 4.6 put in evidence that the application of a forward bias stress causes an evident worsening of the I-V characteristics, both under illumination and in dark. All cell parameters under illumination, J_{SC}, V_{OC}, R_{OC}, and η worsen, and this is accompanied by a worsening of the parameters describing the I-V characteristics in dark, n and J_0, which both increase. On the contrary, under reverse bias stress (Figs. 4.7), an improvement of all the PV cell parameters, both under illumination and in dark, is revealed.

The improvement of n and J_0 indicates that the electron-hole recombination rate is decreasing under the effect of the reverse bias stress, and this is reflected by the improvement of the solar cell parameters, J_{SC}, V_{OC}, R_{OC}, and η.

4.1.5. Effect of Field and Pump Light Wavelength during DC Stress

Once observed the improvement of the overall tandem cell power conversion efficiency, an important question is to understand which of the two cells in series composing the tandem structure, i.e., the amorphous Si and the microcrystalline Si PV cell, is the cause. Figure 4.8 reports the ratio of two external quantum efficiency (EQE) spectra, i.e., the spectrum after the reverse bias stress at -4V for 5 min under illumination with a 700 nm light, divided by the initial spectrum.

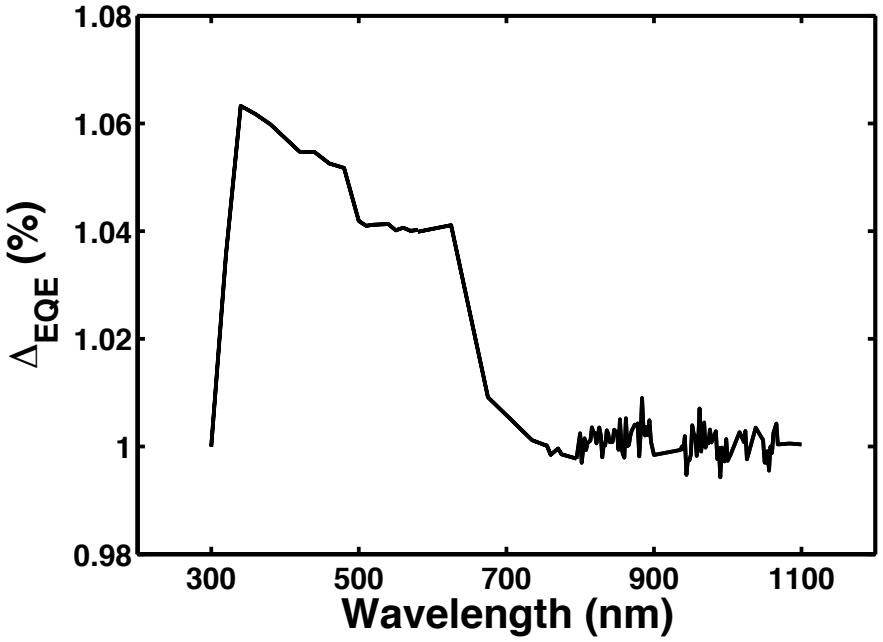

Fig. 4.8. Ratio of an EQE spectrum after a reverse bias stress at -4 V for 5 min under illumination with a 700 nm light divided by the initial EQE spectrum.

It is evident that the EQE after the reverse bias stress increases in the blue portion of the spectrum. This is the part of spectrum transformed into electrical power by the top amorphous Si cell. The red portion of EQE, i.e., the part of solar spectrum managed by the microcrystalline Si cell does not change. Therefore, we can conclude that the reverse bias stress is improving the performance only of the amorphous Si cell, not of the microcrystalline Si cell. The improvement of the a-Si:H cell provides an overall improvement of the tandem cell.

4.2. Mini-Modules Analysis: Experimental Results

Once performed the analysis on single cell, to verify the important contribution given by the electric field on the recovery/improvement mechanism, a similar DC electric stress was applied to commercial micromorph modules. In fact, while in the first part of the study the research on tandem was performed on single cells having as final geometries circular shape with diameters varying from 0.01 to 0.64 cm, in this second part of the analysis it was studied how the level of reverse bias during stress affects, under real condition of illumination (outdoor analysis), the solar cell performance of commercial tandem amorphous/microcrystalline Silicon PV minimodules, produced by 3SUN.

4.2.1. Device and Stress Procedure Description

In this study all the several tests were performed outdoor in Maximum Power Point (MPP) condition (according to a repeating sequence morning – afternoon, between June and September) on groups of four stabilized (i.e. subjected to 1000 h light soaking, before our stress tests) tandem amorphous/microcrystalline Silicon PV minimodules, each consisting of 3 solar cells electrically in series and having the basic structure shown in fig. 4.1.

The tandem amorphous/microcrystalline Silicon PV minimodules have been installed on an appropriate support structure (inclined 30° on the horizontal plane and facing south, at a latitude of about 37,41°N). Fig. 4.9 shows the Device Under Tests (DUTs) and the c-Si reference solar cell which we used to take over the irradiance level during the tests.

To set the proper stress conditions and measure the electrical output characteristics of the DUTs and of the reference (Ref) cell a Keithley 4200 instrument was used. In each test, the DUTs were subjected to a set number of consecutive cycles; in each one, all the DUTs worked at constant voltage in their maximum power point (for a duration of 600 s) and at the beginning of each cycle, the output I-V (i.e. current vs voltage) electrical characteristics of the DUTs and of the Ref. cell were measured.

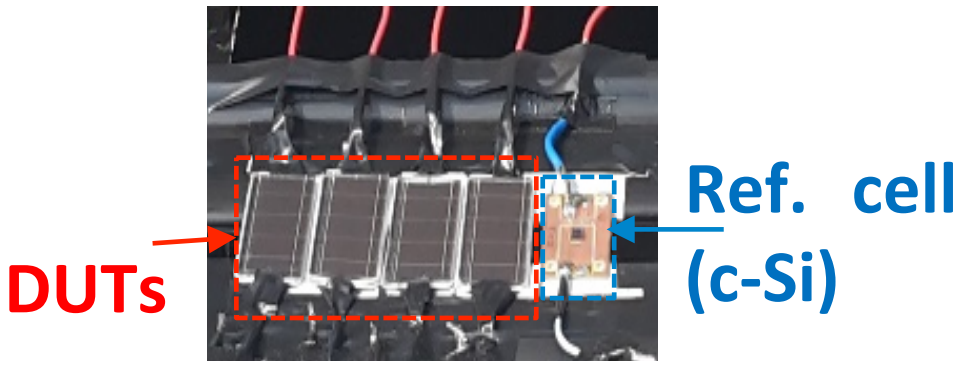

Fig. 4.9. Photograph of the tested PV devices (DUTs) and the Ref. cell (c-Si), on the support structure.

In the table 4.1 are shown the main characteristics of one of the micromorph minimodules (DUT) used for the outdoor experiments.

Micromorph PV Minimodules Main Characteristics	
ACTIVE AREA (cm x cm)	**3,2 x 2,1**
J_{SC} (A / cm^2)	**9,5 x 10^{-3}**
I_{SC} (A)	**21,28 x 10^{-3}**
V_{OC} (V)	**4,101**
I_{MPP} (A)	**20,53 x 10^{-3}**
V_{MPP} (V)	**3,27**
P_{MAX} (W)	**67,13 x 10^{-3}**
Efficiency (%)	**10,49**
FF (%)	**77**
R_{OC} (Ω)	**20**

Table 4.1. Tandem amorphous/microcrystalline Silicon PV minimodule (DUT) main characteristics

4.2.2. Experimental Results

As introduced, all the several tests were performed outdoor alternating morning and afternoon analyzes. A summary of the results is shown in Fig. 4.10. Here are noticed considerable power conversion efficiency variations, with a remarkable efficiency increase in the afternoon and this effect results systematic from the morning to the afternoon in all samples.

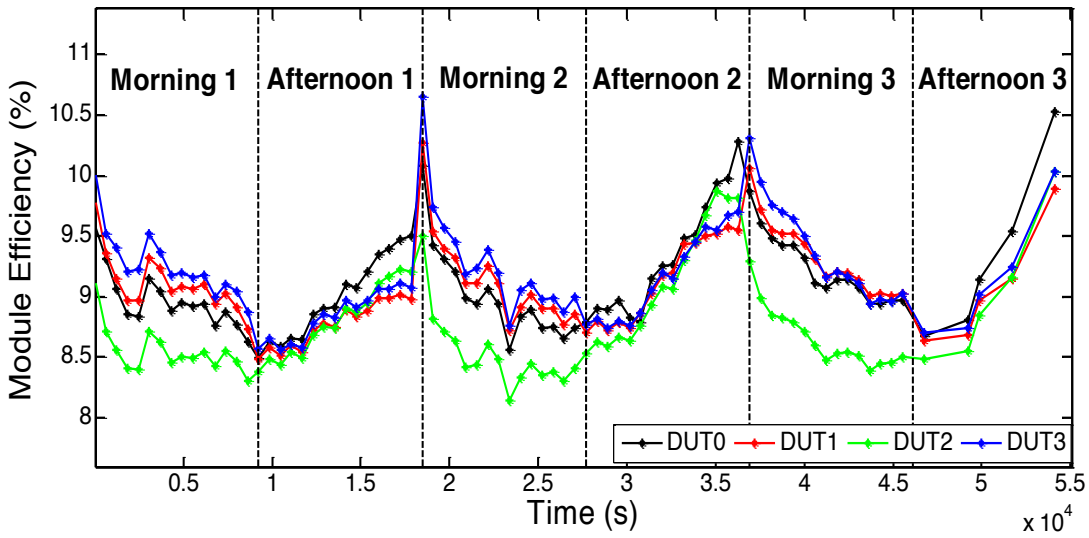

Fig. 4.10. Historical data trends of the overall conversion efficiency for the tested stabilized PV devices, during the stress tests carried out.

Figs. 4.11 (a, b, c) consider individually the main solar cell parameters normalized to the illumination, considering as e.g. the 1° afternoon case. On it we can easily observe that the efficiency improvement is due principally to a J_{SC} and fill factor increase and a R_{OC} reduction.

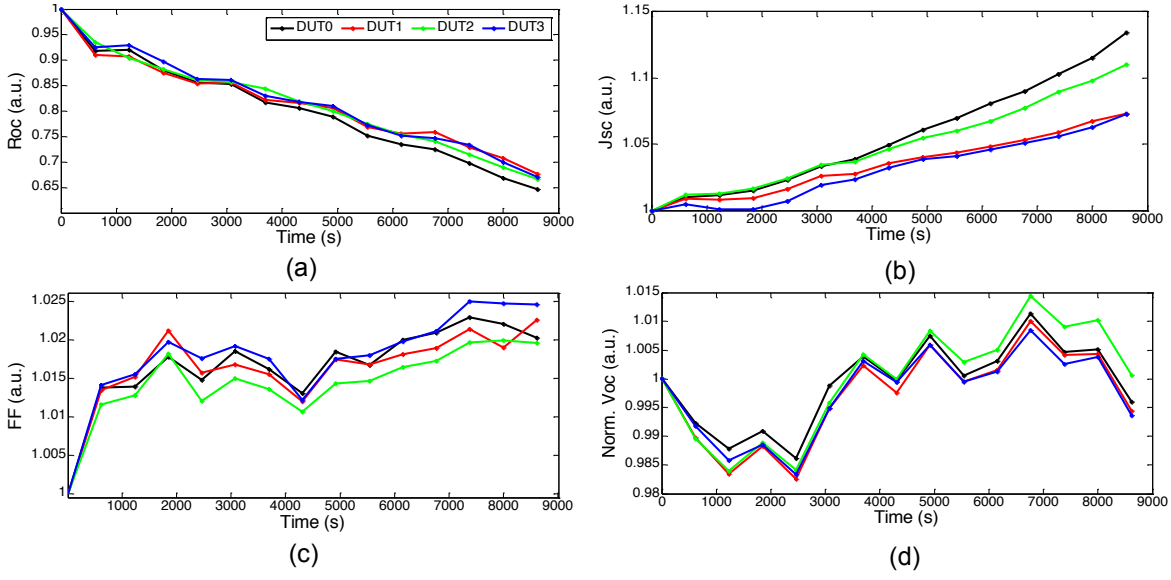

Fig. 4.11. Normalized (to light intensity) data trends of: (a) Series resistance, R_{OC}; (b) Short circuit current density, J_{SC}; (c) Fill Factor; (d) Open circuit voltage, V_{OC}, of the tested PV devices, in the 1° afternoon test of Fig. 4.10.

Obviously, in addition to the lighting variation, the temperature variation of the DUTs should also be considered, since a cooling of the PV modules in the afternoon is expected. To estimate the temperature variations of the DUTs, indoor measurements of the V_{OC} was performed at constant temperature for different irradiation values and extracted, from the solar panel datasheets, the V_{OC} variation with the temperature at constant illumination, resulted equal to -0.30%/°C.

Therefore, from this dual information the temperature variations was evaluated and, by using the V_{OC} vs time data corrected for the lighting level, normalized the results for the temperature and illumination changes. The data are reported in Fig. 4.11(d).

In this way, we estimated the temperature variations of the minimodules (see Fig. 4.12a, related to the 1° afternoon case) and, starting from these variations and from the maximum electric power variation with the temperature at constant illumination (-0.24%/°C), we evaluated the efficiency variations of the DUTs, corrected for the lighting and temperature variations (Fig. 4.12b).

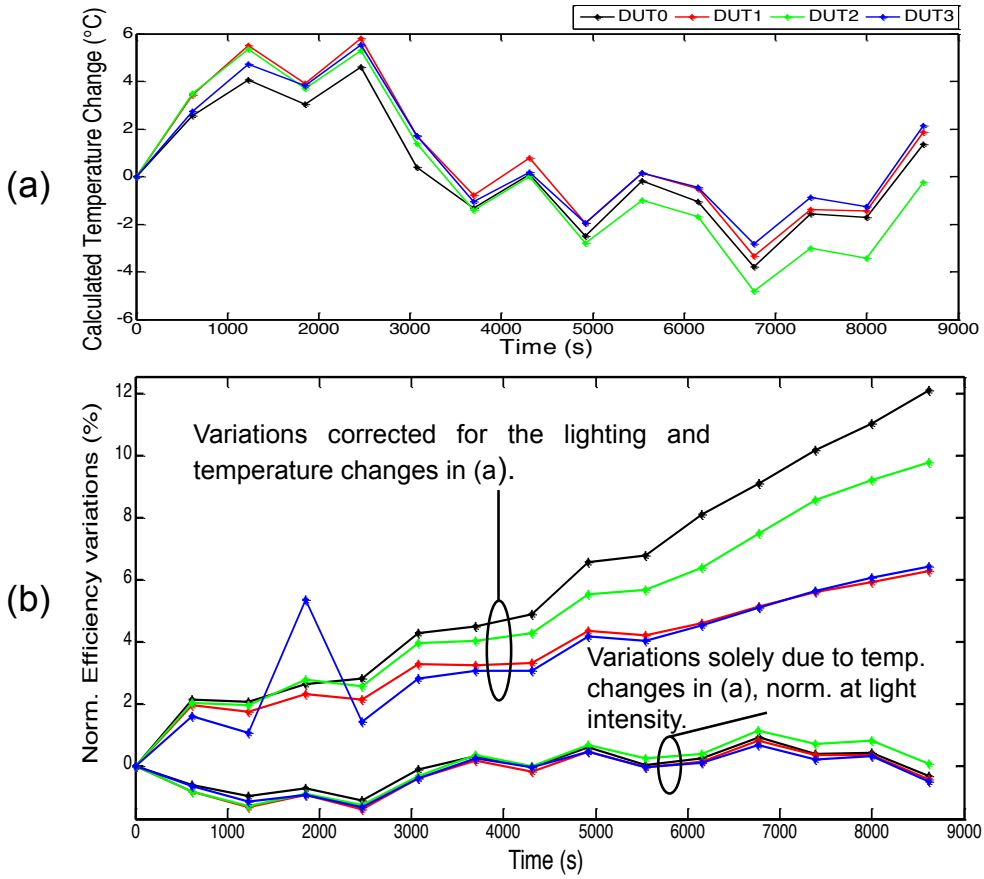

Fig. 4.12. (a) Calculated temperature changes and (b) Normalized overall conversion efficiency variations trends, for the tested devices, during the 1° afternoon test of the fig. 4.10.

4.2.3. NIR Effect

From these normalized data we notice a remarkable efficiency increase in the afternoon. The large power conversion efficiency increase from the morning to the afternoon is a very reproducible effect, and moreover, at the early stages of the morning outdoor tests, the modules maintain initially the larger efficiency found at the end of the previous afternoon.

The cause of such effect seems to be the linked to the variation of the incident spectrum on PV modules from morning to afternoon; as clear visible in Fig. 4.13, during the afternoon the red-infrared component becomes heavier.

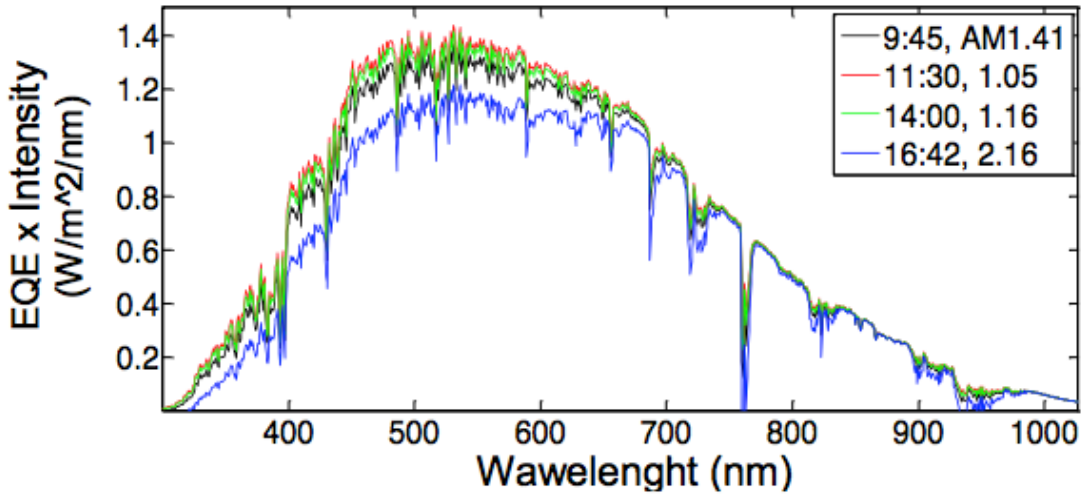

Fig. 4.13. EQE x Intensity of the incident solar radiation at the tested devices, at different hours of the day (July 2017).

So, there may be an improvement due to the more intense (with respect to the visible portion) Near-InfraRed (NIR) component in the afternoon. This confirm what we have seen previously on single a-Si:H cells analysis. As reported in Fig. 3.12, indeed, that cells were subjected to stress under monochromatic light at various wavelengths, and only in the NIR range varying from 700 nm to 800 nm a significant quantum efficiency improvement was detected. This really means that this effect might be responsible for the performances instability observed.

Chapter 5

Dye Sensitized Solar Cells Analysis

5.1. Dye Sensitized Solar Cell Overview

Dye-Sensitized Solar Cells (DSSCs) have been studied extensively and have attracted much attention in recent years because of its low cost and high efficiency, making them very promising for different photovoltaic applications [48-52]. The DSSC is constituted by three key components placed in succession: the photoanode, the electrolyte and the cathode. The photoanode consists of a conductive transparent substrate such as fluorine doped SnO_2 (FTO) – glass covered by a thin mesoporous layer of semiconductor nanoparticles (such as TiO_2, ZnO, SnO etc..) [53] sensitized by a dye, which extends the absorption properties of the TiO_2 to the visible region of the solar spectrum. The cathode electrode (CE) consists of a conductive substrate on which it is deposited a catalyst material such as platinum or a carbon based material (carbon nanotubes, graphite, graphene, etc.). In order to prevent electrolyte leakage a gasket sealant materials such as ionomeric polymer (Surlyn) [54] is placed between photoanode and cathode. The DSSC's working steps can be outlined by the following main processes:

1) Absorption of the light by the dye;
2) Injection of the electron in the semiconductor's conduction band and oxidation of the dye;
3) Migration of the electron through the semiconductor's film to the cathode;
4) Catalysis of the triodide-iodide reaction;
5) Reduction of the oxidized dye by the iodide.

These main processes are schemed below according the following equations:

$$S + hv \rightarrow S^* \qquad \text{Eq. 1}$$

$$S^* + TiO_2 \rightarrow S^+ + e^-_{(cb)}\,(TiO_2) \qquad \text{Eq. 2a}$$

$$S^* \rightarrow S \qquad \text{Eq. 2b}$$

$$2\,S^+ + 3\,I^- \rightarrow 2\,S + I_3^- \qquad \text{Eq. 3a}$$

$$S^+ + e^-_{(cb)}\,(TiO_2) \rightarrow S + TiO_2 \qquad \text{Eq. 3b}$$

$$I_3^- + 2\,e^-(catalyst) \rightarrow 3\,I^- \qquad \text{Eq. 4a}$$

$$I_3^- + 2\,e^-_{(cb)}\,(TiO_2) \rightarrow 3\,I^- + TiO_2 \qquad \text{Eq. 4b}$$

The dye, upon absorption of a photon (hν), goes to an electronically excited state S* (Eq. 1) which lies energetically above the Conduction Band (CB) edge of the semiconductor nanoparticles (Eq. 2a) and injects an electron into the TiO2 conduction band. The deactivation reaction (Eq. 2b) is a relaxation of the excited states, which occurs in competition with the electron injection into the TiO_2. The collection efficiency of the photo-injected electrons at the anode back contact is hindered by two major recombination processes, which are shown in Eq. 3b (back electron transfer) and in Eq. 4b (the TiO_2 conduction band electron captured by the oxidized redox couple).

These two processes are in competition with the oxidation of iodide (Eq. 3a) and reduce the current production of the cell. In the external circuit, the injected electrons give a current flow and provide for the reduction of iodine at the CE (Eq. 4a). One of the most important components of the DSSCs is the dye.

Commonly, transition metal coordination compounds such as ruthenium [55, 56] and osmium [57-59] polypyridil complexes and synthetic organic dyes [60,61] are used as effective sensitizers [62]. Over the last two decades' ruthenium complexes, equipped with appropriate ligands and anchoring groups, have been the most widely used choice of charge transfer sensitizers for mesoscopic solar cells [55, 63]. Each process needs to be concerted with the others in order to obtain the best performance.

Many factors, such as the composition and structure of the two electrodes, the type of redox electrolytes and the nature of the sensitizers, still affect the performance of DSSCs, rendering its long-term stability a major issue. In the last years many efforts have been done in developing chemical strategies to improve the stability and the efficiency of such cells [67-72]. Also the effect of electrical stresses has started to be investigated. The study of reverse bias applied pulses has provided valuable information regarding the chemical stability of the dyes in their oxidized states [73].

Moreover, in the case of forward bias pulses, Zhang et al. showed the ability to recover the degradation of quasi-solid state DSSCs after prolonged exposure to illumination. Up to 30.7% of the solar energy conversion efficiency of a degraded polymer based DSSC was recovered by applying an electrical double-pulse in a Poly(VinyliDene Fluoride) (PVDF) based DSSC [74]. Starting from these works, the effect of bias stress in liquid electrolyte based DSSCs both in forward and in reverse bias was systematically investigated.

It is shown and discussed the effect on the open circuit voltage (V_{OC}), short circuit current (J_{SC}), series resistance (R_{OC}), fill factor (FF) and power conversion efficiency of liquid electrolyte DSSCs with an N719 dye as a function of the levels of voltage applied, stress time, illumination intensity, and type of electrolyte. Based on the above observations the study proposes possible mechanisms responsible for the performance improvement.

5.2. Experimental Details and Conditions

The FTO-glass (7 ohm/□), used for the preparation of transparent electrodes, was first cleaned in a detergent and then washed with deionized water and ethanol. These conductive glassy plates were immersed in a $TiCl_4$/water solution (40 mM) and kept at 70°C for 30 min, then washed with water and ethanol and dried in oven at 70°C for 30 min. A TiO_2 layer was deposited on the FTO glassy plates by screen printing (frame with polyester fibres 43 T). This procedure, involving two steps (coating and drying at 125°C), was repeated twice. The TiO_2 coated plates were gradually heated up to 325°C, after the temperature was increased to 375°C in 5 min, and afterwards to 500°C. The plates were sintered at this temperature for 30 min [53], finally cooled down to room temperature and cut into rectangular pieces (area: 2 cm x 1.5 cm).

Afterwards, the TiO_2 film was treated with 40 mM $TiCl_4$ solution, following the procedure previously described, rinsed with water and ethanol and, finally, sinterized at 500°C. Each anode resulted in a transparent mesoscopic oxide film, with a thickness of 12 μm and a spot area of 0.196 cm2, deposited on a rectangular FTO-glass. A titanium oxide scattering layer (4 μm) was screen printed (employing a screen printing paste furnished by Dyesol, sized 150-200 nm). The dye-sensitized films were prepared using a 0.3 mM N719 solution (ditetra-butylammonium-cis-bis (isothiocyana-to)bis(2,2′-bipyridyl-4,4′-dicarboxylato)-ruthenium(II)), which was obtained dissolving the dye in a mixture of acetonitrile and tert-butyl alcohol (volume ratio 1:1).

The titania films were immersed into the N719 solution overnight at room temperature. After that all the dyed films were washed with acetonitrile and stored in the dark. Each counter-electrode consisted in an FTO-glass plate (area: 2 cm x 2 cm) on which a hole (1.0 mm diameter) was drilled. The perforated substrates were washed and cleaned with water and ethanol in order to remove any residual of glass powder or organic contaminants. The Pt transparent catalyst was deposited on the conductive face of the FTO glass by dropping H_2PtCl_6 solution (5 mM in isopropanol) and by heating at 500 °C for 30 min. The mesoporous titania films based photo anode and the Pt counter-electrode were assembled into a sandwich type arrangement and sealed (using a thermo press) with a hot melt gasket

made of the Surlyn ionomer. The aperture of the surlyn frame was larger than the TiO_2 area (cell active area 0.20 cm^2). A drop of electrolyte solution was put on the hole of the cathode and the cell was placed in a small vacuum chamber to remove air inside. The subsequent exposure to ambient pressure causes the electrolyte diffusion into the cell.

Finally, the hole was sealed by using another Surlyn film and closed by a thin cover glass. An additive sealing with epoxydic resins to avoid the leakage of solvent vapours out from the cell and insure a longer temporal stability of the device was applied. Three different electrolyte solutions, using all a mixture of acetonitrile/valerionitrile (85/15 v/v) as solvent and having the following compositions, were used respectively:

Type A: 0.05 M I2, 0.8 M LiI;

Type B: type A with addition of 0.6 1-Methyl-3- propyl imidazolium iodide (MPII);

Type C: type B with addition of 0.1M guanidium thiocyanate (GuSCN), and 0.5 M 4-tert-butylpyridine (TBP).

The DSSCs were analyzed by acquiring the current-voltage (I-V) curves in dark and under illumination conditions using a probe station with a temperature controlled chuck. Solar cell illumination was achieved with an AM1.5G spectrum by using a 92191-1000 Newport solar simulator assisted, in some cases, by a system with mirrors and Fresnel lenses to change the light intensity by focusing or de-focusing the solar simulator light beam. The maximum light illumination level was up to about 12 equivalent suns. The illumination light entered in the cells from the photo-anode.

All the I-V measurements to test the solar cells were performed with the voltage varying in the -0.1 to +0.8 V range by using a Keithley 2602A SMU connected via a GPIB bus interface to a PC for computer control. In fact, the basic purpose of this work is to understand the effect of electric field / bias stresses on the DSSC cell I-V characteristics, and this was the reason to limit the explored voltage range (from - 0.1 V to +0.8 V) in the I-V sweep used to measure the solar cell parameters, in order to reduce as much as possible the amount of additional voltage stress both in terms of duration and of voltage level.

The constant voltage stresses were performed under constant illumination conditions by using a DC bias voltage varying in the -3 V to +3 V range. Single stress durations varied in the 5 – 15 s range. The DSSCs temperature was maintained in the 20 – 25 °C range by using a cooling system consisting of the chuck plus three fans properly oriented towards the cells to avoid cell overheating due to the exposure to the light of the solar simulator. The DSSCs temperature was monitored through an NTC (Negative Temperature Coefficient) thermistor sensor placed in contact with the cell top glass. The

transient under dark and light were acquired with the Keithley 4200 using the four-point measurement. The initial power conversion efficiencies of the cells at 1 sun with AM1.5G spectrum illumination were typically about 3% with open-circuit voltage of 0.56 V, short-circuit current densities of 8 mA/cm^2 and fill factor of 67%.

5.3. Experimental Results

Since, as shown in a following section, the DSSCs assembled with type C electrolyte showed better performance compared to the others, we carried out most of our experiments using this electrolytic mediator.

5.3.1. Temperature dependence

As first step we have investigated the role of temperature on the electrical stress of the DSSCs, since this parameter plays a major role in the solar cell stability. Fig. 5.1 shows the behaviour of current-voltage curves for a champion DSSC with varying temperature and under illumination.

It is evident that up to 40 °C the I-V curves shift toward lower power conversion efficiencies as the temperature increases. Since the solar cell characteristics worsen at high temperature, we performed all the measurements and stresses at 20-25 °C.

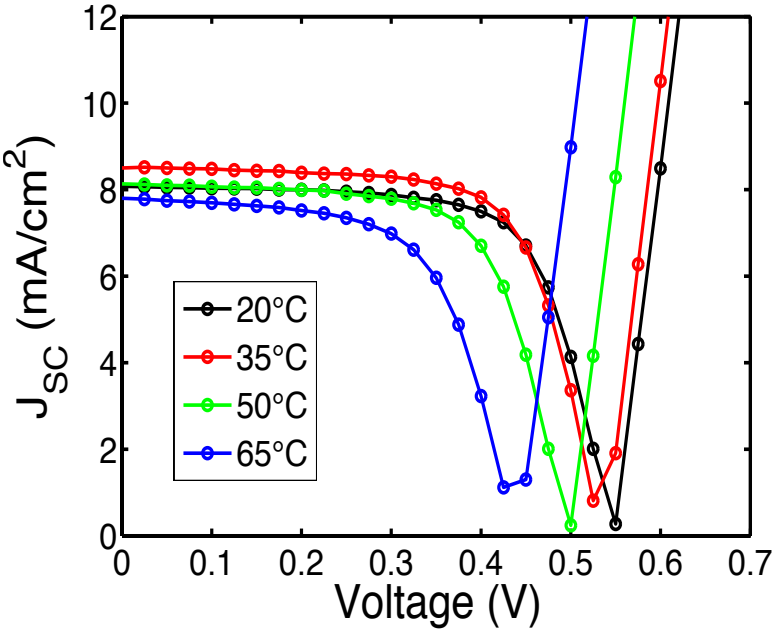

Fig. 5.1. DSSCs temperature dependence under a light exposure of 1 equivalent sun.

5.3.2. Bias Effect

The effect of the application of a bias with a constant electric field to the DSSCs was then analyzed. The cells were stressed using eight different voltage levels (in the -3/+3 V range) at fixed illumination level of 1 equivalent sun. The results are shown in Figs. 5.2 and 5.3.

For each stress sequence an initially fresh solar cell was used, and the evolution of its electrical performance was monitored by measuring the initial I-V curve and subsequent ones, recorded by temporarily stopping the stress and measuring the I-V sweep. Fig. 5.2 reports the I-V curves, while Fig. 5.3 shows the DSSC short circuit currents (J_{SC}) normalized to the respective initial value.

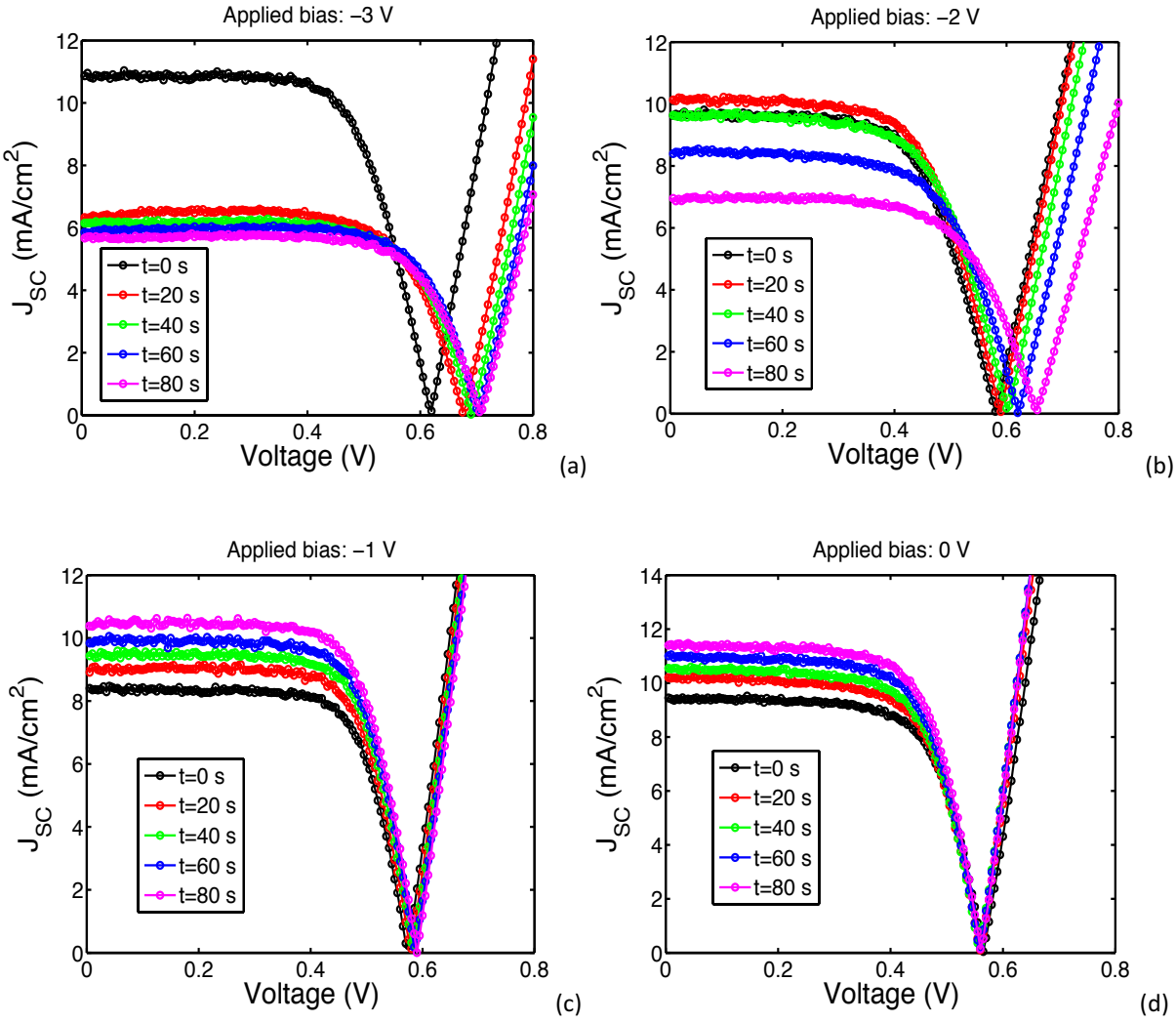

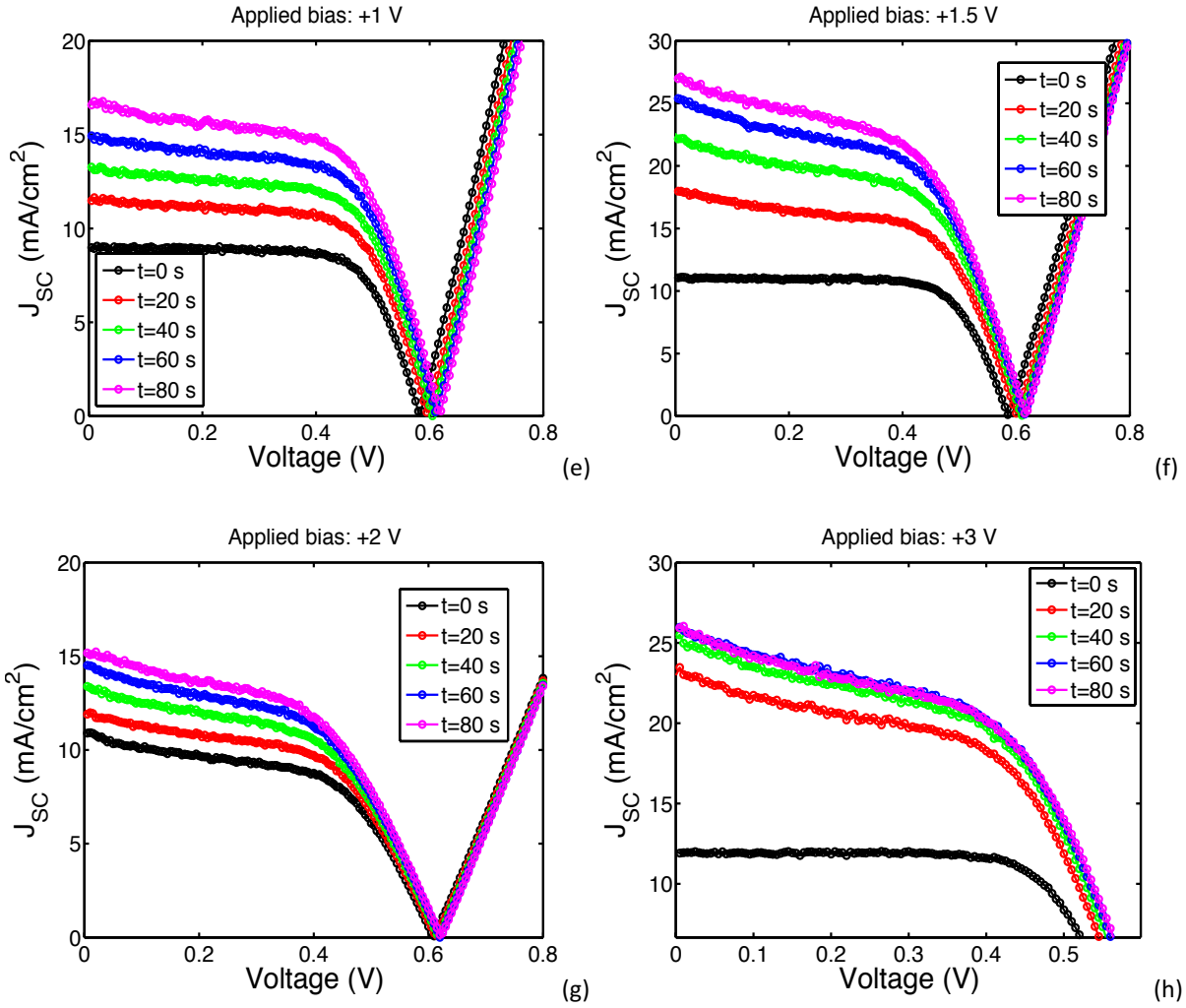

Fig. 5.2. Data trend analysis observed applying a bias of (a) -3 V, (b) -2 V, (c) -1 V, (d) 0 V, (e) +1 V, (f) +1.5 V, (g) +2 V, (h) +3 V under a light exposure of 1 equivalent sun.

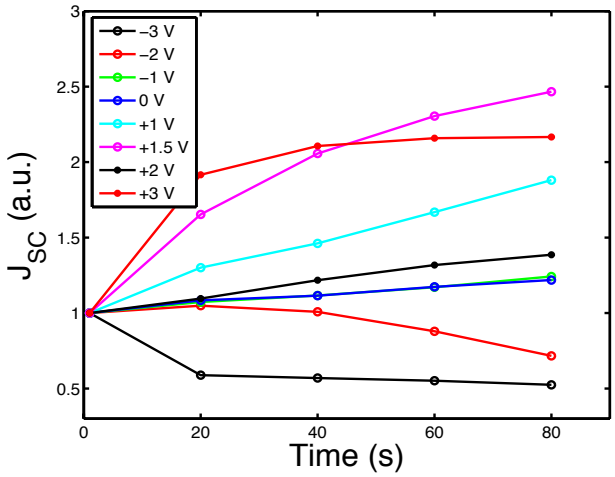

Fig. 5.3. Normalized data trend analysis for J_{SC} as a function of stress time for different bias voltages under a light exposure of 1 equivalent sun.

As it can be clearly seen from the figures above, by applying a bias larger than -1 V the I-V curves improve and shift toward higher power conversion efficiencies as the stress time increases. The DSCC improvement is mainly associated with an increase of the J_{SC} value. By applying a negative voltage stress below -1 V, we assist, on the contrary, to a collapse of J_{SC}.

5.3.3. Combined Bias - Light Effect

A second set of measurements was so focused to the dependence on light intensity of the above DSSC parameter instability to voltage stresses. Figs. 5.4 and 5.5 show the results of stresses at a fixed voltage of +1 V, performed in the same way of the experiment previously described, at eight different light intensity levels (starting from ≈ 0.01 up to 12 equivalent suns). Fig. 5.4 reports the I-V curves, while Fig. 5.5 shows the DSSC short circuit currents (J_{SC}), all normalized to the respective initial value.

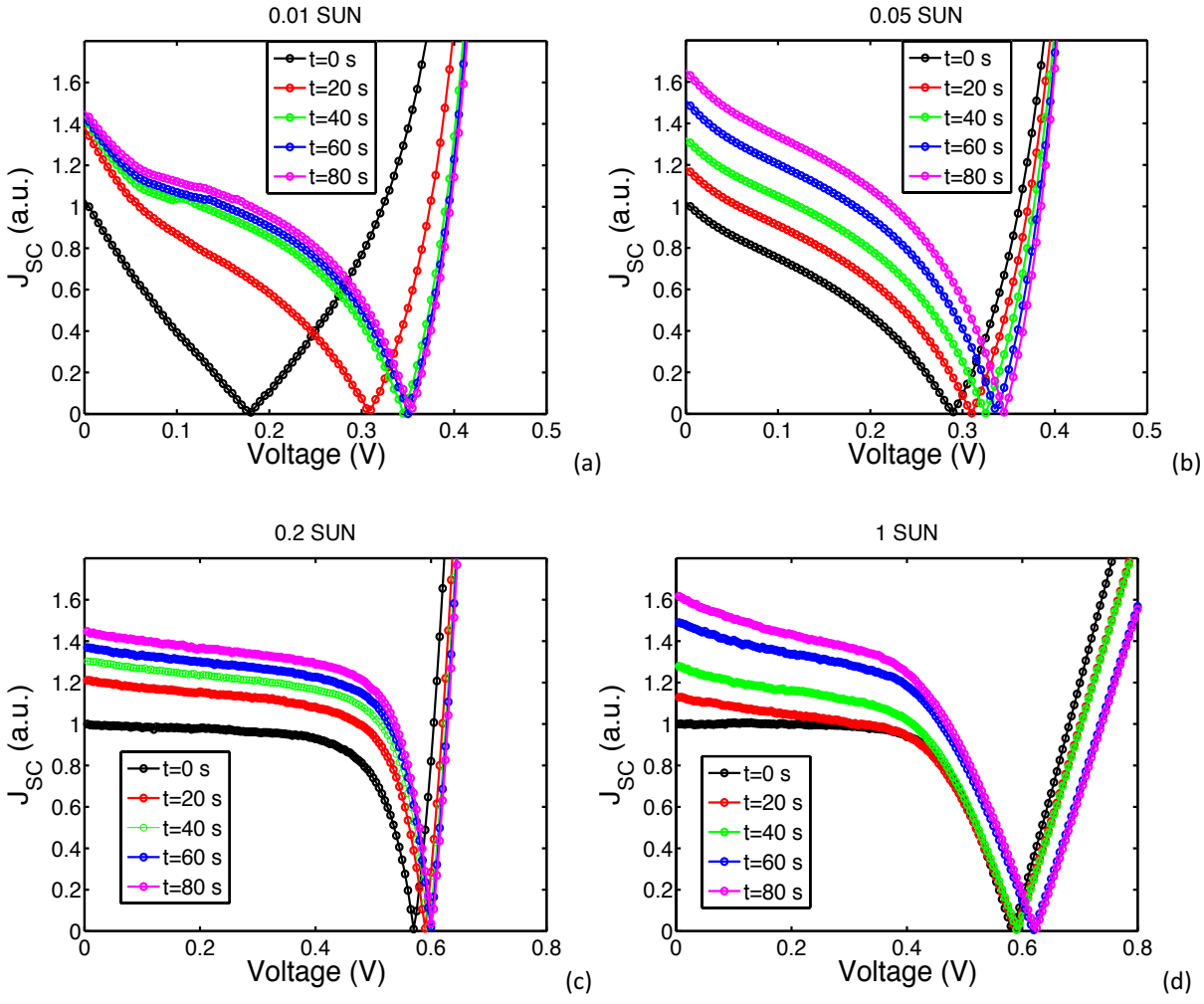

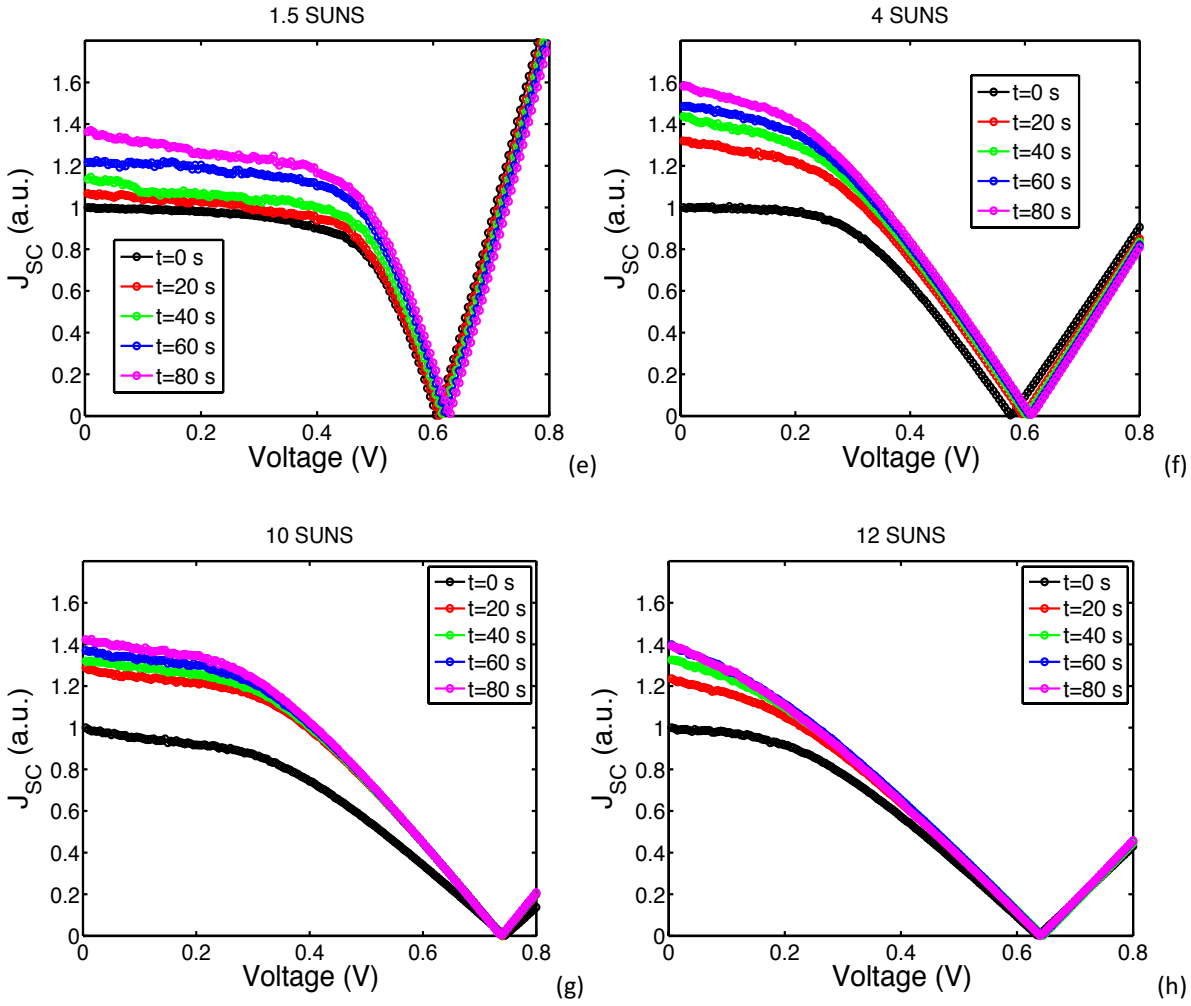

Fig. 5.4. Data trend analysis observed applying a fixed stress voltage bias of +1 V under an equivalent light exposure of (a) 0.01 sun, (b) 0.05 sun, (c) 0.2 sun, (d) 1 sun, (e) 1.5 suns, (f) 4 suns, (g) 10 suns, (h) 12 suns.

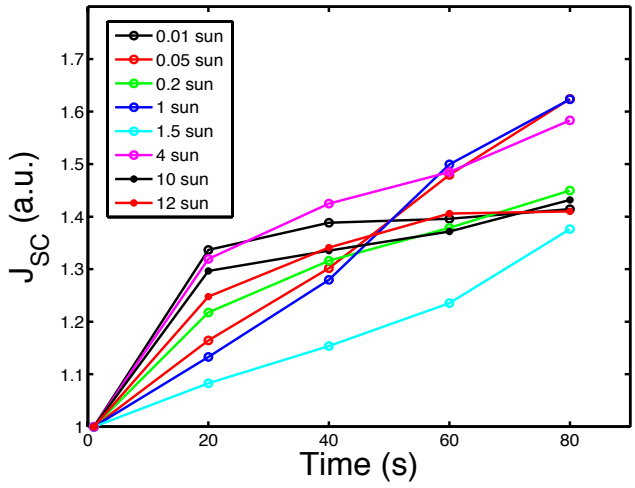

Fig. 5.5. Normalized data trend analysis for J_{SC} as a function of stress time for different light exposures at fixed stress voltage bias of +1 V.

As evident from the graphs above, almost independently of the illumination level the short circuit current J_{SC} has approximately the same linear growth trend with the stress time in all cases. That is, the increase of light intensity during the stress reduces the improvement on the DSSC parameters. We therefore conclude that the DSCC improvement is mainly associated to the application of a suitable voltage, slightly negative or positive, and the light presence has almost no effect.

5.3.4. Reversibility of DSSC Parameters

In a third set of experiments it was investigated whether the above discussed effects of improvement / worsening of the solar cell parameters under bias stress are reversible. In particular, the effect of the application of consecutive positive and negative bias stresses were studied. Fig. 5.6(a) shows the I-V characteristics of a DSSC at a light intensity of 1 equivalent sun, starting from the fresh solar cell, followed by the I-V after a 20 s long reverse bias stress at -3 V, then by the I-V after a 20 s long forward bias stress at +1.5V, and so on, repeating three times in total this sequence of negative stress / I-V measure / positive stress / I-V measure. To simplify the Fig. 5.6(a) reading, Fig. 5.6(b) shows the trend of the J_{SC} value measured after each I-V trace in this cell.

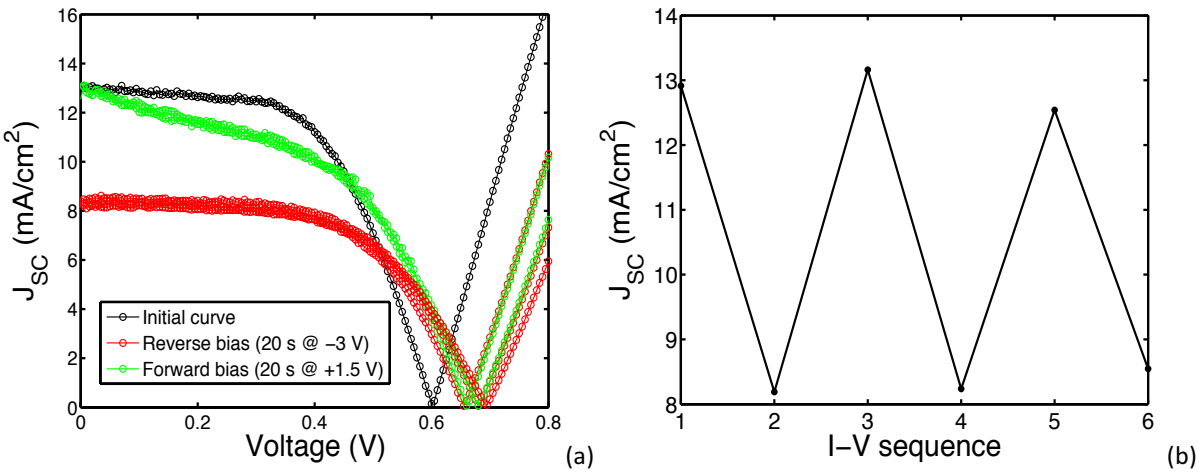

Fig. 5.6. Data trend observed applying, alternately, a bias of -3 V first and a bias of +1.5V after. The figure shows (a) the I-V reversibility sequence and (b) the short circuit current density trend as function of applied stress.

As highlighted in Fig. 5.6, the process of the DSSC characteristics improvement results completely reversible. In these graphs it is clear that the J_{SC} and the overall I-V curves go up and down according to the applied stress voltage.

5.3.5. Improvement Limit

Fig. 5.7 shows the effect of prolonged stress at +1.5 V at 1 sun equivalent illumination. It is evident that the DSSC I-V characteristics improve for the first 80-100 min, and then a decrease of efficiency starts to appear.

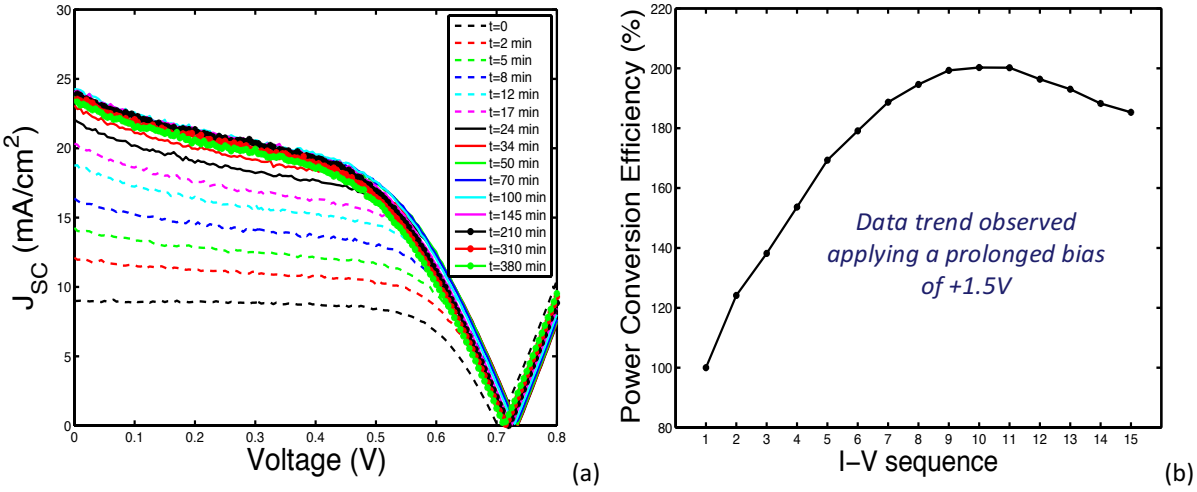

Fig. 5.7. Data trend observed applying a prolonged bias of +1.5V. The figure shows (a) the I-V sequence and (b) the power conversion efficiency trend as function of applied positive bias.

5.3.6. Electrolyte Analysis

To better investigate the aforesaid improvement also the role played by the electrolyte was investigated. The three different types of electrolyte (type A, B, and C) described in the experimental section were compared. Fig. 5.8a reports the time evolution of the open-circuit voltage for three DSSCs realized with the different electrolytes respectively. The stress is simply obtained by light exposure under open circuit conditions.

Note that the stress under open circuit condition is at an almost constant positive voltage, equal to the V_{OC}, i.e., approximately equal to 0.6 V for these cells. Fig. 5.8b shows the behaviour of the short circuit current for the three electrolytes in stresses obtained by light exposure under short circuit conditions, i.e., at V = 0 V, according to the definitions of Figs. 5.2 and 5.3.

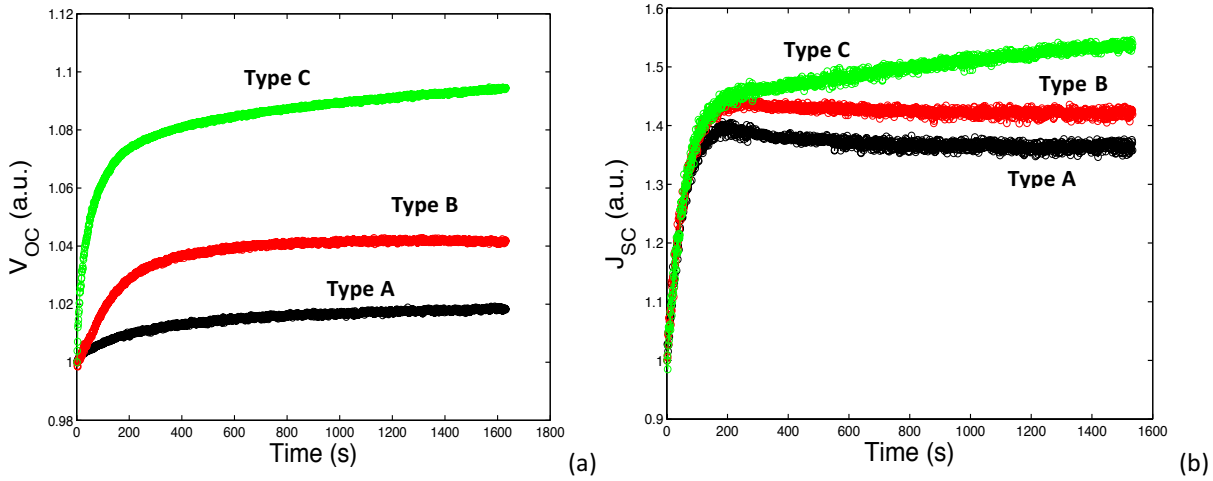

Fig. 5.8. Normalized data trend for (a) V_{OC}, (b) I_{SC} as function of time for the three different types of electrolyte: types A, B and C.

From the figures above, it is observed that the type C cells show a significant increment of the short-circuit current (50%) and of the open circuit voltage (10%), after about 1/2 hour. Fig. 5.8 also shows the V_{OC} and I_{SC} transients for the type A and B DSSCs. We observe the same trend found for the type C cell, though the maximum percentage change of V_{OC} and I_{SC} are lower. Further information is provided by measurements of the solar cell dark current in forward bias. In fact, as discussed above, the DSSC improvement effect is not related to light exposure. On the other hand, the transient of the DSSC dark current in forward bias may provide information about the lifetime of the charge carriers in the DSSC junction region, since the charge transport in forward bias in dark condition for these DSSCs is likely due to electron-hole recombination at the TiO_2 / Dye / Electrolyte interface, as shown in Reference [76]. Fig. 5.9 reports the time evolution at room temperature of the DSSC dark current in forward bias at a polarization voltage equal to the respective V_{OC} for the investigated cells.

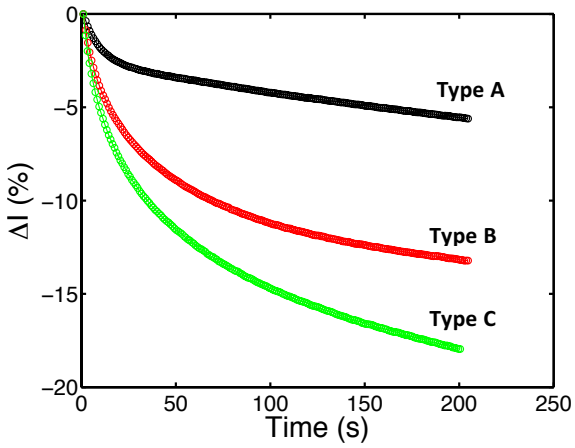

Fig. 5.9. Relative variation of the dark current measured at forward bias corresponding to the respective V_{OC}, as a function of the time for the investigated cells A, B, and C.

We note that for the investigated stress time the relative variation of the dark current with respect to the initial value is the largest for the type C cell, followed by the type B and type A. The same trends are found for the I_{SC} and V_{OC} variations under illumination reported in Fig. 5.8: the variations are the largest for the type C cell, followed by the type B and A. Moreover, the relative variation and the shape of the dark current time dependence are similar to those observed for the J_{SC} transient. This suggests that the J_{SC} and dark current variations have the same cause and also most likely can be due to a variation of the lifetime of the electrical charge carriers (electrons and holes) at the TiO_2 / dye / electrolyte interface. In fact, it is known that the main contribution to the forward bias dark current in a DSSC is the recombination of electrons from the TiO_2 conduction band with I3-, i.e. the reaction reported in Eq 4(b). If for some reason the recombination of the electrons with holes decreases, i.e., if the recombination lifetime increases, then the dark current will also decrease by the same measure. This in turn may induce a larger photocurrent, i.e., a larger J_{SC} since the net number of photo-carriers collected at the contacts is the fraction of excitons that survive to recombination.

The carrier lifetime improvement may be explained by different processes. One may involve point defects in the TiO_2 dielectric close to the TiO_2 / dye / electrolyte interface. Such defects may trap charges and become inactive to assist electron-hole recombination, thus promoting carrier lifetime increase. Another possibility is to consider a mechanism involving the motion of light ions in the electrolyte, for example Li+, which may have trapped at the TiO_2 interface due to the forward bias applied to the cell (negative voltage on the TiO_2). Indeed, for the case of Li+ ions it has been suggested that such ion trapping, localized at the TiO_2 surface, reduces the recombination of the conduction electrons of the TiO_2 with holes of the electrolyte [75].

Under illumination, this reduction of recombination rate increases J_{SC}, V_{OC} and the overall cell efficiency. The comparison of the V_{OC} and J_{SC} transients for various electrolytes shown in Fig. 5.8, may indicate that by adding suitable species to the electrolyte which are adsorbed on the TiO_2 surface (such as MPII, GuSCN and TBP), the chance of interface electron-hole recombination further decreases, and this improves the DSSC behaviour. The application of a reverse bias, on the contrary, should remove the Li^+ ions; in this condition would increase the electron-hole recombination rate and it would favour the decrease of J_{SC}. The Li^+ ion removal under reverse bias stress may also explain the increase of V_{OC}, since it should favour the TiO_2 depletion, and therefore the V_{OC} increasing. This effect, however, could also be explained by the charge state change of point defects in the TiO_2 close to the TiO_2 / dye / electrolyte interface. The cause for the observed DSSC instability, whether due to the motion of light ions in the electrolyte and adsorption at the interface or to defects in the TiO_2 changing their charge state under electrical stress is still unclear, though its effects are extremely evident.

Chapter 6

Conclusions and Future Developments

This section is dedicated to the synthesis and analysis of the results obtained during this work. Based on what has been achieved through experimental data, the possible industrial applications are here examined and then the necessary in-depth activities related to future dedicated research steps are also discussed.

The preliminary analysis initially conducted to define the sample preparation conditions, affirms the great importance of hydrogen dilution of silane-processing gas into the deposition process of amorphous silicon. By comparing the two different H_2/SiH_4 ratios used to obtain the reference baseline a-Si:H cells, it resulted in fact immediately evident (an identical behavior was noted on different intrinsic thicknesses layers) the better overall performance shown by the R=5 option against the less value R=2. Furthermore, the preliminary analysis directed to study the degradation of the solar cells under light soaking in short circuit conditions confirmed that the degradation rate results an increasing function of the incident light intensity.

Regarding the overall sets of experiment conducted on the single junction a-Si:H cells, in summary, it was shown that the application of a reverse bias to a-Si solar cells not only can recover its light-induced degradation (caused mainly by the Staebler-Wronski effect and by the increase of the series resistance) but it can also produce an improvement of the performance, especially of the series resistance, of the open circuit voltage, and of the overall power conversion efficiency. To further investigate such recovery/improvement kinetics, various experiments were performed: as a function of reverse bias voltage, illumination, temperature, type of contact to the p-type a-Si:H film, and also in individual a-Si:H doped films (not solar cells). The overall results may be explained by assuming that the improvement of series resistance and fill factor in the p–i–n solar cells, and of the sheet resistance in individual p-type a-Si:H films deposited on SiO_2 is due to the motion of light ions from the oxide to the a-Si:H films (or vice-versa) driven mainly by the electric field.

To confirm the theory according to which the improvement would be dictated by motion of ions from the oxide layer to the p-type a-Si:H film and viceversa, it was shown the radical difference of behavior between forward and reverse bias stress also for tandem a-Si:H / microcrystalline Si solar cells.

Comparing the micromorph solar cell stress results to the previous case of single junction amorphous Si PV cells we can state that while in the first case the required reverse voltage levels are much larger, of the order of -12V (corresponding to electric fields in the intrinsic layer of the a- Si:H cell of 5×10^5 V/cm), in the case of tandem amorphous/microcrystalline Si cell, the reverse bias voltage at which the best improvement results are found is -4V, which corresponds to a much lower electric field in the intrinsic regions, of about 2×10^4 V/cm. That is, the improvement effect is observed at an electric field of a factor 25 x lower.

The lower electric field required to trigger the improvement effect in the case of a tandem amorphous/microcrystalline Si cell may be consistent to the case of the single junction a-Si:H cells. In fact, for the case of the single-junction a-Si:H PV cell, the improvement effect was attributed to the migration/field-assisted diffusion of charged impurities, most likely related to H species; here, in the case of micromorph cells, the microcrystalline Si layer has a large hydrogen concentration, much larger than the SnO_2:F TCO, and this may render easier the H diffusion toward the a-Si:H cell, and therefore the improvement effect observable at a lower electric field.

Furthermore, the analysis conducted on the tandem amorphous/microcrystalline Si solar cells minimodules fabricated by 3SUN showed a remarkable and reproducible efficiency increase in the afternoon caused by the clear variation of the incident spectrum on PV modules from morning to afternoon. Such 'NIR Effect' (during the afternoon the red-infrared component becomes heavier) seems to be linked to the range of wavelengths (700-800 nm range) needed to assist the recovery / improvement dynamics under DC voltage stress, found in the case of single junction a-Si:H cells analysis. This really means that this effect might be also responsible for the performances instability observed.

Even that, as previously pointed out, the behaviour of complete PV modules may be quite different compared to small area solar cells studied in this work, and of course, an energetic balance needs to be done in any case, the various experiments performed on doped single layers of a-Si:H, a-Si:H solar cells, and micromorph solar cells provide novel information on the improvement kinetics and on the possible causes and this may be surely extremely important from the point of view of potential applications. Indeed, on the basis of what was experimentally seen, it is not difficult to imagine an electrical-optical equipment capable of regenerate degraded photovoltaic modules or able to eliminate production defects as last step machine of a manufacturing chain. Nowadays it is not difficult, in fact, to think about a control electronics embedded to the single panel; just think, for example, to an integrated microinverter able to talk with a supercap and so through which may be possible to force an external bias to enhance the single panel overall performances.

Apart from the research already under way for commercial micromorph products, the natural continuation of the work carried out so far on amorphous cells is certainly the application of the above recovery / improvement techniques to heterojunction class solar cells. This technology represents, in fact, the new frontier in the field of commercial photovoltaics.

Regarding the Dye-Sensitized Solar Cells (DSSC), great attention was also addressed towards these new thin-film technologies main attractive for their innovative concept and for their promising low cost. For this type of cells, due the strong instability, the study was purely focused, as done in the case of a-Si:H solar cells, to counteract the degradation and trying, in this way, to make such instability phenomena also here reversible.

In this work it is shown that the application of a stress bias larger than -1 V to dye-sensitized solar cells not only can recover its light-induced degradation but it can also produce an improvement of the performance, especially of the series resistance, of the short circuit current, and of the overall power conversion efficiency. Even here, various experiments were performed: as a function of stress bias voltage, illumination and temperature conditions. It was investigated the spontaneous recovery / improvement of ruthenium-based DSSCs parameters with different electrolyte composition. It was also observed that drifts are present in dark conditions under forward bias, with the decrease of the dark current, which has a time-dependence similar to those of V_{OC} and J_{SC}. In addition, all the investigated DSSC, having the same electrolyte based on iodide/ iodine redox couple but different composition, have shown the same kind of instability. Moreover, both current–voltage and impedance measurements have shown that, during the current and voltage transients acquired in dark conditions and under illumination, an increase in electrons lifetime occurs.

The recovery/improvement of the performances is still not very clear, one of the most accredited causes could be attributable to the charge transport mechanism at the TiO_2/electrolyte interface and so to the increasing of the electron lifetime in the titania. This effect could be explained by intercalation of ions H^+ present in the electrolyte that limits the recombination of electrons from TiO_2 to the triiodide. However, as in the case of amorphous silicon based solar cells, even in this case, an in-depth study on possible causes should be further investigated; comparing the instability behavior of these cells involving several chemical species, could in fact clarify any doubts about instability processes.

In this way, by optimizing the techniques used in this study through a careful analysis related to the energy balance, as well as thought for the amorphous type cells, one could design in principle a suitable instrumentation capable of regenerate degraded photovoltaic modules.

Appendix A

Published Articles

A.1 Peer - Reviewed Publications

A.1.1 International Journals

- ***Role of electric field and electrode material on the improvement of the ageing effects in hydrogenated amorphous silicon solar cells***

  A. Scuto, L. Valenti, S. Pierro, M. Foti, C. Gerardi, A. Battaglia and S. Lombardo.
  Solar Energy Materials and Solar Cells 141, 203-209, 2015.

- ***Measurements and Simulations on the Mechanisms of Efficiency Losses in HIT Solar Cells***

  S. Pierro, A. Scuto, L. Valenti, M. Foti, A. Battaglia, G. Mannino, C. Gerardi, F. Crupi and S. Lombardo. *International Journal of Photoenergy 501, 515767, 2015.*

- ***Data supporting the role of electric field and electrode material on the improvement of the ageing effects in hydrogenated amorphous silicon solar cells***

  A. Scuto, L. Valenti, S. Pierro, M. Foti, C. Gerardi, A. Battaglia and S. Lombardo.
  Data in Brief 4, 518-523, 2015.

- ***Investigation of recovery mechanisms in dye sensitized solar cells***

  C. Chiappara, V. Figà, G. Di Marco, G. Calogero, I. Citro, A. Scuto, S. Lombardo, B. Pignataro and F. Principato. *Solar Energy 127, 56-66, 2016.*

- ***Effect of illumination and electric field intensity on the efficiency improvement of amorphous silicon tandem solar cells***

  A. Scuto, C. Gerardi, A. Battaglia and S. Lombardo.
  Journal of Vacuum Science and Technology B 35, 2017.

A.1.2 Conference Proceedings

- ***Improvement of solar cell performance and reversibility of ageing effects in hydrogenated amorphous silicon solar cells under illumination and electric field stress: role of TCO and substrate***

  A. Scuto, M. Foti, C. Gerardi, A. Battaglia and S. Lombardo.
  IEEE International Reliability Physics Symposium (IRPS) – Pasadena, CA USA, April 2016.

- ***Improvement of DSSC performance by voltage stress application***

  A. Scuto, G. Di Marco, G. Calogero, I. Citro, F. Principato, C. Chiappara and S. Lombardo.
  IEEE International Reliability Physics Symposium (IRPS) – Pasadena, CA USA, April 2016.

- **Effect of field and pump light wavelength during DC stress on the efficiency improvement of amorphous silicon single junction and tandem solar cells**

  A. Scuto, C. Gerardi, A. Battaglia, A. Canino and S. Lombardo.
  IEEE International Reliability Physics Symposium (IRPS) – Monterey, CA USA, April 2017.

- **Performance Improvement of tandem amorphous / microcrystalline Si photovoltaic modules under changes in illumination conditions**

  F. Ricco Galluzzo, A. Scuto, C. Gerardi, A. Battaglia, A. Canino, F. Aleo and S. Lombardo.
  Abstract submitted for IEEE International Reliability Physics Symposium (IRPS) – San Francisco, CA USA, March 2018.

A.2 Conference Participations

A.2.1 Invited Talk

- ***Electric field stress effect and role of electrode material on the improvement of hydrogenated amorphous silicon solar cells***

  A. Scuto, L. Valenti, S. Pierro, M. Foti, C. Gerardi, A. Battaglia and S. Lombardo.
  Energy, Materials, and Nanotechnology (EMN) Photovoltaics Meeting - Hong Kong, January 2016.

A.2.2 Oral Presentations

- ***Direct voltage stress effect on dye sensitized solar cells performance***

  A. Scuto, G. Di Marco, G. Calogero, I. Citro, F. Principato, C. Chiappara and S. Lombardo.
  Italian National Conference on Condensed Matter Physics (FisMat) – Palermo, September 2015.

- ***Electric field stress effect and role of electrode material on the improvement of hydrogenated amorphous silicon solar cells***

  A. Scuto, L. Valenti, S. Pierro, M. Foti, C. Gerardi, A. Battaglia and S. Lombardo.
  Italian National Conference on Condensed Matter Physics (FisMat) – Palermo, September 2015.

- ***Improvement of solar cell performance and reversibility of ageing effects in hydrogenated amorphous silicon solar cells under illumination and electric field stress: role of TCO and substrate***

  A. Scuto, M. Foti, C. Gerardi, A. Battaglia and S. Lombardo.
  IEEE International Reliability Physics Symposium (IRPS) – Pasadena, CA USA, April 2016.

- ***Effect of illumination and electric field intensity on the efficiency improvement of amorphous silicon single junction and tandem solar cells***

  A. Scuto, M. Foti, C. Gerardi, A. Battaglia and S. Lombardo.
  Workshop on Dielectrics in Microelectronics (WoDiM) – June 2016.

- ***Efficiency improvement of amorphous silicon single junction and tandem solar cells through DC electric field stress***

  A. Scuto, C. Gerardi, A. Battaglia and S. Lombardo.
  Italian National Conference on Materials Science and Technology (MATERIALS) – Catania, December 2016.

- **Effect of field and pump light wavelength during DC stress on the efficiency improvement of amorphous silicon single junction and tandem solar cells**

  A. Scuto, C. Gerardi, A. Battaglia, A. Canino and S. Lombardo.
  IEEE International Reliability Physics Symposium (IRPS) – Monterey, CA USA, April 2017.

- **Performance Improvement of tandem amorphous / microcrystalline Si photovoltaic modules under changes in illumination conditions**

  F. Ricco Galluzzo, A. Scuto, C. Gerardi, A. Battaglia, A. Canino, F. Aleo and S. Lombardo.
  Submitted request for talk for IEEE International Reliability Physics Symposium (IRPS) – San Francisco, CA USA, March 2018.

A.2.3 Poster Presentation

- ***Data and modeling of transparent conductive oxide emitters for crystalline Si photovoltaic cells***

  S. Pierro, A. Scuto, L. Valenti, M. Foti, A. Battaglia, G. Mannino, C. Gerardi, F. Principato and S. Lombardo. *European Material Research Society (E-MRS) Spring Meeting – Strasbourg, May 2013.*

- ***Improvement of Hydrogenated Amorphous Silicon Solar Cells by Light Assisted Reverse Bias Stress***

  A. Scuto, L. Valenti, S. Pierro, M. Foti, C. Gerardi, A. Battaglia and S. Lombardo.
  Material Research Society (MRS) Spring Meeting – San Francisco, CA USA, April 2015.

- ***Investigation of recovery mechanisms in dye sensitized solar cells***

  C. Chiappara, V. Figà, G. Di Marco, G. Calogero, I. Citro, A. Scuto, S. Lombardo, B. Pignataro and F. Principato. *Italian National Conference on Condensed Matter Physics (FisMat) – Palermo, September 2015.*

- ***Improvement of DSSC performance by voltage stress application***

  A. Scuto, G. Di Marco, G. Calogero, I. Citro, F. Principato, C. Chiappara and S. Lombardo.
  IEEE International Reliability Physics Symposium (IRPS) – Pasadena, CA USA, April 2016.

List of References

[1] World Energy Assessment: Energy and the Challenge of Sustainability, United Nations Development Program, United Nations Department of Economic and Social Affairs, World Energy Council (Sept. 2000).

[2] I. Held and B. Soden, "Water Vapour Feedback and Global Warming," Annual Review of Energy and the Environment (Annual Reviews), no. 25, pp. 441-475, 2000.

[3] Kemp W, The Flow of Energy in a Hunting Society. Energy and Power, A Scientific American Book, W.H. Freeman and Company, San Francisco, CA, pp 55–65 (1971).

[4] F. Convery, "Issues in Emissions Trading - an Introduction," Environmental Institute, University College Dublin, Dublin, 2003.

[5] UNFCCC, "Status of Ratification of the Kyoto Protocol," 2012.

[6] IEA, "World Energy Outlook 2012," OECD/IEA, Paris, 2012.

[7] Martinot E, Ramankutty R, Rittner F, The GEF Solar PV Portfolio: Emerging Experience and Lessons, Monitoring and Evaluation Working Paper 2, GEF pre-publication draft (August 2000).

[8] IPCC, "Special Report on Renewable Energy and Climate Change Mitigation," Intergovernmental Panel on Climate Change, 2011.

[9] Green Rhino Energy, "Green Rhino Energy," Green Rhino Energy Ltd.

[10] A. Luque and S. Hegedus, Handbook of Photovoltaic Science and Engineering, 2nd ed. (John Wiley & Sons Ltd, West Sussex, England, 2003).

[11] IEA Photovoltaic Power Systems Implementing Agreement (PVPS), Annual Reports (2009).

[12] P. Hoertz, A. Staniszewski, A. Marton, G. Higgins, C. Incarvito, A. Rheingold and G. Meyer, "Toward Exceeding the Shockley-Queisser Limit: Photoinduced Interfacial Charge Transfer Processes that Store Energy in Excess of the Equilibrated Excited State," Journal of American Chemical Society, no. 128, pp. 8234-8245, 2006.

[13] M. Zeman and R. Schropp, Amorphous and Microcrystalline Silicon Solar Cells: Modeling, Materials, and Device Technology, Boston/Dordrecht/London: Kluwer Academic Publishers, 1998.

[14] A. Smets, W. Kessels and M. v. d. Sanden, "Vacancies and Voids in Hydrogenated Amorphous Silicon," Applied Physics Letters, vol. 82, no. 10, pp. 1547-1549, 2003.

[15] H. Fritzsche, "A New Perspective on an Old Problem - The Staebler-Wronski Effect," in Materials Research Society Proceedings, San Fransisco, 2010.

[16] D.L. Staebler, C.R. Wronski, Reversible conductivity changes in discharge-produced amorphous Si, Appl. Phys. Lett. 31 (1977) 292.

[17] D.L. Staebler, R.S. Crandall, R. Williams, Stability of n–i–p amorphous silicon solar cell, Appl. Phys. Lett. 39 (1981) 733.

[18] G.A. Swartz, Reverse bias and heat treatment to improve performance of a-Si solar cells, Appl. Phys. Lett. 44 (1984) 697.

[19] H. Fritzsche, Development in understanding and controlling the Staebler-Wronski effect in a-Si:H, Ann. Rev. Mater. Res. 31 (2001) 47.

[20] H.M. Branz, Hydrogen collision model: quantitative description of metastability in amorphous silicon, Phys. Rev. B 59 (1999) 5498.

[21] A. Luque, Steven Hegedus, Handbook of Photovoltaic Science and Engineering, Second Edition, John Wiley & Sons Ltd., UK, 2011.

[22] D.E. Carlson, K. Rajan, The reversal of light-induced degradation in amorphous silicon solar cells by an electric field, Appl. Phys. Lett. 70 (1997) 2168.

[23] D.E. Carlson, K. Rajan, Evidence for proton motion in the recovery of light-induced degradation in amorphous silicon solar cells, Appl. Phys. Lett. 83 (1998) 1726.

[24] T. Shimizu, Staebler-Wronski effect in hydrogenated amorphous silicon and related alloy films, Jpn. J. Appl. Phys. 1 (43) (2004) 3257.

[25] A. Smets, C. Wronski, M. Zeman and M. v. d. Sanden, "The Staebler-Wornski Effect: New Physical Approaches and Insights as a Route to Reveal its Origin," in Materials Research Society Proceedings, San Fransisco, 2010.

[26] A. Kolodziej, Staebler-Wronski effect in amorphous silicon and its alloys, Opto-Electronics Review 12(1), 21–32 (2004).

[27] A.Kolodziej, P.Krewniak, andS.Nowak, “Technologyofthe thin silicon solar cells”, Report for the State Committee for Sci- entific Research on realisation of the Goal Orientated Research, Project No. PBZ KBN 05/T11/98, AGH, Kraków, 2003.

[28] A. Kolodziej, P. Krewniak, and S. Nowak, “Improvements in silicon thin film solar cell efficiency”, Opto-Electron. Rev. 11, 71–79 (2003).

[29] R.A. Street and S. Guha, Technology and Applications of Amorphous Silicon, 1–100 and 252–305, Springer, Berlin, 2000.

[30] R.W. Collins, A.S. Ferlauto, G.M. Ferreira, K. Joohyun, C. Chi, R.J. Koval, J.M. Pearce, C.R. Wronski, M.M. Al-Jassim, and K.M. Jones, “Application of deposition phase diagrams for the optimisation of a-Si:H-based materials and solar cells”, Mat. Res. Soc. Symp. Proc. 762, A10.1.1–A10.1.12 (2003).

[31] G. van Elzakker, "Hydrogenated Amorphous Silicon Solar Cells Deposited From Silane Diluted with Hydrogen, Ph.D Thesis," Technische Universiteit Delft, Delft, 2010.

[32] A. Kolodziej, P. Krewniak, and S. Nowak, “Influence of ZnO/p+a-Si:H microcrystallisation and antireflection coatings on pin a-Si:H solar cells performance”, Mat. Res. Soc. Symp. Proc. 715, A6.7.1–A6.7.6 (2002).

[33] O. Vetterl, F. Finger, R. Carius, P. Hapke, L. Houben, O. Kluth, A. Lambertz, A. Muck, B. Rech, H. Wagner, Intrinsic microcrystalline silicon: a new material for photovoltaics, Solmat 62 (2000) 97.

[34] A.H. Mahan, J. Yang, S. Guha, D.L. Williamson, Structural changes in a-Si:H film crystallinity with high H dilution, Phys. Rev. B 61 (2000) 1677.

[35] R.S. Crandall, Defect relaxation in amorphous silicon: stretched exponentials, the Meyer–Neldel rule, and the Staebler-Wronski effect, Phys. Rev. B 43 (1991) 4057.

[36] M. Stutzmann, W.B. Jackson, C.C. Tsai, Light-induced metastable defects in hydrogenated amorphous silicon: a systematic study, Phys. Rev. B 32 (1985) 23.

[37] H. Fritzsche, Photo-induced structural changes associated with the Staebler-Wronski effect in hydrogenated amorphous silicon, Solid State Commun. 94 (1995) 953.

[38] A.H. Mahan, J. Yang, S. Guha, D.L. Williamson, Structural changes in a-Si:H film crystallinity with high H dilution, Phys. Rev. B 61 (2000) 1677.

[39] S.T. Pantelides, Defect dynamics and the Staebler-Wronski effect in hydrogenated amorphous silicon, Phys. Rev. B 36 (1987) 3479.

[40] T. Su, P.C. Taylor, G. Ganguly, D.E. Carlson, Direct role of hydrogen in the Staebler-Wronski effect in hydrogenated amorphous silicon, Phys. Rev. Lett. 89 (2002).

[41] D.X. Han, J. Baugh, G.Z. Yue, Q. Wang, Light-induced structural changes and their correlation to metastable defect creation in intrinsic hydrogenated amorphous silicon films, Phys. Rev. B 62 (2000) 7169.

[42] G. Cannella, F. Principato, M. Foti, C. Gerardi, S. Lombardo, Comparison between textured SnO_2:F and Mo contacts with the p-type layer in p–i–n hydrogenate amorphous silicon solar cells by forward bias impedance analysis, Sol. Energy 88 (2013) 175.

[43] G. Cannella, F. Principato, M. Foti, S. Di Marco, A. Grasso, S. Lombardo, Carrier transport mechanism in the SnO_2:F/p-type a-Si:H heterojunction, J. Appl. Phys. 110 (2011) 24502.

[44] M. Foti, G. Cannella, C. Gerardi, S. Di Marco, S. Ravesi, N. Sparta, S. Lo Verso, F. Principato, S. Coffa, S. Lombardo, Role of the back metal–semiconductor contact on the performances of a-Si:H solar cells, in: Proceedings of the 220th ECS Meeting on Photovoltaics for the 21st Century, vol. 41, 2011.

[45] S. Lombardo, C. Tringali, G. Cannella, A. Battaglia, M. Foti, N. Costa, F. Principato, C. Gerardi, Plasmonic effects of ultra-thin Mo films on hydrogenated amorphous Si photovoltaic cells, Appl. Phys. Lett. 101 (2012) 123902.

[46] N. Nakamura, K. Watanabe, M. Nishikuni, Y. Hishikawa, S. Tsuda, H. Nishiwaki, M. Ohnishi, Y. Kuwano, Influence of excess carriers on the Staebler and Wronski effect of a Si solar cells, J. Non-Cryst. Solids 59 (1983) 1139.

[47] H.C. Sun, Y.J. Yang, J.Y. Chen, T.M. Chao, C.W. Liu, W.Y. Lin, C.C. Bi, C.H. Yeh, Enhanced recovery of light-induced degradation on the micromorph solar cells by electric field, J. Appl. Phys. 112 (2012) 056104.

[48] B. O'Regan, M. Grätzel, A low-cost, high-efficiency solar cell based on dye-sensitized colloidal TiO2 films, Nature 353, 737 (1991).

[49] M. Grätzel, Solar Energy Conversion by dye-sensitized photovoltaic cells, Inorg. Chem. 44, 6841 (2005).

[50] Q. Yu, et al, High-efficiency dye-sensitized solar cells: the influence of lithium ions on exciton dissociation, charge recombination, and surface states, ACS nano 4(10), 6032 (2010).

[51] Y. Chiba, et al, Dye-sensitized solar cells with conversion efficiency of 11.1%, Jpn. J. Appl. Phys. 45.7L, L638 (2006).

[52] L.M. Gonçalves, et al, Dye-sensitized solar cells: a safe bet for the future, Energy Environ. Sci. 1, 655 (2008).

[53] S. Ito, et al, Fabrication of screen-printing pastes from TiO_2 powders for dye-sensitised solar cells, Prog. Photovolt: Res. Appl. 15, 603 (2007).

[54] S. Ito, et al, Fabrication of thin film DSSC with solar to electric power conversion efficiency over 10%, Thin Solid Films 516, 4613 (2008).

[55] M. K. Nazeeruddin, et al, Conversion of light to electricity by cis- X2bis(2,2'-bipyridyl-4,4'-dicarboxylate)ruthenium(II) charge-transfer sensitizers (X = Cl-, Br-, I-, CN-, and SCN-) on nanocrystalline titanium dioxide electrodes, J. Am. Chem. Soc. 115 (14), 6382 (1993).

[56] M. K. Nazeeruddin, et al, Engineering of efficient panchromatic sensitizers for nanocrystalline TiO_2-based solar cells, J. Am. Chem. Soc. 123 (8), 1613 (2001).

[57] D. Kuciauskas, et al, Electron transfer dynamics in nanocrystalline titanium dioxide solar cells sensitized with ruthenium or osmium polypyridyl complexes, J. Phys. Chem. B. 105, 392 (2001).

[58] R. Argazzi, G. Larramona, C. Contado, C.A. Bignozzi, Preparation and Photoelectrochemical Characterization of a Red Sensitive Osmium Complex Containing 4,4', 4''-Tricarboxy-2,2':6',2''-Terpyridine and Cyanide Ligands, J. Photochem. Photobiol. A. 164, 15 (2004).

[59] S. Altobello, et al, Sensitization of Nanocrystalline TiO_2 with Black Absorbers Based on Os and Ru Polypyridine Complexes, J. Am. Chem. Soc. 127, 15342 (2005).

[60] J. H. Yum, et al, Efficient far red sensitization of nanocrystalline TiO_2 films by an unsymmetrical squaraine dye, J. Am. Chem. Soc. 129, 10320 (2007).

[61] W.M. Campbell, et al, Highly efficient porphyrin sensitizers for dye-sensitized solar cells, J. Phys. Chem. C 111, 11760 (2007).

[62] G. Calogero, et al, Vegetable-Based Dye-Sensitized Solar Cells, Chem Soc Rev. 44, 3244 (2015).

[63] A.S. Polo, M.K. Itokazu, N.Y. Murakami Iha, Metal complex sensitizers in dye-sensitized solar cells, Coord. Chem. Rev. 248, 1343 (2004).

[64] Y. Tachibana, et al, Subpicosecond interfacial charge separation in dye-sensitized nanocrystalline TiO_2 films, J. Phys. Chem. 100, 20056 (1996).

[65] B. Wenger, M. Grätzel, J. E. Moser, Rationale for Kinetic Heterogeneity of Ultrafast Light-Induced Electron Transfer from Ru(II)-Complex Sensitizers to Nanocrystalline TiO_2, J. Am. Chem. Soc. 127, 12150 (2005).

[66] D. Kuang, et al, High molar extinction coefficient heteroleptic ruthenium complexes for thin film dye-sensitized solar cells, J. Am. Chem. Soc. 128 (12), 4146 (2006).

[67] M. K. Nazeeruddin, C. Klein, P. Liska, M. Grätzel, Synthesis of novel ruthenium sensitizers and their application in dye-sensitized solar cells, Coord. Chem. Rev. 249, 1460 (2005).

[68] G. Calogero, G. Di Marco, Red Sicilian orange and purple eggplant fruits as natural sensitizers for dye-sensitized solar cells, Sol. Energy Mater. Sol. Cells 92, 1341 (2008).

[69] M.S Kim, et al, Enhancement of photovoltaic performance in dye- sensitized solar cells fabricated with dendritic photosensitizer containing site- isolated chromophores, Dyes and Pigments 99, 986 (2013).

[70] C. H Wu, et al, Porphyrins for efficient dye-sensitized solar cells covering the near-IR region, J. Mater. Chem. A 2, 991 (2014).

[71] Y. Hua, et al, New simple panchromatic dyes based on thiadiazolo[3,4-c]pyridine unit for dye-sensitized solar cells, Dyes and Pigments 102, 196 (2014).

[72] R. Sastrawan, et al, A glass frit-sealed dye solar cell module with integrated series connections, Sol. Energy Mater. Sol. Cells 90, 1680 (2006).

[73] D. Pumiglia, et al, Photoelectrochemical Response of DSSCs Under Prolonged Reverse Bias and Conduction Band Lowering in Ru-Complex- Sensitized TiO_2, Chem. Electro. Chem. 1, 1388 (2014).

[74] X. Zhang, X. Huang, H. Jiang, Recovering degraded quasi-solid-state dye-sensitized solar cells by applying electrical pulses, Phys. Chem. Chem. Phys. 15 (18), 6864 (2013).

[75] A. Subramaniam, J. S. Bow, H. W. Wang, The effect of Li^+ intercalation on different sized TiO_2 nanoparticles and the performance of dye-sensitized solar cells, Thin Solid Films 520, 7011 (2012).

[76] C. Chiappara, et al, Investigation of recovery mechanisms in dye sensitized solar cells, Solar Energy, 127, 56-66 (2016).